# MODELING AND APPLICATION OF POLYMERIC MICROGELS

A Dissertation
Presented to
The Academic Faculty

by

Svetoslav Nikolov

In Partial Fulfillment
of the Requirements for the Degree
Doctor of Philosophy in the
George W. Woodruff School of Mechanical Engineering

Georgia Institute of Technology
May 2020

# MODELING AND APPLICATION OF POLYMERIC MICROGELS

Approved by:


Dr. Alexander Alexeev, Advisor
School of Mechanical Engineering
*Georgia Institute of Technology*

Dr. Karl Jacob
School of Materials Science and Engineering
*Georgia Institute of Technology*

Dr. Tequila A. L. Harris
School of Mechanical Engineering
*Georgia Institute of Technology*

Dr. Alberto Fernandez-Nieves
Department of Condensed Matter Physics
*University of Barcelona*

Dr. Vladimir Tsukruk
School of Materials Science and Engineering
*Georgia Institute of Technology*



Date Approved: [March 18th, 2020]

# TABLE OF CONTENTS

# ACKNOWLEDGEMENTS

I would like to dedicate this work to my family who have provided unconditional support over the years. I would also like to thank my friends for their encouragement which was always well-timed. In addition I would like to thank my advisor Alexander Alexeev for welcoming me into his lab and taking a chance on me as a graduate student. His mentorship and guidance helped stabilize my journey through graduate school. Dr. Alexeev has always pushed me to attend conferences and seminars which significantly improved my public speaking skills over the years. I enjoyed my time in Dr. Alexeev's lab because he maintained an open dialogue within the lab which fostered independent thinking and helped establish a sense of comradery among the group. I would also like to thank our collaborators Dr. Fernandez-Nieves, Dr. Tsukruk, Dr. Fery, and Dr. Balazs. It was a privilage to work alongside you. I am extremely grateful to Dr. Fernandez-Nieves for the countless discussions over the years. His insights strongly shaped the way I think about soft matter. Additionally I would like to thank Dr. Harris, Dr. Jacob, and the rest of the reading committee members for reviewing my dissertation and providing helpful insights and comments. Lastly, I would like to say thank you to the rest of the Woodruff School of Mechanical Engineering academic faculty and staff which support the graduate student body.

# LIST OF TABLES

# LIST OF FIGURES

The attractive, neutral, and repulsive nanoparticles have $a_{N-P}$ equal to 60, 65, and 75, respectively.

# LIST OF SYMBOLS AND ABBREVIATIONS

| | |
|---|---|
| $A$ | Polymer-solvent repulsion coefficient |
| $X$ | Flory-Huggins interaction parameter |
| $\chi_i$ | Empirical coefficients for Flory-Rehner fit |
| $\Phi$ | Polymer volume fraction |
| $D$ | Collective diffusion coefficient of microgel network |
| $\Pi_{mix}$ | Osmotic pressure due to polymer-solvent mixing |
| $\Pi_e$ | Elastic osmotic pressure |
| $\Pi_{total}$ | Total osmotic pressure |
| $N_c$ | Number of chains in polymer network |
| $k_b$ | Boltzmann constant |
| $T$ | Temperature |
| $V_0$ | Microgel volume in reference state |
| $N_A$ | Avogadro's number |
| $v_s$ | Molar volume of the solvent |
| $\phi_0$ | Polymer volume fraction in reference state |
| $K$ | Bulk modulus |
| $\boldsymbol{F} = \sum_{j \neq i} \left( \boldsymbol{F}_{ij}^{C} + \boldsymbol{F}_{ij}^{D} + \boldsymbol{F}_{ij}^{R} \right)$ | Total force applied on bead *i* in DPD model |
| $\boldsymbol{F}^{C}$ | Conservative DPD force |
| $\boldsymbol{F}^{D}$ | Dissipative DPD force |
| $\boldsymbol{F}^{R}$ | Random DPD force |
| $a_{ij}$ | Coefficient of repulsion between beads *i* and *j* |

| | |
|---|---|
| $w(r_{ij})$ | Weighing function in DPD, $w(r_{ij}) = 1 - r_{ij}/r_C$ |
| $r_C$ | Cutoff distance for DPD interactions |
| $r_{ij}$ | Distance between beads *i* and *j*, $r_{ij} = \left\|\boldsymbol{r}_i - \boldsymbol{r}_j\right\|$ |
| $\boldsymbol{v}_{ij}$ | Relative velocity between beads *i* and *j* |
| $\hat{\boldsymbol{r}}_{ij}$ | Normalized position vector between beads *i* and *j*, $(\boldsymbol{r}_i - \boldsymbol{r}_j)/r_{ij}$ |
| $\xi_{ij}$ | Standard normal variable with zero mean |
| $\gamma$ | Dissipative force coefficient for DPD model |
| $\sigma$ | Random force coefficient for DPD model, $\sigma = \sqrt{2\gamma k_B T}$ |
| $\Delta t$ | Timestep |
| $U_{bond}$ | Bond energy |
| $k_{bond}$ | Harmonic bond stiffness |
| $r_{eq}$ | Equilibrium separation length between polymer beads |
| $U_{bend}$ | Bending energy |
| $k_{bend}$ | Bending stiffness which controls persistence length |
| $\theta$ | Angle between two polymer bonds sharing a common bead |
| $\boldsymbol{F}_{ij}^{SRP}$ | Segmented repulsive potential (SRP) force |
| $r_{c_{SRP}}$ | Cutoff distance for SRP potential |
| $r_{min}$ | Minimum distance between two bonds |
| $H$ | Coefficient for SRP potential |
| $\rho$ | Density in DPD model |
| $a_{S-S}$ | Repulsion coefficient for solvent-solvent interactions |
| $a_{P-P}$ | Repulsion coefficient for polymer-polymer interactions |

| | |
|---|---|
| $a_{P-S}$ | Repulsion coefficient for polymer-solvent interactions, $a \equiv a_{P-S}$ |
| $N$ | Average number of beads per chain |
| $R_{end}$ | End-to-end distance of polymer chain |
| $b$ | Kuhn length |
| $v$ | Flory's exponent |
| $N_{min}$ | Minimum number of beads in the chain for flexible behavior |
| $P$ | Microgel porosity |
| $\rho_c$ | Crosslink density |
| $\eta$ | Total number of crosslinks in microgel network |
| $V_a$ | Microgel volume for a given solvency $a$ |
| $R$ | Microgel radius |
| $R_{final}$ | Final equilibrated gel radius |
| $R_{ini}$ | Initial equilibrated gel radius |
| $\tau_{char}$ | Characteristic time constant |
| $t$ | Time |
| $G$ | Shear modulus |
| $f$ | Friction coefficient |
| $P_i$ | $i$ % porosity microgel |
| $\tau_{skin}$ | Timescale for skin layer formation |
| $\tau_v$ | Viscous timescale |
| $m_s$ | Mass of solvent bead |
| $\upsilon_{solv}$ | Solvent dynamic viscosity |
| $l_1$ | Average microgel mesh size for $R$ = 95 and $P_{65}$ |

| | |
|---|---|
| $\alpha$ | Swelling ratio |
| $\alpha_{max}$ | Maximum swelling ratio |
| $AR$ | Toroidal aspect ratio |
| $\phi_{skin\ layer}$ | Polymer volume fraction in skin layer |
| $k_{bond,s}$ | Harmonic bond stiffness for bonds in shell |
| $k_{bond,c}$ | Harmonic bond stiffness for mesh-centerline bonds |
| $a_{M-S}$ | Repulsion coefficient between mesh-solvent beads |
| $r_{handle}$ | Radius of toroidal handle |
| $r_{tube}$ | Radius of toroidal tube |
| $\Gamma$ | $\Gamma$ is the slope of $r_{handle}$ vs $r_{tube}$ during quasistatic deswelling |
| $R_c$ | Critical radius at which $\tau_{skin} \approx \tau_{deswell}$ |
| $\tau_{deswell}$ | Timescale for deswelling |
| $\tau_{swell}$ | Timescale for swelling |
| $E$ | Young's modulus |
| $\Pi_{network}$ | Pressure in microgel network |
| $V$ | Microgel volume |
| $W$ | Number of polymer beads in microgel network |
| $\sigma_{ii}^{ave}$ | Average normal stress per bead in *x*, *y*, and *z* directions |
| $r_{c,p}$ | Physical size of cutoff radius $r_c$ |
| $r_H$ | Hertzian contact radius |
| $L$ | Applied load |
| $\lambda$ | Displacement of plate |
| $\kappa$ | Number of microgel particles in a given suspension |
| $V_{sus}$ | Volume of microgel suspension |

| | |
|---|---|
| $V_{eq}$ | Equilibrated microgel volume in dilute conditions |
| $V_a$ | Equilibrated microgel volume at specified polymer-solvent repulsion coefficient, $a$ |
| $\psi$ | Generalized packing fraction |
| $\varphi$ | Packing fraction |
| $V_{box}$ | Computational box volume |
| $N_{solvent}$ | Number of solvent beads inside microgel volume |
| $N_{total}$ | Total number of beads inside of microgel volume |
| $V_{eq25}$ | Equilibrium volume of single microgel particle at $a = 25$ |
| $\psi_c$ | Generalized packing fraction at the critical point |
| $S$ | Surface area to volume ratio |
| $\delta$ | Radial microgel-microgel penetration distance |
| $\delta_{X-link}$ | Average crosslink distance |
| $K_P$ | Bulk modulus of a standalone microgel particle at the specified $\psi$ and $a$ |
| $G'$ | Storage modulus |
| $G'$ | Loss modulus |
| $G'_{crossover}$ | Storage modulus at crossover point where $G' = G''$ |
| $\omega_{crossover}$ | Crossover frequency |
| $\tau_{relax}$ | Relaxation time of microgel suspension |
| $L/W$ | Length-to-width aspect ratio of microsheet |
| $P_{avg}$ | Average pressure in composite layer |
| $\varepsilon$ | Swelling ratio |
| $\zeta$ | Thermal expansion coefficient |
| $h_1$ | 1 / 2 thickness of polystyrene layer |

| | |
|---|---|
| $h_2$ | 1 / 2 thickness of silk ionomer layer |
| $h_3$ | 1 / 2 thickness of $\beta$-sheet layer |
| $h_{i,j}$ | Distance between the centroidal lines of the $i$ and $j$ layers |
| $r_{curv}$ | Radius of curvature of composite structure |
| $E_1$ | Modulus of elasticity of polystyrene layer |
| $E_2$ | Modulus of elasticity of silk ionomer layer |
| $E_3$ | Modulus of elasticity of $\beta$-sheet layer |
| $A_1$ | Area moments of inertia of polystyrene layer |
| $A_2$ | Area moments of inertia of silk ionomer layer |
| $A_3$ | Area moments of inertia of $\beta$-sheet layer |
| $k$ | Spring constant |
| $d_R$ | Thickness of responsive layer in microswimmer |
| $d_P$ | Thickness of passive layer in microswimmer |
| $w_{arm}$ | Width of microswimmer arm |
| $L_{side}$ | Length of microswimmer arm |
| $s$ | Arc length of microswimmer arm |
| $q$ | Curvature of microswimmer arm |
| $P_{act}$ | Period actuation for microswimmer |
| $V_{swim}$ | Swimming speed of microswimmer |
| $n_s$ | Number density of crosslink points in microswimmer polymer network |
| $T_R$ | Thickness ratio of bilayer microswimmer, $T_R = d_P/d_R$ |
| $V_s$ | Swollen volume |
| $V_c$ | Collapsed volume |

| | |
|---|---|
| $a_{P-Nano}$ | Repulsion coefficient for polymer-nanoparticle interactions |
| $a_{ii}$ | Self-repulsion for beads of the same species |
| $a_{EG-EG}$ | Self-repulsion for end-group beads on polymer brush |
| $a_{P-PB}$ | Repulsion coefficient for microgel-brush interactions |
| $C_{ext}$ | Concentration of nanoparticles in external solvent |
| $C$ | Concentration of nanoparticles in microgel network |
| $N_{adv}$ | Particles captured due to advection |
| $V_{bulb}$ | Volume of gel bulbs |
| $N_{diff}$ | Particles captured due to diffusion |
| $A_{bulb}$ | Bulb area exposed to solvent |
| $l_{diff}$ | Characteristic diffusion timescale |
| $D_P$ | Nanoparticle diffusion coefficient |
| $Pe$ | Peclet number |
| $P_{act}$ | Actuation period for active microcapsule |
| $T_{tot}$ | Total simulation time |
| DPD | Dissipative particle dynamics |
| PNIPAM | Poly(N-isopropylacrylamide) |
| LCST | Lower critical solution temperature |
| MG | Methacrylated gelatin |
| HA-Tyr | Hyaluronic acid-tyramine |
| HRP | Horseradish peroxidase |
| SARW | Self-avoiding random walk |
| LAMMPS | Large-scale Atomic/Molecular Massively Parallel Simulator |

| | |
|---|---|
| OVITO | Open Visualization Tool |
| PS | Polystyrene |
| SI | Silk-ionomer |
| BS | $\beta$-sheet |
| LSM | Lattice Spring Model |
| PVCL | Poly(N-vinylcaprolactam) |

# SUMMARY

This work develops a mesoscale hydrogel model that is based on dissipative particle dynamics (DPD). The model is used to study the mechanics and kinetics of different microgel systems. Firstly, we examine how the swelling curves and microgel kinetics vary for microgel particles with different network properties. In our simulations we find that during deswelling the network is highly inhomogeneous as the polymer chains bundle and cluster with nearby neighbors. Depending on the microgel network parameters this can either speed-up or arrest the deswelling. To determine how the microgel mechanics vary throughout the volume phase transition we evaluate the bulk and Young's moduli at different solvents. The mechanical results show good agreement with Flory-Rehner theory signifying that our model can capture both the microgel kinetics and mechanics. We leverage single microgel particle results to probe the behavior of microgel suspensions at different packing fractions and solvencies. Our findings demonstrate that mechanical responses are guided by the single particle modulus. We show that loss and storage moduli data can be scaled onto two master curves, when normalizing by the crossover frequency and loss modulus. Using our mesoscale model, we construct various hydrogel-based microdevices, including self-folding microsheets, a self-propelling bi-layered microswimmer, and an active microcapsule. The self-folding microsheets are shown to produce different 3D structures like helical coils and microtubules depending on the initial 2D geometry. The novel active-passive bilayer microswimmer generates time irreversible motion and achieves self-propulsion due to the timescale mismatch between de/swelling

and bending. The active microcapsule can selectively capture nanoparticles from the external solvent at predefined rates, controlled by the actuation period.

# CHAPTER 1. INTRODUCTION

## 1.1 Motivation

Hydrogels are highly porous 3D networks which when exposed to an external stimulus, like temperature, light intensity, pH changes, or magnetic/electric fields can experience drastic changes in their internal structure [2-5]. One of the most well-known examples is Poly(N-isopropylacrylamide) or PNIPAM. PNIPAM experiences a lower critical solution temperature (LCST) at ~32°C, which means that when this material is heated above the LCST, the initially highly porous and solvent-rich network experiences a volume phase transition. During this transition the gel collapses, expelling solvent from the network interior in the process. The swelling/deswelling process is reversible and easily controlled by varying the underlying external stimulus. In the 1980-90s a large body of work went into characterizing the behavior of macrogels (cm-mm sized gels) [6-12]. Over the past two decades researchers have extended much of the earlier work to the micro realm (50nm – 100μm) and found that many of the earlier findings apply equally well [13-15].

The large volume changes achieved by these microgels near the critical point of the volume phase transition in tandem with their tissue-like biocompatible nature has made them a promising material of choice for a variety of biomedical and engineering applications like micro-actuation [16-18], tissue scaffolding [19-24], drug delivery [25-28], and micro-catalysis [29, 30]. Recent experiments show that by varying the relaxation rates of the underlying hydrogel matrix, mesenchymal stem cells can be predisposed towards osteogenic differentiation (vs. adipogenic differentiation) which is important for bone tissue formation [31]. Additionally, methacrylated gelatin (MG) scaffolds have been

used to regrow cardiac muscle cells [32]; it was shown that by enriching the MG network with carbon nanotubes, the beating frequency of the cells could be varied. Hydrogels have also been used extensively to create novel drug delivery devices. A new hydrogel-based microdevice capable of aiding diabetics by delivering a sustained release of insulin in response to enzymatic oxidation of glucose has been recently demonstrated [33]. Additionally, microscopic hydrogel particles have been used to encapsulate living cells to create 3D microenvironments for cell culturing [34] for controlled release of DNA targets [35]. Ultrasoft microgels have also been shown to act as artificial platelets facilitating blood clotting [36], whereas dense colloidal suspensions of such microgels enable assays to evaluate cell invasiveness [37]. Furthermore, stimuli-responsive multi-layered gel structures are promising for microactuator applications [16-18] and for designing self-propelling robots [38-40].

In the recent work of Ren *et al.* researchers developed a thermally triggered hyaluronic acid-tyramine (HA-Tyr) injectable hydrogel scaffold [19]. By placing liposome encapsulated horseradish peroxidase (HRP) (derived via the dehydration-rehydration vesicle method) and hyaluronic acid-tyramine conjugates in a hydrogen peroxide solution, researchers were able to induce gelation between the HRP and HA-Tyr conjugates by varying the temperature. Near room temperature the HRP and hyaluronic acid-tyramine solution remained liquid, but when injected into a target site *in vivo* in mice the rise in temperature caused a phase change in the liposomes, which increased the membrane permeability, allowing for the HRP (crosslinking agent) to make contact with the external solution and for oxidative coupling of Tyr moieties to occur, which lead to the formation of a hydrogel network. The implications of this work are significant as they can lead to

groundbreaking developments in areas of tissue engineering, in particular the injectable HA-Tyr hydrogel networks have promising applications as synthetic scaffolds for cartilage repair [41-44]. Further developments and enhancements of hydrogel-based therapies, like the one introduced by Ren *et al.*, are critically dependent on fully understanding the underlying micromechanics and kinetics of hydrogels. Understanding the micro-macro property relations in the case of Ren *et al.* can allow researchers to design permanent scaffolds with self-healing properties that allow for longer *in vivo* lifetimes and higher immunogenicity.

Up to this point, phenomenological (Flory-Rehner type) models have been widely used to characterize stimuli-sensitive hydrogels [7, 11-13, 45-47]. While these models correctly capture how the bulk properties change near the critical point, they do not provide a clear picture as to how individual chain parameters affect network mechanics. In that regard, molecular dynamics models, which study the hydration/swelling of individual polymer chains have been developed [48]. Although invaluable insight has been gained from these efforts, especially regarding hydration, creating larger mesoscopic networks using these atomistic models is currently not possible. Application in the relevant nm-μm length scales are typically not computationally accessible using atomistic simulations [49], hindering the potential utility in solving engineering problems. Continuous approaches enable access to much larger length and time scales compared to atomistic models. In this case, however, connecting individual chain parameters to bulk material properties is not an easy task for hydrogel materials [50] due to the complex interplay among elastic, hydrodynamic, and chemical interactions. As a result, mesoscale models of polymeric materials are gaining popularity due to their ability to tackle problems that are inaccessible

by other methods [51-53]. In our study, we focus on developing a mesoscale model which can simulate the mechanics of hydrogels on longer spatial and temporal scales (while retaining the main ideas from the aforementioned theoretical and molecular models).

## 1.2 Research Objectives

In this work we aim to develop a mesoscopic model which will allow us to study how individual polymer chain parameters affect the mechanics and kinetics of microgel particles. To achieve this, we rely on concepts from polymer physics to characterize the behavior of single polymer chains. Then, using these chains as building blocks, we construct large spherical random polymer networks. After the networks are constructed we apply the appropriate stresses to measure the underlying mechanical response of each network and we compare this response to Flory-Rehner's theory [13].

In addition to this we track the kinetics during instantaneous swelling/deswelling of each network and compare the volume change of the networks to the corresponding volume changes predicted by Tanaka's theory for swelling [9]. For instantaneous deswelling experimentally it has been shown that in some cases microgel kinetics can become arrest as a dehydrated "skin layer" near the gel-solvent interface forms [1, 54]. Our goal is to investigate the impact of such skin layer formation on the microgel kinetics. Additionally, we want to understand how skin layer growth varies for different microgel sizes and network structures. Lastly, we aim to examine how the collective diffusion coefficient varies throughout the volume phase transition for quasistatic swelling/deswelling.

Another objective of the current research is to utilize the single particle model to construct large colloidal suspensions and study how the mechanical behavior of these suspensions' changes with packing fraction and solvency. The colloidal suspensions themselves are made up of many (~100) soft and deformable spherical particles which give the suspensions an incredibly rich mechanical response. The soft, deformable, and responsive nature of the constituent particles allows these suspensions to reversibly alternate between fluid-like and glassy behavior. Examining the mechanical behavior of compressed microgel suspensions, which have a high energy storage capacity and fast response times, will help researchers design novel self-healing materials. The results of this work should lead to many interesting conclusions since the colloidal suspensions themselves resemble biological tissue which is made up of soft and deformable cells.

The final goal of the research is to design novel hydrogel-based microdevices. To that extent, we first create a model which will allow us to predict swelling induced deformations in active trilayered composite microsheets. The active material in this system is a silk-ionomer hydrogel which can swell/deswell with changes in the pH. Swelling of the silk-ionomer layer generates stresses in the adjacent passive layers and initiates the deformation of the composite structure. We show that by varying the thickness and aspect ratios of the microsheets we can control the final 3D equilibrated structures. After this, we also show how bilayered hydrogel microsheets can be leveraged to create a microscopic swimmer that is capable of swimming in a viscous fluid when actuated by a periodically applied stimulus. For this microdevice we will demonstrate that the swimming speed depends on the relative stiffness of the two gel layers composing the swimmer, and we will determine the optimal stiffness ratio for swimming. In addition to this microswimmer, we

will also design a phagocyte-like, active microcapsule which can selectively capture external particles. Here we will study how the capture rate depends on the swelling period and we will quantify the ideal swelling period which maximizes capture rates.

### 1.3 Survey of Prior Studies

Some of the earlier experimental work on macrogel properties was done by Hirotsu and Tanaka which focused on gel mechanics and swelling kinetics, respectively. Hirotsu was the one to point out the dip in the bulk modulus and the corresponding negative Poisson ratios [7, 10-12]. Meanwhile Tanaka developed a very popular theory for the swelling kinetics of spherical macrogel particles, which allows the relaxation time and collective diffusion coefficient of the network to be calculated [9]. Tanaka's work is pivotal because it clarifies the misconception that the swelling/deswelling kinetics of a macrogels are set by the diffusion of the water molecules. Instead, Tanaka shows that the swelling kinetics are set by the diffusion of the polymer network into the water, which can be characterized by the collective diffusion coefficient $D$ [9]. In their work Tanaka *et al.* also showed that a critical point can be observed in the macrogel kinetics [8]. This was done by incrementally collapsing a gel network and at each point quantifying the collective diffusion of the network. Near the critical point a dip in $D$ was observed, where $D$ decreases by about an order of magnitude as it approached zero. This indicates that at the critical point network relaxation becomes arrested. During rapid deswelling it was also observed that macrogel kinetics can become arrested [1, 55, 56] leading to deswelling times which are on the order of days/weeks [55, 57].

Over the years there has been a large (and still growing) body of experimental work which was(is) compared against Flory Rehner's theory. The utility of the theory comes from the fact that it beautifully captures all the non-linear behavior which is seen experimentally. To derive the expression for the bulk modulus from the theory we start with the equilibrium condition for total osmotic pressure $\Pi_{total} = \Pi_e + \Pi_{mix} = 0$, where $\Pi_e = \frac{N_c k_b T}{V_o}\left[\left(\frac{\phi}{2\phi_o}\right) - \left(\frac{\phi}{\phi_o}\right)^{1/3}\right]$ is the elastic osmotic pressure and $\Pi_{mix} = \frac{N_A k_b T}{v_s}[\phi + ln(1-\phi) + \chi\phi^2]$ is the osmotic pressure due to polymer-solvent mixing. Here $\phi$ is the polymer volume fraction, $N_c/V_o$ is the number of polymer chains in the preparation state per volume, $v_s$ is the molar volume of the solvent, $\phi_o$ is the volume fraction in the preparation state, $\chi$ is the solvency parameter, $N_A$ is Avogadro's number, $k_b$ is Boltzmann's constant, and $T$ is the temperature. Using that $K = \phi\frac{\partial \Pi_{total}}{\partial \phi}$ and Flory's description of $\Pi_{mix}$ and $\Pi_e$, we can obtain an expression for the microgel bulk modulus: $K = \frac{k_b T}{v_s}\left(\frac{N_c}{V_0} v_s\left[\frac{1}{2}\left(\frac{\phi}{\phi_0}\right) - \left(\frac{\phi}{2\phi_0}\right)^{1/3}\right] + \frac{\phi^2}{1-\phi} - 2\chi\phi^2\right)$. This equation can be used to fit the experimental data via nonlinear regression. Thus Flory-Rehner's theory can predict how $K$ will vary with polymer volume fraction and solvency.

In the 1990s Hirotsu *et al.* showed that Flory-Rehner's theory can capture the behavior of experimental macrogels well. An important finding in their work is that the volume phase transition becomes sharper as the gel softens and becomes more fragile [10]. More recently Fernandez-Nieves *et al.* have shown that Flory-Rehner's theory applies equally well to microgel PNIPAM particles [13]. Their experimental findings are in good agreement with the prior macrogels studies carried out by Hirotsu and Tanaka [10]. In their work Fernandez-Nieves *et al.* determined that a quadratic expansion of the $\chi$ parameter is

needed ($\chi = \chi_0 + \chi_1\varphi + \chi_2\varphi^2$) in order for the fit to be accurate, which shows that many-body interactions near the critical point become significant [13].

Fernandez-Nieves *et al.* also studied the behavior of compressed microgel suspensions where they illustrated how the phase change process for compressed suspensions changes with particle stiffness [58]. They showed that for very soft particles only a liquid phase exists. As the particle stiffness increases liquid crystal and glassy phases begin to emerge [58]. For stiff enough particles the behavior resembles that of hard spheres [58]. In addition to this work Fernadez-Nieves *et al.* also showed that the shear and bulk moduli of compressed microgel suspensions are set by the single particle bulk modulus [59]. For these suspensions they noted a three order of magnitude difference in the bulk and shear moduli. This is totally different than what is seen for other disordered soft matter systems like compressed emulsions and foams, where the mechanical response is set by the interfacial energy, which only leads to an order of magnitude difference in the bulk and shear moduli. The much higher bulk modulus in the microgel suspensions allows this material to exhibit high energy storage and fast response times. The low shear modulus, meanwhile, means that particles can easily rearrange, making this material ideal for self-healing applications. Overall, the work of Fernandez-Nieves *et al.* shows that compressed microgel suspensions exhibit a uniquely rich mechanical behavior which cannot be elicited from other soft matter systems [58-61].

Using Flory-Rehner's theory to understand how properties on the microscale (monomer type, chain flexibility, etc.) affect the bulk mechanical behavior is not possible. In that regard, recently Kojima *et al.* put forth a cooperative dehydration theory which more closely describes the physics of neutral microgels. The theory stipulates that for nonionic

PNIPAM gels the onset of the volume phase transition is dictated by a cooperative dissociation of the bound water molecules from the polymer chain [62]. A ball and stick model of PNIPAM is shown in Figure 1.1a. Kojima *et al.* hypothesize that when a water molecule engages in hydrogen bonding with the amide group (NH-C=O) the nearby bulky isopropyl groups ($CH_3$) get displaced which makes it sterically easier for more localized hydrogen bonding to occur. Kojima *et al.* illustrate how this behavior can be incorporated into the Flory-Rehner picture by modifying the original solvency parameter $\chi$. A significant finding in their work is the fact that random hydration (without cooperativity) cannot reproduce a discontinuity in the swelling curve and the corresponding mechanical response observed for some microgels [12].

One of the models which takes the hydrogen bonding aspect into account is the model proposed by Deshmukh *et al.* which is a molecular dynamic (MD) model for PNIPAM cross-linked with BIS [48]. In their work the authors used the GROMOS96 force-field with corresponding bond, angle, and dihedral potentials. The initial structures were generated using a self-avoiding random walk (SARW) model. Although very accurate, the major drawback of this model is that the corresponding length and time scales which can be modeled are relatively small (angstroms and nanoseconds). To access larger length and time scales mesoscopic modeling techniques need to be applied. In general, mesoscale models reduce computational costs by eliminating extra degrees of freedom which are considered nonessential with respect to the phenomenon of interest.

In the recent work of Zaccarelli *et al.* researchers developed a patchy particle mesoscale model which is intended to computationally reproduce the experimental polymer network structure [63]. Once the computational structure is achieved traditional bead-spring

modeling is used to model the microgel dynamics. In their work the level of coarse graining is larger than MD methods, each NIPAM monomer (Figure 1.1a) is represented by a single particle, a similar approach is taken for the BIS crosslinker. As a result, a single gel particle in their model has a characteristic size of approximately 50 nm. A limitation in their work is the fact that there is no explicit solvent in the model. The microgel collapse is achieved via a pseudopotential which they introduce. The pseudopotential introduces attractive forces between monomers as the solvency is decreased, which causes the microgel to collapse in bad solvent. The lack of explicit solvent is beneficial because it reduces the overall compute time. However, removing solvent particles from the simulation can also lead to unphysical gel kinetics.

Numerous other mesoscale models have been developed over the years which study polyelectrolyte gels [64-66], multi-shell microgels [67], Belousov–Zhabotinsky reactions in gels [68] and self-regulating behavior (via feedback-loops) [69]. No mesoscale models have been developed however which properly capture the kinetics and mechanics of microgels along with the hydrodynamics of the embedded solvent.

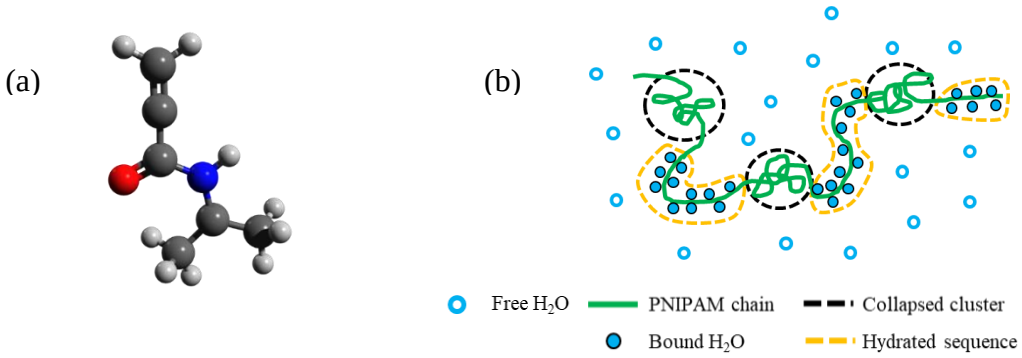


Figure 1.1 (a) Ball and stick model of PNIPAM monomer. Dark gray particles represent carbon atoms while the light gray particles represent hydrogen. The red and blue particles represent oxygen and nitrogen atoms, respectively. (b) Illustration of cooperative hydration scheme proposed by Kojima et al. Water molecules bind to PNIPAM chain in consecutive sequences to form a pearl-necklace conformation.

# CHAPTER 2. MESOSCALE MODEL OF MICROGELS

## 2.1 Introduction

Experimentally, microgel particles are often characterized by their swelling curve, which illustrates how the microgel volume or porosity vary throughout the volume phase transition. An important step towards obtaining a better understanding of the microgel micromechanics and kinetics is determining how individual chain parameters affect the microgel network. We initially focus on characterizing the flexibility of individual polymer chains, where we aim to minimize computational costs while still retaining the flexibility profile observed in experiments. To achieve this, we rely on Flory's theory which utilizes a mean-field approach to predict the equilibrium conformation of real 3D polymer chains. We then create spherical microgel networks with different average chain lengths. By swelling/deswelling these networks we can then gauge the impact that the average chain length has on the volume phase transition of a microgel particle.

We focus on studying "neutral" microgel networks using the dissipative particle dynamics (DPD) method. The "neutral" distinction signifies that swelling/deswelling does not occur as a result of ionic interactions, as is the case for polyelectrolyte gels. Experimentally, microgels like PNIPAM are often regarded as "neutral", where the swelling/deswelling transition is driven by hydrogen bonding. In the section which follows we outline the computational setup for our DPD model. The remaining chapters build on the ideas introduced in Chapter 2.

## 2.2 Dissipative Particle Dynamics

We use DPD, a particle-based method where beads represent mesoscales molecular clusters and fluid volumes [70-72], to model a mesoscale polymeric network immersed in a viscous solvent. The beads follow Newtonian dynamics and interact via soft potentials allowing a larger time step for the integration of the equation of motion. This in turn enables modeling systems over extended time scales, which is unachievable using atomistic methods. Furthermore, DPD uses pairwise interactions that preserve local hydrodynamics that is critical for modeling systems involving fluid flows. DPD has long been successfully tested against scaling theories for modeling simple systems [49, 73-79] and experimental data [80-88] showing it can capture relevant physical effects.

The governing dynamics between beads in DPD is set by three main forces $\boldsymbol{F} = \sum_{j \neq i}\left(\boldsymbol{F}_{ij}^{C} + \boldsymbol{F}_{ij}^{D} + \boldsymbol{F}_{ij}^{R}\right)$ acting between a given bead $i$ and its neighboring beads $j$ located within a cutoff radius $r_C$. There is a conservative repulsive force $\boldsymbol{F}_{ij}^{C} = a_{ij} w\left(r_{ij}\right)\hat{\boldsymbol{r}}_{ij}$, which leads to the bead excluded volume, a dissipative force $\boldsymbol{F}_{ij}^{D} = -\gamma w\left(r_{ij}\right)^2\left(r_{ij} \cdot v_{ij}\right)\hat{\boldsymbol{r}}_{ij}$ representing the effects of viscosity, and a random force $\boldsymbol{F}_{ij}^{R} = \sigma w\left(r_{ij}\right)\xi_{ij}(\Delta t)^{-1/2}\hat{\boldsymbol{r}}_{ij}$ associated with thermal fluctuations. The latter two forces are related by $\sigma^2 = 2\gamma k_B T$ due to the fluctuation- dissipation theorem. In all forces, $w\left(r_{ij}\right) = 1 - \hat{r}_{ij}$ is a weighing function with $\hat{r}_{ij} = r_{ij}/r_C$ and $r_{ij} = \left|\boldsymbol{r}_i - \boldsymbol{r}_j\right|$ the separation distance between beads $i$ and $j$. Additionally, $\hat{\boldsymbol{r}}_{ij} = \left(\boldsymbol{r}_i - \boldsymbol{r}_j\right)/r_{ij}$, $\xi_{ij}$ is a standard normal variable with zero mean, $k_B$ is the Boltzmann constant, and $T$ is the temperature.

To model the polymeric chains in the microgel we use a bead-spring model (Figure 2.1a), where DPD beads are connected using a harmonic bond potential, a bending angle potential, and a segmented-repulsive potential (SRP). The energy for the bond potential is given by $U_{bond} = k_{bond}(r - r_{eq})^2$, where $k_{bond}$ is the bond stiffness and $r_{eq}$ is the equilibrium separation length between beads. The energy for the angle potential is given by $U_{bend} = k_{bend}(1 + cos\,\theta)$, where $k_{bend}$ is the bending stiffness and $\theta$ is the angle between two polymer bonds sharing a common bead. The segmented repulsive potential prevents polymer chains from crossing each other; it is implemented by imposing a soft repulsive force between chain bonds. The associated force is given by $\boldsymbol{F}_{ij}^{SRP} = H(1 - r_{min}/r_{c_{SRP}})\hat{\boldsymbol{r}}_{ij}$, where $r_{c_{SRP}}$ is the cutoff distance for the SRP potential, $r_{min}$ is the minimum distance between two bonds, and $H$ is the strength of the potential [89].

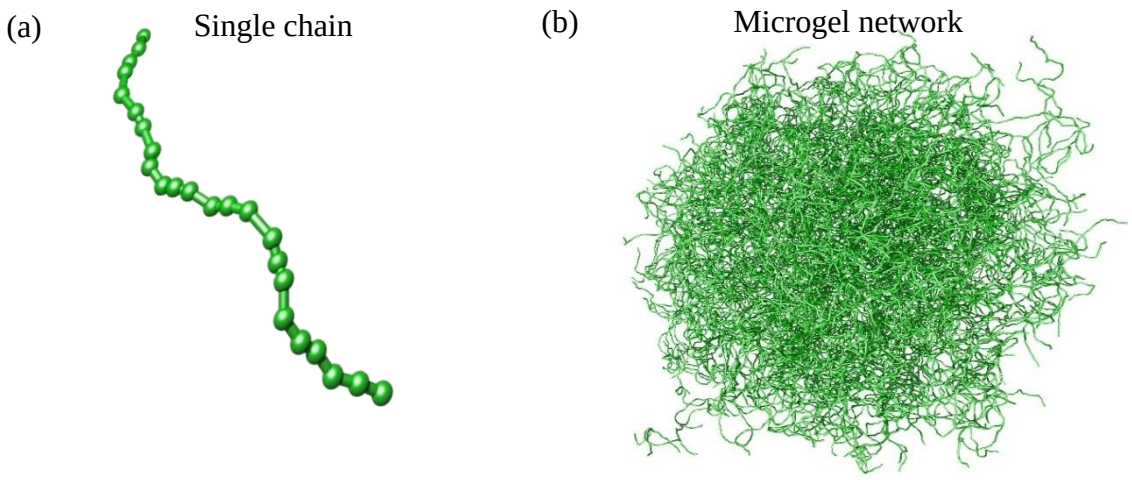


**Figure 2.1**. (a) Single polymer chain comprised of polymer beads connected with harmonic bonds. (b) Model microgel network composed of individual chains interconnected at crosslinking sites.

In our simulations, we set $r_C = 1, \gamma = 4.5, k_BT = 1, \rho = 3, r_{c_{SRP}} = 0.5, C = 100,$ and $\Delta t = 0.01$. Here, $\rho$ is the number density of DPD beads in the system and $\Delta t = 0.01$ is the simulation timestep. The repulsion between solvent beads and between beads within polymer chains are $a_{S-S} = 25$ and $a_{P-P} = 25$, respectively. To model swelling and deswelling of the polymer gel, we alter the polymer-solvent repulsion $a_{P-S}$ in the range between 20 and 35. For the sake of simplicity in what follows, we use $a$ without a subscript to indicate the polymer-solvent repulsion; hence $a \equiv a_{P-S}$. The bond stiffness for polymer chains is set to $k_{bond} = 35$ with $r_{eq} = 0.6$. The bending stiffness is set to $k_{bend} = 10$, except for single chain simulations where it is varied in the range between 0 and 10. Note that all dimensional parameters are expressed in DPD units, unless indicated otherwise.

To create the gel networks in this chapter, we randomly distribute 3600 crosslink points in a cubic box [87]. We then find all crosslink points separated by a distance in the range between $0.8r_{eq}N$ and $1.1r_{eq}N$, and randomly connect them with connectivity up to 4 using straight polymer chains. Here, $N$ is the average number of monomers per chain. The number of monomers in each chain is set such that the distance between beads is close to $r_{eq}$. A microgel with spherical shape is formed from the initial cubic gel by cutting out the chains outside the gel radius, with disconnected chain segments removed via a depth-first search algorithm [90] (Figure 2.1b). The final average connectivity is found to be about 3.4, mainly due to free chains at the outer gel surface.

For all the microgel networks in this chapter we use an identical initial crosslinking configuration. We investigate the effect of the number of beads per chain by setting $N =$ 6, 9, 12, and 24. To create networks with different $N$ we rescale the relative positions of crosslink points such that the average number of monomers in chain connecting them is

close to the desired value. Thus, all networks share the same characteristics including number of crosslinks, connectivity, and entanglements, and only differ by the number of monomers per chain; this corresponds to changing the crosslink-to-monomer ratio, which is often done in experiments [60, 91]. We conduct our simulations in a periodic computational domain. In the simulations with microgel networks, we choose a domain size in the range from $100 \times 100 \times 100$ to $170 \times 170 \times 170$ such that any interactions of the microgel with its periodical image are prevented. The domain size for single chain simulations is $20 \times 20 \times 20$. We keep the number density of the system constant by adding the required amount of solvent DPD beads. At the beginning of the simulations, we equilibrate the microgel network in solvent until a steady state situation is reached.

### 2.3 Single Chain Properties

Neutral PNIPAM gels are composed of polymer chains that exhibit flexible behavior [61]. We use this property as a guiding criterion for constructing our mesoscale model for a polymer chain. Flory's theory allows us to characterize the flexibility of

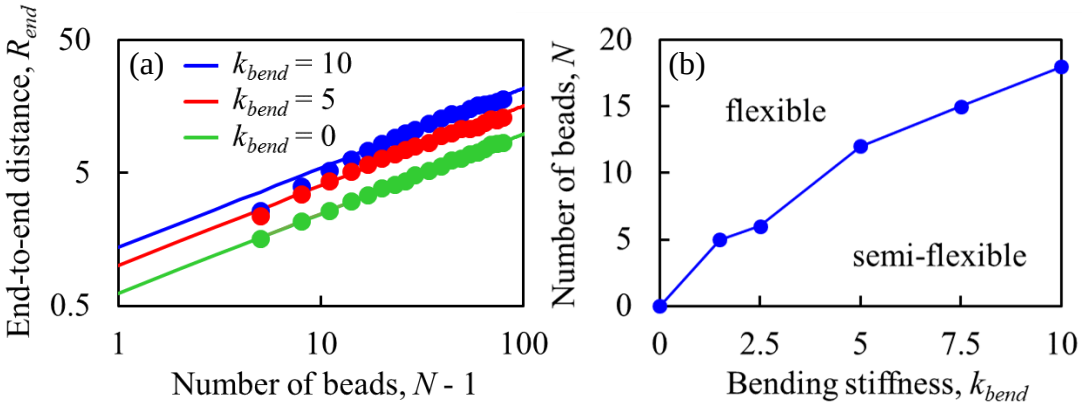


**Figure 2.2**. (a) End-to-end distance of linear chains with different bending stiffness. The points show simulation data, whereas the solid lines represent the Flory theory scaling behavior for flexible chains. As the bending stiffness increases, longer chains deviate from flexible behavior. (b) Minimum chain length for which chains follow flexible behavior as a function of chain bending stiffness. The line separates parameter space for the flexible and semi-flexible polymer chains. For stiffer chains, a longer length is required to recover flexible behavior.

individual polymer chains in dilute solution in terms of the relation between the end-to-end distance $R_{end}$ and the number of monomers $N$. This relation is given by $R_{end} \sim b(N-1)^{v}$, where $b$ is the Kuhn length, and $v$ is Flory's exponent, which is equal to $3/5$ for flexible, self-avoiding chains in a good solvent [92].

When the bead-spring model is used without bending stiffness, we reproduce the flexible behavior of a polymer chain with just a few beads per chain. In Fig, 2a, we show a log-log plot of $R_{end}$ as a function of the number of beads for chains with different bending stiffness $k_{bend}$. The solid lines in the figure correspond to $v = 3/5$. For $k_{bend} = 0$, the bead-spring model conforms to the expected scaling behavior, even for very short chains. Including bending stiffness, however, leads to deviations for chains with small number of beads, as shown for $k_{bend} = 5$ and $k_{bend} = 10$ in Figure 2.2a. These chains behave as flexible chains only if the number of beads in the chain is sufficiently large. In Figure 2.2b, we show the dependence of the minimum number of beads in the chain $N_{min}$ for the chain to be flexible as a function of the bending stiffness. This number increases as $k_{bend}$ increases. Hence, the chains with $N > N_{min}$ behave as flexible chains, whereas chains with $N < N_{min}$ are semi-flexible. Note that in our mesoscale microgel model, we are interested in using shorter chains to reduce the size of the system and accelerate the simulations.

In addition to changing the values of $N_{min}$, bending stiffness also affects the magnitude of the Kuhn length, which represents the effective length of orientationally independent segments within a polymer chain. For $k_{bend} = 0$, the Kuhn length is relatively short and is equal to about 0.6, which is the equilibrium length $r_{eq}$ for stretching springs connecting the beads in the chain. The addition of bending stiffness leads to an increased Kuhn length that increases nearly linearly with $k_{bend}$ within the tested range (Figure 2.3a). As we show below, larger values of Kuhn length are critical for modeling highly porous swollen gels.

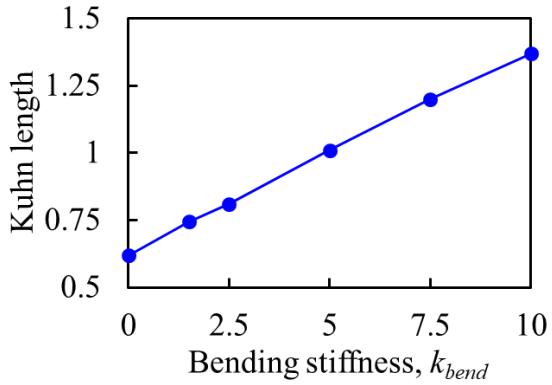


**Figure 2.3**. (a) Kuhn length monotonically increases with bending stiffness. With increasing $k_{bend}$, the number of beads in each Kuhn segment increases. For $k_{bend} = 0$, the Kuhn length corresponds to one bond length, which is ~0.6 in DPD units.

## 2.4 Swelling Curves

Hydrogels are characterized by a high porosity in a good solvent (> 90-95%) [61, 93]; this plays a fundamental role in gel transport properties, mechanics, and swelling kinetics. It is, therefore, important that our mesoscale microgel model can exhibit relevant values of porosity in good solvent conditions.

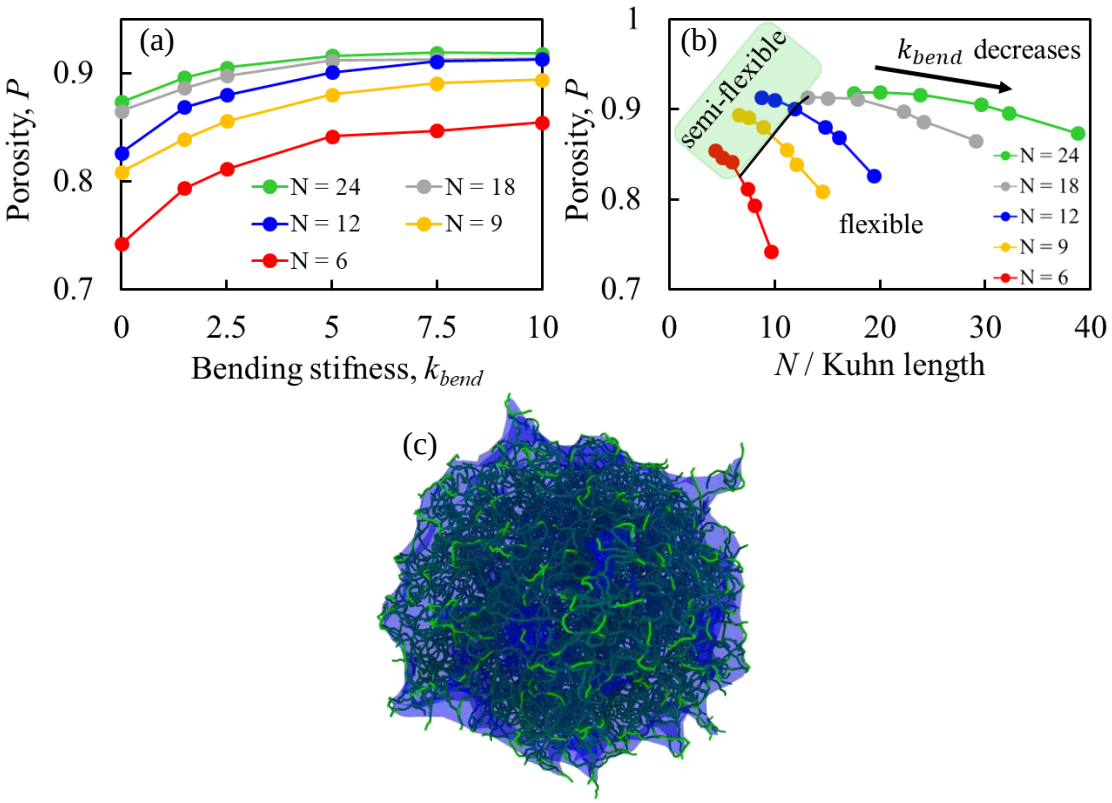


**Figure 2.4**. (a) Porosity of spherical microgels composed of chains with different length as a function of chain bending stiffness. (b) Plot showing how network porosity varies with the scaled chain length. While $N$ is fixed the variation in $k_{bend}$ causes the persistence to change, which alters the flexibility of the chain. The flexible and semi-flexible regimes from Figure 2.2 are shown here to illustrate the impact on porosity. (c) Triangulated surface mesh enclosing a microgel network. Mesh surface is shown in blue and gel network is shown in green. The surface mesh is semi-transparent.

In Figure 2.4a, we plot the gel porosity $P$ as a function of $k_{bend}$ for chains with different $N$. To determine the microgel porosity, we first measure the microgel volume $V$ by constructing a surface mesh enclosing the microgel network (Figure 2.4c) [94]. The surface mesh is defined using a probe with a radius of about half of the microgel crosslink distance. We then calculate microgel porosity based on the number of solvent beads located within the surface mesh. We find that $P$ increases with chain length. However, for $k_{bend} = 0$, the porosity does not exceed 0.87 even for relatively long chains with $N = 24$. Further

increase of the chain length can lead to higher porosity, but this also significantly extends computation time, as the domain size scales as $N^3$.

Long computational times can be avoided by noting that $P$ can be increased by using shorter chains with a greater $k_{bend}$ and, thus, a greater Kuhn length. Indeed, we find that for $k_{bend} = 10$, the porosity is about 0.95 for chains with $N = 24$, which is close to typical experimental values for hydrogels. Furthermore, these chains behave as flexible chains, which is also typical in experiments. We, therefore, use chains with $k_{bend} = 10$ in our mesoscale model. Figure 2.4b shows the impact of Kuhn length on network porosity and chain flexibility. The semi-flexible regime is highlighted in Figure 2.4b. Using chains with $k_{bend} > 10$ would further increase microgel porosity. However, this would require using longer chains in order to ensure that fully flexible behavior is maintained, which in turn would lead to excessive computational times.

We conduct simulations in which we place a spherical microgel network in solutions with different solvency, which we vary by changing the network solvent

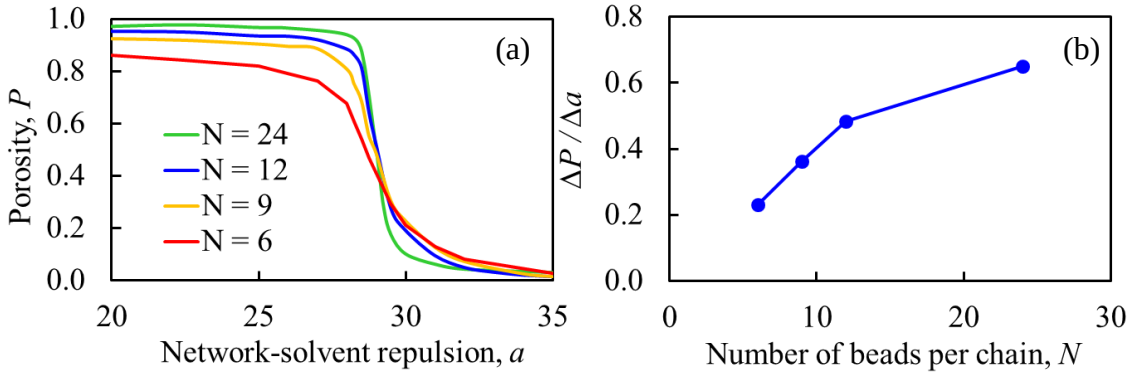


**Figure 2.5**. (a) Swelling curves in terms of porosity and the network-solvent repulsion for spherical microgels with different chain lengths. (b) Derivative of network porosity with respect to network-solvent repulsion near the swelling transition, $a \approx 29$. The magnitude of derivative increases with chain length indicating a sharper volume phase transition.

repulsion coefficient $a$. Larger values of $a$ correspond to bad solvents, whereas lower values of $a$ correspond to good solvents. At each $a$ we calculate the network porosity, which is shown in Figure 2.5a for gels with different $N$. In bad solvents, all microgel networks have a nearly zero porosity, indicating that the microgel expels practically all of the solvent and adopts a nearly collapsed state. As $N$ increases from 6 to 24 the microgel porosity in good solvent increases from $P \approx 86\%$ to $P \approx 95\%$.

The microgel volume change, as the solvent changes from good to bad, strongly depends on $N$. For $N = 6$, the volume increases approximately 7 times, when the microgel changes from the collapsed to the swollen state. For $N = 24$, the volume increases about 30 times between collapsed and swollen states. We find that as the chain length increases, the volume phase transition becomes sharper, as indicated by the greater value of the porosity gradient, $\Delta P/\Delta a$, for microgels with longer chains in Figure 2.5b. This behavior is related to the microgel softening due to the decreasing crosslink density $\rho_c = \eta/V_a$ in microgels with larger $N$. Here, $\eta$ is the total number of crosslinks and $V_a$ is the gel volume for a given value of $a$. This result is in qualitative agreement with expectations from the Flory-Rehner theory of polymer gels [10].

Larger volume changes can be also obtained by using polymer chains with greater bending stiffness. In good solvent, stiffer chains lead to a higher microgel porosity, whereas in bad solvent conditions, the size of collapsed gel is nearly insensitive to $k_{bend}$ and mostly defined by the excluded volume of the chains.

## 2.5 Summary

We have illustrated how a bead-spring model can be leveraged within the dissipative particle dynamics framework to simulate neutral microgel particles. The model network is immersed in an explicit viscous solvent. We alter the solvency by changing the repulsion between the network and the solvent. To prevent chains from crossing each other we employ bond-bond repulsive potentials. To model sufficiently large microgel networks, we identified single chain parameters leading to experimentally realistic microgel properties. We find that to model swollen microgels with high porosity, bending stiffness needs to be incorporated into the polymer chains to increase their Kuhn length. This imposes a limitation on the minimum polymer chain length when flexible chain mechanics is required.

We show that microgels undergo a continuous volume transition when the solvency is changed. In bad solvents, the network collapses to a nearly collapsed state, whereas in good solvents, the microgel swells with a porosity that increases proportionally to the chain length. Microgels with higher porosity are characterized by a sharper volume transition. This is in agreement with the work of Hirotsu, who hypothesizes that the gel softening at higher porosities increases the sharpness of the volume transition [10].

In its current implementation, our mesoscale model is limited to modeling microgels that exhibit a continuous volume phase transition. Thus, our microgel model cannot simulate gels with a negative Poisson ratio and discontinuity in the bulk modulus, which are observed near the critical volume phase transition for certain microgels [12]. More elaborate chain-chain and chain-solvent interactions need to be integrated into the

model to capture these effects, which is an important direction for future model development.

# CHAPTER 3. MIRCOGEL KINETICS

## 3.1 Introduction

Biofriendly microgels, like PNIPAM and dextran, find numerous applications as microscopic delivery agents for advanced therapies of cancer, diabetes, and bacterial infections [28, 95]. The release of the embedded drugs/nanoparticles from the microgel matrix is often achieved via passive diffusion [96-98]. In this case the release rate strongly depends on the drug/nanoparticle size, network mesh size, and microgel radius [99]. Typically the drug/nanoparticle size is limited to no more than 200 nm [100, 101]. Passive diffusion is usually a slow process. For many systems the drug/nanoparticle release occurs over the course of hours/days [102, 103], which can limit the effectiveness of many therapies.

For responsive microgels release of embedded drugs/nanoparticles could be initiated via external stimuli, which causes the polymer network to deswell [2-5]. In this case deswelling proceeds via a “squeeze-out” mechanism. The squeeze-out mechanism however can also be a slow process due to the formation of a dehydrated "skin layer” or shell at the gel-solvent interphase. The formation of the dehydrated layer is initiated during deswelling as microgel-solvent interactions become unfavorable. The dehydrated skin layer hinders solvent migration from the microgel interior which arrests the kinetics of the collapsing microgel [1, 55, 56]. The trapped solvent inside the microgel core is eventually squeezed out of the network as hydrostatic pressure in the gel builds up over time. This squeeze out process can take hours/days to complete in some cases, depending on the initial

swollen gel size [57, 104]. If the hydrostatic pressure is not large enough to compress the microgel significantly, drug/nanoparticle release can be effectively stopped.

For certain microgel systems however deswelling does not lead to skin layer formation [55, 105]. Indeed, little is known about the conditions under which the dehydrated skin layer forms. Experimentally it has been shown that when skin layer formation is avoided microgel response times can be on the order of nanoseconds (for $\sim 0.5\ \mu m$ in diameter microgels) [105]. The presence of the dehydrated skin layer hence can have a profound effect on microgel-based drug therapies [95]. Obtaining a deeper understanding of the microgel kinetics is a critical step to developing more effective treatments for diseases like diabetes and cancer [100, 106].

The aim of the current work is to utilize mesoscale computational modelling to understand how structural network parameters affect microgel kinetics. This will be accomplished using the microgel model introduced in Chapter 2. Initially we will examine how microgel swelling proceeds for microgels with different, chain lengths, crosslink densities, and sizes. Our data will be validated against Tanaka's theory for swelling which has been shown to capture experimental trends well [9, 107]. After this we will examine how deswelling proceeds and compare our results to our previous findings for swelling. Lastly, we will examine under which conditions skin layer formation occurs. Doing this we will highlight the impact of skin layer formation on the swelling ratio and microgel mechanics.

## 3.2 Microgel Kinetics

When the gel undergoes a volume transition, the kinetics of this process are defined by a balance among osmotic pressure, gel elasticity, and viscous drag due to the solvent penetrating in or out of the gel network. The swelling kinetics of a spherical gel can be analyzed analytically [9]. The change of the gel radius is given by $\Delta r(t) = \Delta r_0 \frac{6}{\pi^2} \sum_n n^{-2} e^{-n^2 t \tau^{-1}}$, where $\Delta r_0 = r_{final} - r_{ini}$ is the total increase in the radius, with $r_{final}$ and $r_{ini}$ being the final and initial equilibrated gel radii, respectively, $\tau_{char}$ is the characteristic time constant, and $t$ is time. The time constant is given by $\tau_{char} = r_{final}^2/D$, where $D = (K + 4G/3)/f$ is the collective diffusion of the gel characterizing its elastic relaxation in a viscous solvent. Here, $K$ is the bulk modulus, $G$ is the shear modulus, and $f$ is the friction coefficient between the polymer network and the fluid. Note that as in Chapter 2 all dimensional parameters are expressed in DPD units, unless indicated otherwise.

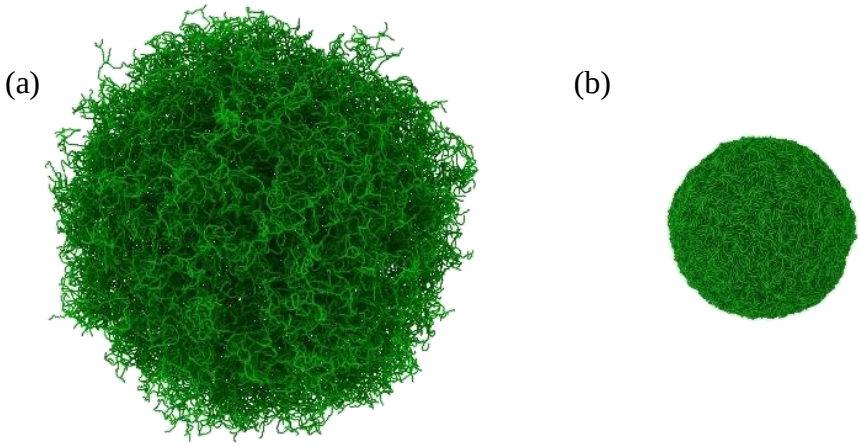


**Figure 3.1**. (a) Swollen particle in good solvent $a = 25$. (b) Deswollen particle in bad solvent $a = 35$.

To examine whether our mesoscale microgel model can properly describe swelling kinetics, we simulate swelling of a spherical microgel that is initially in the collapsed state

($a = 35$). At $t = 0$, the collapsed gel is placed in a good solvent ($a = 20$) and allowed to equilibrate. The collapsed and swollen states are illustrated in Figure 3.1. In our simulations, we track how the microgel radius changes as the microgel undergoes swelling in the good solvent. The results of the simulations for different chain lengths $N$ are shown in Figure 3.2a. As a result of the fitting we find that $\tau_{char}$ increases roughly proportional to $N^2$, whereas the collective diffusion $D$ decreases with increasing $N$ [108]. Hence, networks with longer chains swell slower than networks with smaller chains. The plot in the figure shows that our simulations agree well with the theory for all $N$, indicating that our microgel model can properly capture microgel interactions with the viscous solvent.

In Figure 3.2b we illustrate results for different microgel sizes and network porosities. The polymer networks in Figure 3.2b are constructed using $N = 12$ and $k_{bend} = 5$. The porosity is varied from 65% ($P_{65}$) to 93% ($P_{93}$) by changing the crosslinker concentration. For these two porosities we generate the larger networks first and then cut out the smaller networks from these two samples. As mentioned in Chapter 2 the material

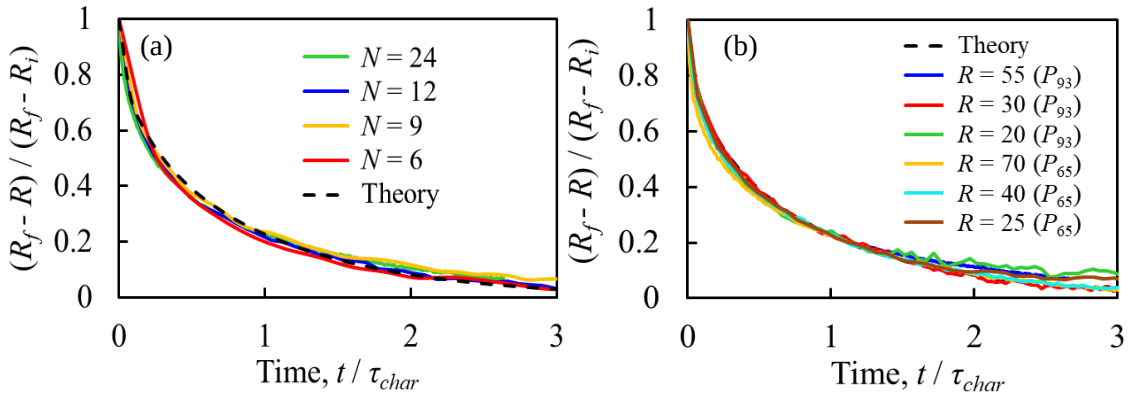


**Figure 3.2**. (a) Swelling kinetics for spherical microgels from Chapter 2 transitioning from collapsed to swollen state. (b) Swelling kinetics for microgels ($N = 12$ and $k_{bend} = 5$) with different porosities and sizes. In all cases we see good agreement between simulations and theory indicating swelling is well described by a single time constant.

that is cut is removed via a depth-first search algorithm [90]. For all cases we see that the computational model adheres to Tanaka's theory very well. Thus regardless of the microgel structure or size in all cases we see that swelling is well described by a single time constant as suggested by Tanaka [9]. Figure 3.3 shows that the relaxation time increases with

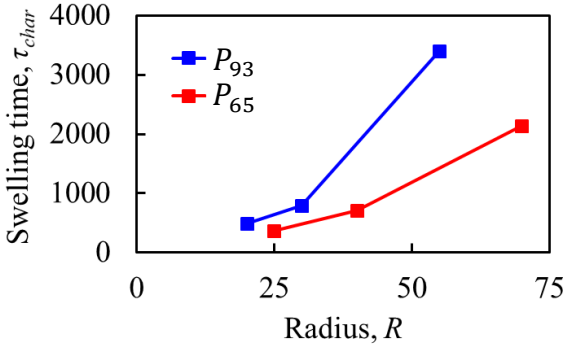


**Figure 3.3**. Swelling time for networks from Figure 3.2b. Networks with larger porosities have longer relaxation/swelling times.

porosity and microgel size. The $P_{93}$ networks are mechanically softer indicating that the swelling time should increase with decreases in the microgel moduli. For larger gel particles the swelling time increases because a larger quantity of solvent has to be expelled from the microgel network. Interestingly, as the microgel size increases the disparity in swelling times between $P_{93}$ and $P_{65}$ microgels increases.

We also examine the microgel kinetics during deswelling, as shown in Figure 3.4. To deswell a given microgel, the initially swollen spherical microgel ($a = 20$) is introduced to a bad solvent ($a = 35$). The time evolution of the microgel size during deswelling is shown in Figure 3.4. We find that for microgels with high porosity ($P \approx 86\% - 95\%$, Figure 3.4a-b) the deswelling kinetics can also be fitted to Tanaka's theory, although the agreement is somewhat less accurate when compared to the swelling process. For these microgels the kinetics for deswelling are faster than swelling. For $P_{65}$ polymer networks (Figure 3.4c), the kinetics are not in good agreement with Tanaka's theory. This

indicates that for $P_{65}$ the deswelling process cannot be described by a single time constant. For $P_{65}$ we find that the kinetics for swelling are faster than deswelling.

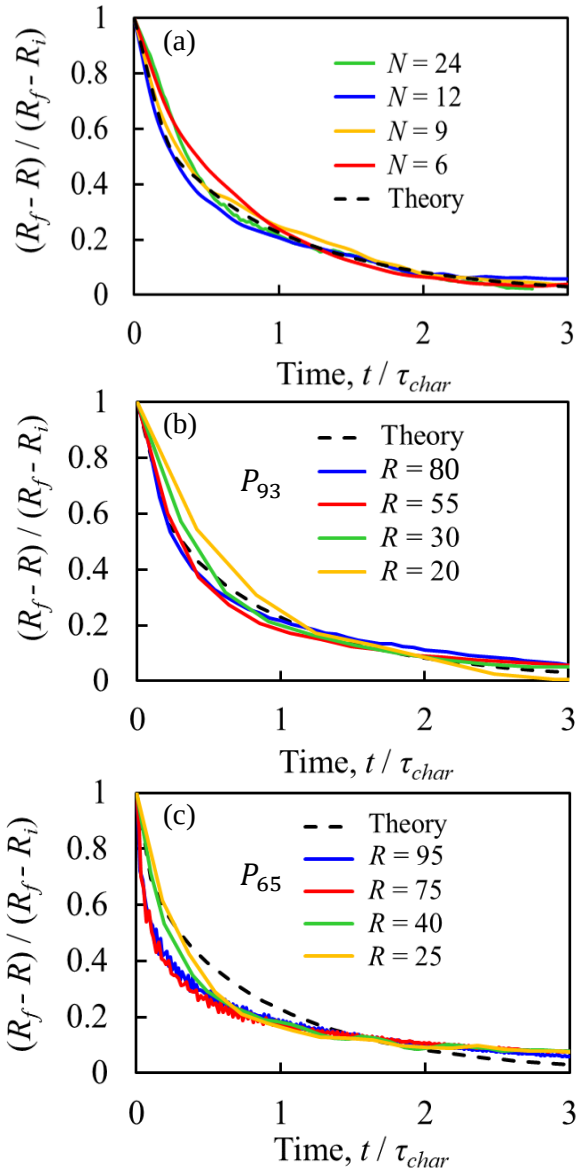


**Figure 3.4**. (a) Kinetics for spherical microgels from Chapter 2 transitioning from swollen to collapsed state. (b) Deswelling kinetics for high porosity microgels ($N = 12$ and $k_{bend} = 5$). (a-b) For higher porosity microgels ($P \approx 86\% - 95\%$) good agreement between simulations and theory is observed for sizes and structures considered here. This indicates that for these cases swelling is well described by a single time constant. (c) Deswelling kinetics for low porosity microgels ($N = 12$ and $k_{bend} = 5$). Deviations from Tanaka's theory increase as the microgel size increases. Results for low porosity microgels indicate deswelling cannot be described by a single time constant.

Figure 3.5 shows snapshots of $P_{93}$ microgel with $N = 12$ that undergoes swelling (Figure 3.5a) and deswelling (Figure 3.5b) transitions. During swelling the microgel gradually increases in size while maintaining a nearly homogeneous structure (Figure 3.5a). In contrast, during deswelling, the microgel exhibits a remarkably different internal structure at intermediate times. Our simulations indicate that deswelling from a fully swollen state proceeds through network coarsening that manifests as formation of chain bundles throughout the microgel (Figure 3.5b). Similar coarsening behavior has been reported for isochore phase separation in hydrogels [109]. Eventually, however, the microgel volume decreases and the solvent is expelled, allowing the microgel to shrink to its collapsed size. Note, that this process is different from rapid deswelling of mm sized macrogels, whereby a skin of collapsed gel is formed on the outer gel surface. This dense skin prevents solvent transfer from the hydrogel interior, thereby delaying the gel deswelling [110]. As it will be shown in the next section, the skin layer can also be generated at smaller microgel sizes if the microgel porosity is lowered.

So far, we have only looked at how the kinetics change between the swollen ($a = 20$) and collapsed ($a = 35$) states. We can however also study the kinetics at intermediate states [8]. This allows us to characterize how the relaxation time and diffusion coefficient change throughout the volume phase transition. To achieve this, we start at $a = 20$ and increase $a$ in small increments up to $a = 35$. For each jump in the network-solvent repulsion we track how the microgel radius changes and fit the corresponding data to Tanaka's theory for swelling. The maximum change in the microgel radius as $a$ is varied is 10%. The corresponding results are shown in Figure 3.6 below. From the plot in Figure 3.6a we can see that the diffusion coefficient is minimized near the critical point. This is in

good agreement with experimental results for PNIPAM microgels [8]. Experimental findings also suggest that near the critical point, when the slope of the swelling curve is nearly vertical, the relaxation time becomes very slow [8]. The plot in Figure 3.6b shows this exact trend, as gel deswelling becomes more than an order of magnitude slower near the critical point.

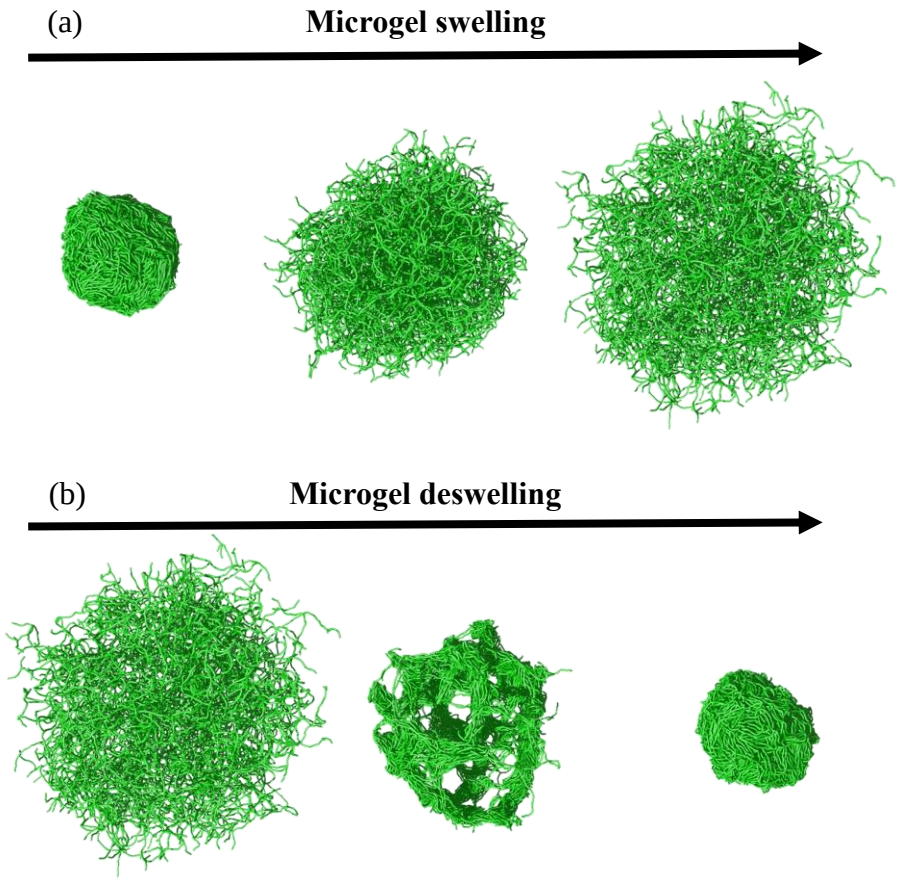


**Figure 3.5**. Simulation snapshots illustrating a microgel network with $N = 12$ during (a) swelling and (b) deswelling. The bad and good solvent conditions are modelled using $a = 35$ and $a = 20$, respectively. Swelling is a homogeneous process. Large structural heterogeneities observed during deswelling as polymer chains bundle together to avoid solvent.

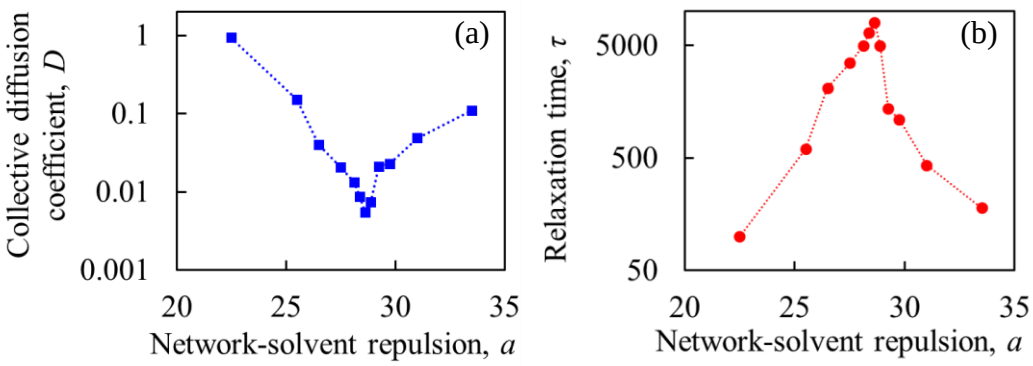


**Figure 3.6**. (a) Plot showing variation in collective diffusion coefficient $D$ throughout the volume phase transition. (b) Plot showing how the relaxation time changes throughout the volume phase transition. The data presented is for $N = 12$ with porosity $P_{93}$. The dotted lines are guides to the eye.

### 3.3 Kinetic Arrest

As shown in Figure 3.4c, for certain microgels, when transitioning from a swollen ($a = 25$) to a collapsed state ($a = 35$), the deswelling kinetics cannot be described well by Tanaka's theory. In these cases, we find that deswelling cannot be described by a single time constant. Examining the microgel network structure for particle $R = 95$ with $P_{65}$ in Figure 3.7, we find that deswelling initially manifests in chain bundling as shown in Figure 3.5b. Before the microgel could equilibrate to the collapsed state however, a dehydrated skin layer develops near the gel-solvent interface. This skin layer arrests the kinetics of the particle by preventing solvent from leaving the microgel interior. Figure 3.7 shows a series of cross-sectional snapshots which illustrate how chain bundling helps coarsen the internal microgel structure and ultimately leads to skin layer formation. Figures 3.5 and 3.7 highlight the fact that skin layer formation is highly dependent on the microgel properties.

Figure 3.8a below shows how the polymer volume fraction $\phi$ varies radially throughout the microgel with time, once deswelling has been triggered. Here $\tau_v$ is the viscous timescale, $\tau_v = l_1^2/\upsilon_{solv}$, where $\upsilon_{solv} \approx 0.283$ is the solvent viscosity, and $l_1 \approx 1.5$ is the approximate network mesh size. The plot shows that in the skin layer indeed the polymer volume fraction is quite high, $\phi \approx 96\%$. For analysis purposes once $\phi$ has reached $90\%$ we consider the skin layer to be fully formed. Figure 3.8b shows that the timescale for skin layer formation $\tau_{skin}$ varies linearly with the microgel size. Considering that the timescale for deswelling (up to skin layer formation) varies quadratically with the particle radius [9, 107], it becomes conceivable that for each microgel network a crossover point exists [8].

Below this crossover point the timescale for deswelling is less than or equal than $\tau_{skin}$. As a result, the microgel equilibrates to the collapsed state before the skin layer has had a chance to form, as shown in Figure 3.5. Above the crossover point $\tau_{skin}$ is smaller than the timescale for deswelling, which leads to kinetic arrest as the skin layer traps

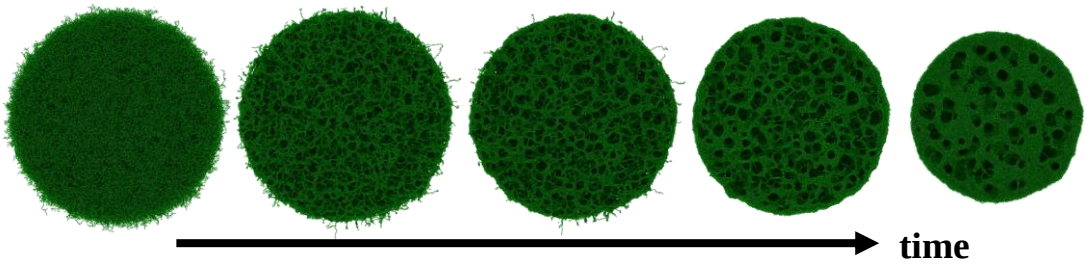


**Figure 3.7**. Cross-sectional images of spherical microgel showing microstructural changes during network collapse. The microgel properties are $N = 12$, $P_{65}$, and $R = 95$.

solvent particles inside the microgel, as shown in Figure 3.7. Experimental data shows that for millimeter-cm sized gels like PNIPAM the skin layer is always present [1, 54, 57, 111]. This supports the above hypothesis, since for large $R$ the deswelling timescale would

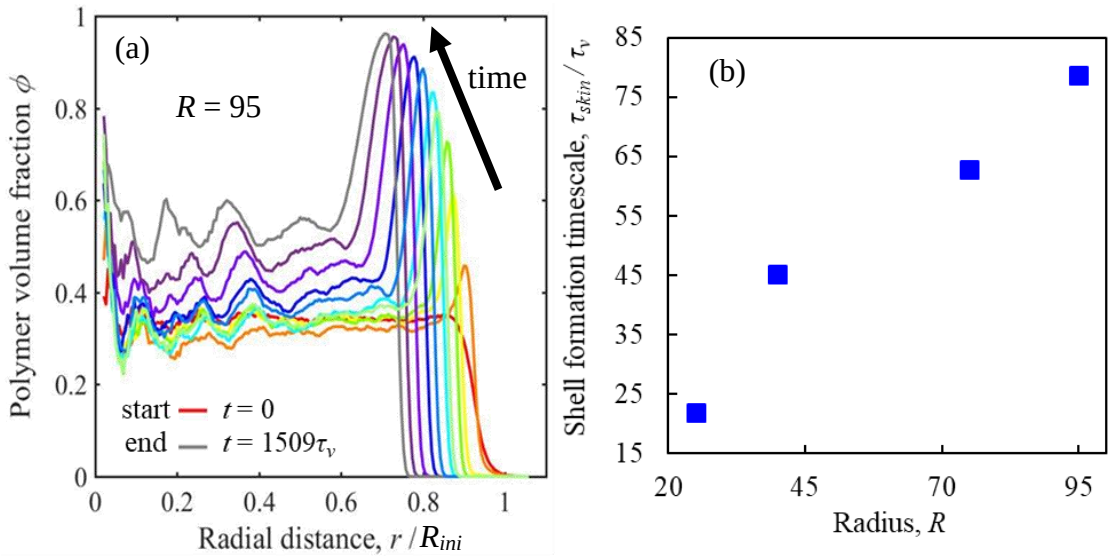


**Figure 3.8**. (a) Plot showing how polymer volume fraction $\phi$ varies radially throughout microgel during deswelling leading up to kinetic arrest. At $t = 1509\tau_v$ the polymer volume fraction is $\phi \approx 0.96$. (b) Plot showing how timescale for skin layer formation varies with microgel size for $P_{65}$ microgels.

dominate. Thus, kinetic arrest is mainly dependent on the crosslink density (porosity) and particle size. For a given microgel the crosslink density affects the mesh size of the network. For example, for $P_{65}$ and $P_{93}$ networks the mesh size is 1.5 and 2.5, respectively. Meanwhile, the crosslink density of $P_{65}$ networks is approximately 3.8 times larger than the crosslink density of $P_{93}$ networks. As the mesh size decreases and chains get closer together bundling and coarsening is accelerated, leading to shorter $\tau_{skin}$.

Comparison in internal microstructure between $P_{65}$ and $P_{93}$ microgels is shown in Figure 3.9 below. Figure 3.9a shows how the polymer volume fraction varies radially in each microgel ($P_{65}$ and $P_{93}$) after 1.2 million timesteps, $t = 1509\tau_v$. In Figure 3.9b-c we show equilibrated side and cross-sectional views of each microgel in $a = 35$. Figure 3.9c shows that when the porosity is large the particle is able to collapse to a nearly dry state. In this case, the plot in Figure 3.9a shows that the skin layer thickness is comparable to the microgel radius (blue curves). Figure 3.9b shows that increasing the crosslink density

makes the dry state inaccessible at this timescale. By increasing the crosslink density $\tau_{skin}$ is shortened which leads to kinetic arrest. In this case the skin layer thickness is much

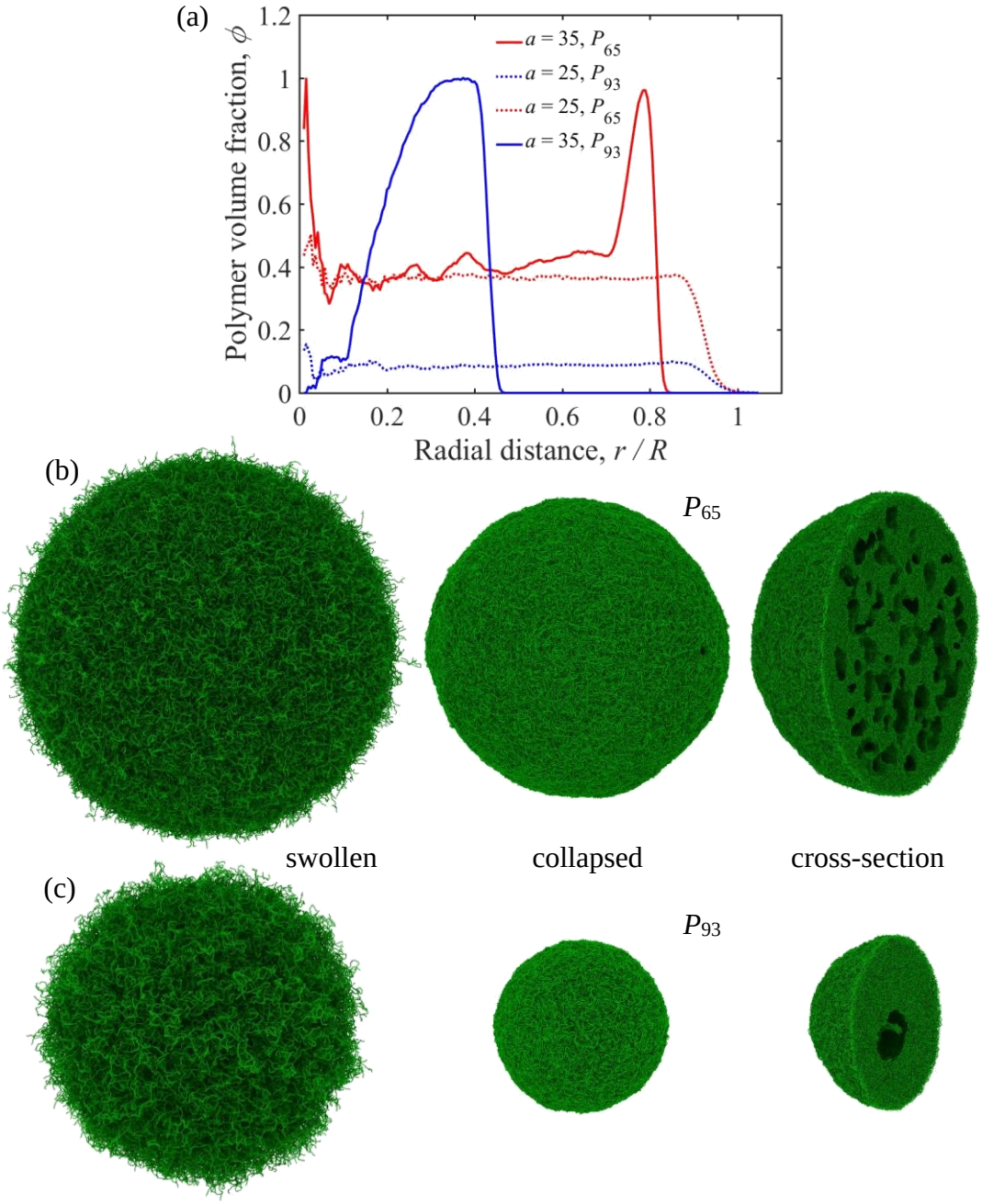


**Figure 3.9**. (a) Polymer volume fraction at $t = 1509\tau_v$ after equilibration in $a = 35$ for $P_{93}$ ($R = 80$) and $P_{65}$ ($R = 95$) microgels. Side and cross-sectional images of $P_{65}$ (b) and $P_{93}$ (c) microgels.

lower, as shown in the plot in Figure 3.9a (red curves). Once the microgel kinetics have been arrested the radius remains constant at short timescales.

Over time thermal fluctuations cause rearrangements in the trapped solvent domains inside the microgel. This can cause solvent domains near the skin layer to escape, leading to a reduction in the particle radius. This phenomenon, however, occurs on a timescale that is several orders of magnitude larger than the timescale for deswelling (without kinetic arrest). Additionally, as more and more solvent domains are released the skin layer grows in thickness which makes it more difficult for the rest of the trapped solvent to escape. In Figure 3.9a, we can see that the polymer volume fraction in the internal coarsened structure is ~60%, when the skin layer is fully formed. This is comparable to what is seen in experiments. Figure 3.9a does indeed indicate that the polymer volume fraction in the skin layer is close to one.

In Figure 3.10a we plot the swelling ratio for microgels with both high and low porosity. The dotted lines in the plot show the theoretical maximum swelling ratio $\alpha_{max}$ based on the swollen and dry states. The solid lines show the swelling ratio $\alpha$ after 1.2

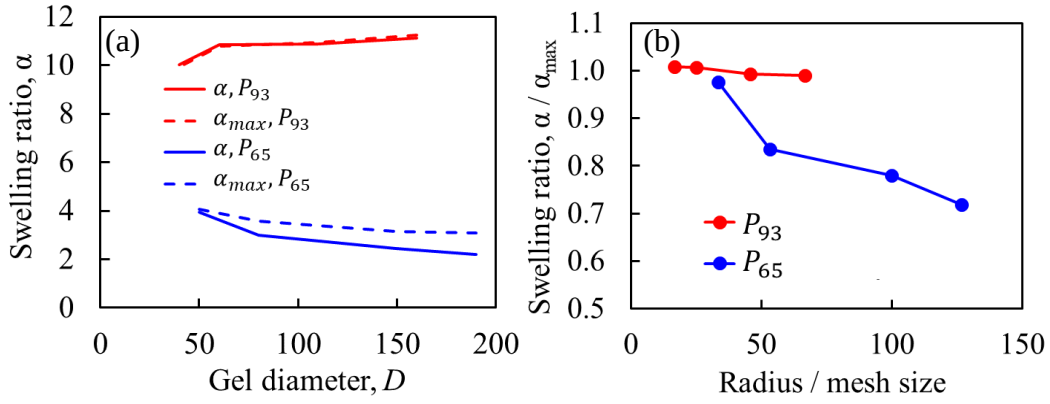


**Figure 3.10**. (a) Swelling ratio as a function of microgel size and porosity. (b) Plot showing how normalized swelling ratio $\alpha/\alpha_{max}$ depends on the radius to mesh size ratio. A normalized swelling ratio below 1 indicates retention of trapped solvent domains in microgel core.

million timesteps of equilibration ($t = 1509\tau_v$). Past this point the microgel has either collapsed to a dry state or entered kinetic arrest. For the high porosity microgels, it is evident that the skin layer does not play a big role since $\alpha \approx \alpha_{max}$. For the low porosity microgels however, the skin layer does make an impact since $\alpha < \alpha_{max}$. Moreover, as the microgel size grows the disparity between $\alpha$ and $\alpha_{max}$ increases. This signifies that to maximize the nanoparticle/drug release from a given microgel the onset of kinetic arrest must be well characterized. A decrease in the microgel porosity decreases the microgel size at which kinetic arrest occurs, as shown in Figure 3.10b. In Figure 3.10b a ratio of $\alpha/\alpha_{max} < 1$ indicates the onset of kinetic arrest.

The results above indicate that nano sized microgel particles may be impervious to the arrested kinetics which larger microgels encounter. Currently the smallest nano-sized gels which can be fabricated have a diameter of about 20-50 nm [63, 101, 112]. Thus, there is a practical limit to how much the size of the gels can be decreased. Furthermore, such small particles have low capacity for encapsulated payload. Thus, it is important to identify structural parameters which can alter $\tau_{skin}$. An interesting direction for future work is investigating how different crosslink distributions alter $\tau_{skin}$. Experimentally most microgels have a normal or Gaussian crosslink distribution [113]. By better understanding how crosslink density and crosslink distribution affect skin layer formation the conditions under which kinetic arrest occurs can be better quantified. This information could then be used to improve existing microgel based drug therapies by helping maximize drug/nanoparticle release rates.

## 3.4 Shape-dependent Instabilities

The formation of the stiff dehydrated shell also has an interesting impact on the mechanics of the microgel particles. As the shell is formed solvent outflow from the microgel core is arrested, leading to isochoric conditions at short time scales. When the gel attempts to deswell under the constraints imposed by the dehydrated skin layer, stress accumulation in the network can lead to mechanical instabilities, such as buckling, which in turn lead to large and rapid magnitude shape changes [1, 54]. Thus, studying stress development in these polymer networks during deswelling could lead to the design of novel microsensors and actuators.

For non-spherical geometries deswelling can lead to lead to out-of-plane buckling [1] if the dehydrated skin layer is present. It has been shown that for toroidal PNIPAM macrogels rapid heating in a thermal bath can lead to increasingly complex buckling modes when the aspect ratio of the torii increases [1]. Once the dehydrated shell forms the volume of the torii becomes effectively fixed, as the kinetics of the network are arrested. Due to this, deswelling occurs under isochoric conditions, which causes the interior domain to form a heterogeneous distribution of distinct solvent and polymer rich phases within the dehydrated skin layer.

For large aspect ratio microgels the distribution of these domains leads to large differences in the internal stresses of the toroid which drives the large-scale buckling deformations. Figure 3.11 shows data of low aspect ratio ($AR$ = handle radius / tube radius) toroidal gel ($AR = 3$) in the collapsed state. The internal voids in the network are highlighted in Figure 3.11.

Modelling buckling in toroidal microgels using the DPD model outlined in Chapter 2 is a computationally expensive task. In order to achieve buckling the skin layer needs to be small compared tube radius. This is important because the higher stiffness of the skin layer (since $\phi_{skin\ layer} \approx 1$) can act to suppress deformations. Experimentally it has also been shown that buckling occurs only for large aspect ratio gels ($AR > 3$) [1]. To satisfy these two requirements the computational domains required are quite large, requiring between 0.5-1 billion particles. The large relaxation times of the polymer networks significantly increase the compute time required as well. As a result of these barriers the current efforts have been limited to examining lower aspect ratio gels ($AR = 3$) where the skin layer thickness is approximately 20% of the tube radius, as shown in Figure 3.11. In this case however, we already see bending of the toroidal tube (Figure 3.11c) and small deformations of the toroidal shape, indicating the onset of buckling.

To confirm whether a stiff toroidal shell can lead to buckling we create a simplified model that is composed of a toroidal shell constructed using a tetrahedral mesh with an average node spacing of~0.35. Nodes in the mesh are connected by harmonic bonds. To mimic the effect of the gel heating rate, we arrange beads along the toroidal centerline and

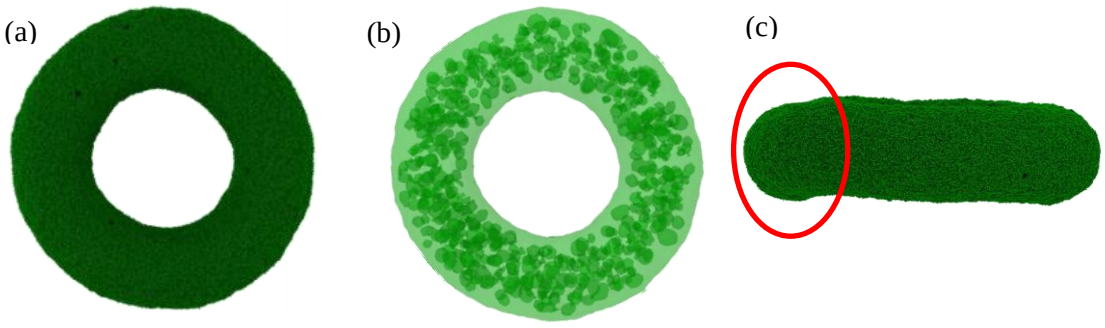


**Figure 3.11**. (a) Top view of deswollen toroidal microgel, $AR = 3$. (b) Top view of semi-transparent surface mesh of deswollen toroidal particle, $AR = 3$. The internal voids can be seen in the darker green color. When deswollen rapidly the toroidal microstructure, internally coarsens becoming very heterogeneous. (c) Side view of toroid showing bending in toroidal tube.

connect them to the beads forming the shell. Mesh-centerline bonds are shown in the cross-sectional view in Figure 3.12, where half of each bond is colored in blue (parts closer to the centerline bead) and the other half is colored in green (portion of the bond closer to the mesh bead). The initial equilibrium bond length for the mesh-centerline bonds was set to 5. The harmonic bonds in the shell have stiffness $k_{bond,s} = 500$, while the mesh-centerline harmonic bonds have stiffness $k_{bond,c} = 100$. Note that we do not impose a DPD repulsion between the beads in the mesh, so that the mesh properties are characterized entirely by the bond stiffness. The repulsion between mesh-solvent beads is $a_{M-S} = 100$. The density of the fluid is $\rho \approx 3$, yielding an average spacing between solvent beads of about 0.7. The smaller spacing between beads in the mesh and the relatively large repulsion between mesh-solvent beads ensures that solvent particles which are initially inside of the toroidal mesh remain trapped during the rapid heating process. To model rapid heating, we instantaneously decrease the

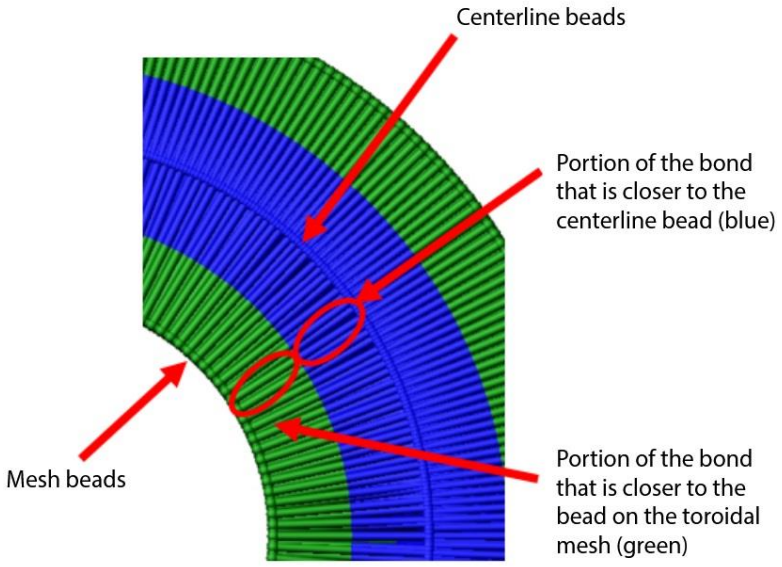


**Figure 3.12**. Cross-sectional view of toroids for rapid heating simulations. The beads in the toroidal mesh and centerline beads are shown in green and blue, respectively. Each mesh-centerline bond is represented with a half-green and a half-blue color scheme for illustration purposes.

mesh-centerline equilibrium bond length from 5 to 3. The final bond length is selected based on the numerical stability of the shell model.

Figure 3.13 illustrates the final buckled shapes for toroids with an aspect ratio of 4 and 5. These large deformations are very similar to what is seen in experiments [1, 54]. Moreover, the model shows that for low aspect ratios buckling is not observed, which also agrees with experiments. The results from the toroidal polymer network model show that a dehydrated skin layer is present during rapid deswelling of toroidal microgels. The method illustrates the highly heterogenous coarsened structure in the toroid interior. The toroidal mesh model then confirms the hypothesis that a stiff external shell which blocks solvent outflow can buckle into highly irregular shapes when strained.

It should be noted that buckling occurs only when the toroid is rapidly deswollen, i.e. instantaneous changes in solvency from $a = 25$ to $a = 35$. If the solvency is changed gradually, experimental results show that the toroidal gel will maintain its shape and aspect ratio throughout the deswelling process [1]. We find the same behavior in our simulations, as shown in Figure 3.14. The good agreement with experimental findings again highlights

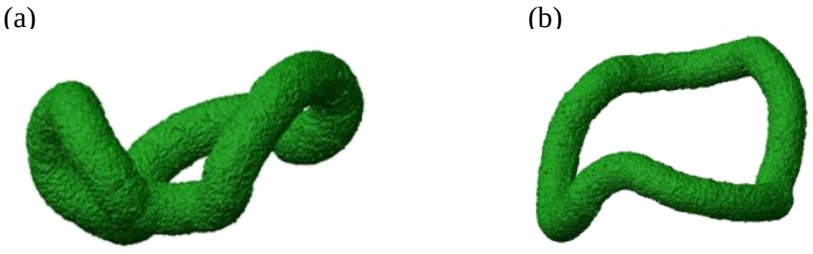


**Figure 3.13**. (a) Buckling of toroidal gel with an aspect ratio of 4. (b) Buckled shape of a toroid with an aspect ratio of 5.

that our microgel model correctly captures the microgel kinetics, as explained in section 3.2.

To generate the toroidal microgels for the quasistatic deswelling study (Figure 3.14) we utilize the random polymer network model from Chapter 2. To construct our toroidal gel network, we randomly distribute crosslink points in a 60×60×60 simulation domain and then connect them with nearby neighbors via flexible chains using a connectivity of 6. The toroidal geometries are cut out from the corresponding cubic networks and placed in a 100×100×100 simulation domain filled with a viscous solvent with density $\rho = 3$ represented by DPD beads. Deswelling of toroidal gels is achieved by varying the gel-solvent repulsion parameter $a$. To model the collapse of the toroidal microgel, we start at $a = 25$ and slowly decrease the solvency until we reach $a = 35$.

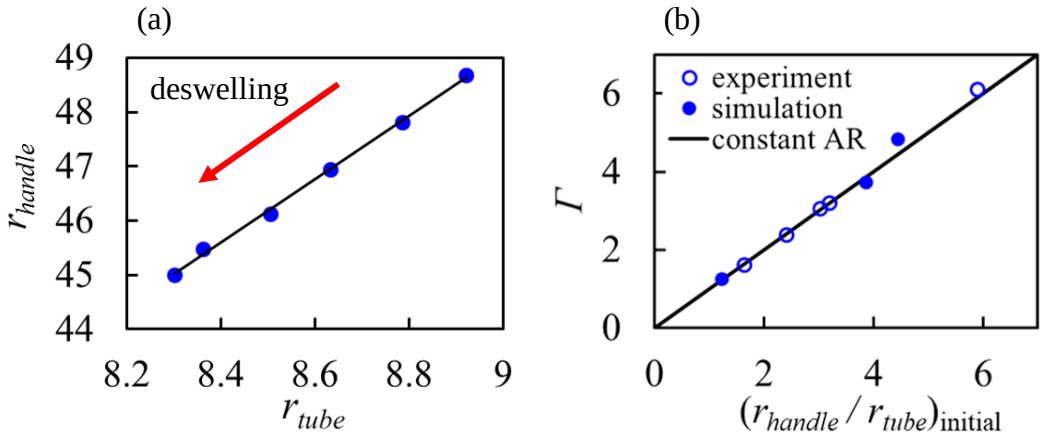


**Figure 3.14**. (a) Slow deswelling of toroidal microgel with an aspect ratio of ~5.8. (b) Comparison between simulations and experiments for slow deswelling of toroidal microgels. Here $\Gamma$ is the slope for $r_{handle}$ vs $r_{tube}$ deswelling data.

### 3.5 Summary

The results presented in this section show that the current mesoscale microgel model captures the kinetics of experimental microgels well. In section 3.2 we illustrated how swelling and deswelling proceed when the dehydrated skin layer is absent. In both

cases we show that the kinetics agree well with Tanaka's theory for swelling, regardless of the microgel size, porosity, or length of constituent chains (Figure 3.2ab and Figure 3.4ab). Additionally, by incrementally varying the solvency of a spherical microgel particle we show that the collective diffusion coefficient of a microgel is minimized near the critical point. As a result of this the relaxation time and network friction coefficient increase by more than an order of magnitude near the critical point. These results are in good agreement with experimental findings.

To characterize the formation of the skin layer, we monitor how the polymer volume fraction varies radially. This analysis shows that the timescale for skin layer formation is linearly dependent on the microgel size. The fact that the timescale for deswelling is quadratically dependent on the microgel radius suggests that for a given microgel network a critical size $R_c$ exists at which the timescale for skin layer formation $\tau_{skin}$ is equal to the timescale for deswelling. For $R < R_c$ it is expected that the timescale for swelling $\tau_{swell}$ will be larger than the timescale for deswelling $\tau_{deswell}$. In this regime the deswelling kinetics are sped up by chain bundling and network coarsening (Figure 3.5). For $R > R_c$ however the particle enters an arrested state which significantly extends the timescale for deswelling. In this regime swelling is expected to be much faster than deswelling. In the special case where $R \approx R_c$ the skin layer thickness is comparable to the microgel radius. Hence by the time the skin layer is formed the microgel is in a nearly dry state. For this case $\tau_{deswell}$ should still be less than $\tau_{swell}$.

Lastly, we illustrate the impact that the dehydrated skin layer can have on the mechanics of toroidal microgels. For toroidal microgels the dehydrated skin layer can

induce buckling for large aspect ratios. In these cases, the bending energy becomes much smaller than the extensional energy. As a result, the toroidal microgels buckle out of plane to equilibrate the internally generated stresses [1]. Such materials could be utilized to create novel sensors which have the ability to both swell/deswell and buckle in response to external stimuli.

# CHAPTER 4. MIRCOGEL MECHANICS

## 4.1 Introduction

The previous two chapters illustrated the large volume changes which microgels undergo near the critical point. As a given microgel particle deswells microgel chains are brought closer together, decreasing the mesh size. The most apparent impact of the decrease in mesh size is the increase in the refractive index. As the particle deswells the diffraction pattern inside the microgel network changes, which increases the turbidity of the gel. As a result the initially transparent network becomes more opaque [114]. Along with these changes near the critical point the mechanical properties also vary greatly. When the microgel is swollen it is soft and deformable, due to the high porosity. In the collapsed state a given microgel becomes several orders of magnitude stiffer, as a large quantity of solvent is expelled from the network.

As outlined in the previous chapter variations in the structural parameters of each polymer network can significantly impact the deswelling kinetics. As illustrated in section 3.2 of Chapter 3 this also has significantly implications on the mechanical properties of each network. In this chapter we illustrate how mechanical properties like the bulk ($K$), shear ($G$), and Young's ($E$) moduli can be measured directly. Consolidating these findings with the kinetic data from the previous chapter helps strengthen our understanding of the microgel behavior near the critical point.

## 4.2 Microgel Mechanics

We measure the bulk modulus of our mesoscale gels by quasi-statically varying the total osmotic pressure imposed on the microgel network. To change the osmotic pressure, we create a semi-permeable spherical shell around the microgel (Figure 4.1). The spherical shell interacts with the gel particles via a harmonic potential, while the solvent particles are allowed to pass freely through the shell. Varying the radius of the spherical shell thus effectively mimics a change in the osmotic pressure. For each solvency $a$, we vary the radius of the semi-permeable shell and evaluate the corresponding network volume and pressure. To find the microgel volume $V$, we construct a surface mesh around the gel. The network pressure is calculated as $\Pi_{network} = W(\sigma_{xx}^{ave} + \sigma_{yy}^{ave} + \sigma_{zz}^{ave})/3V$, where $W$ is the number of microgel beads in the network, and $\sigma_{ii}^{ave}$ is the average normal stress per bead in the $x$, $y$, and $z$ directions. The stress is averaged over all beads in the microgel network.

Figure 4.2a shows the network pressure $\Pi_{network}$ as a function of microgel volume $V$. The pressure is calculated for different values of solvency $a$ at the linear region of microgel compression, where $\Pi_{network}$ is a linear function of $V$ (see the inset in Figure 4.2a). The variation of $\Pi_{network}$ with $V$ in this linear region is used to evaluate microgel bulk modulus as follows $K = V\frac{\Delta\Pi_{network}}{\Delta V}$. This procedure is repeated for different $a$ covering the entire range of microgel swelling transition. As in Chapter 2 all dimensional parameters are expressed in DPD units, unless indicated otherwise.

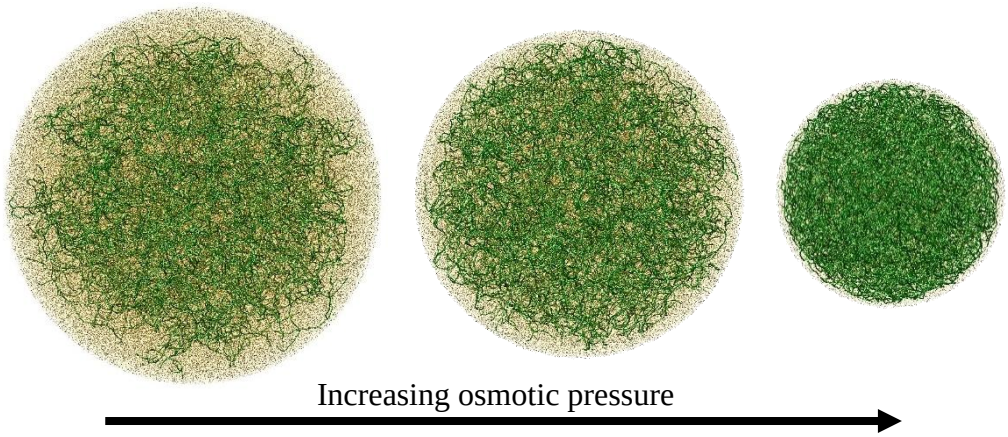


**Figure 4.1**. Illustration of bulk modulus measurements. Images show the microgel inside a spherical shell. Yellow points represent solvent beads while green points represent microgel beads. Decreasing the radius of the semi-permeable shell increases the osmotic pressure on the microgel.

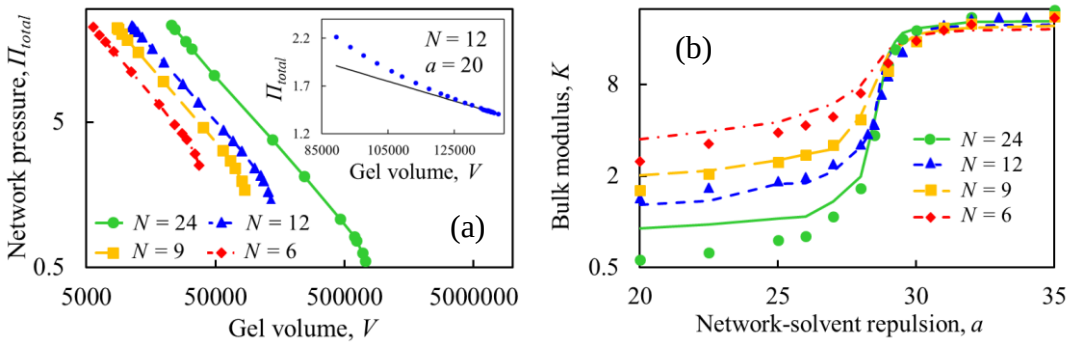


**Figure 4.2**. (a) Network pressure as a function of microgel volume for different chain lengths throughout the volume phase transition. The inset shows network pressure as a function of gel volume for $N = 12$ and $a = 20$. The solid line in the inset represents the slope of the linear region of the microgel deformation. (b) Bulk modulus data from simulations and corresponding fits to the Flory-Rehner theory (solid dashed lines). In bad solvents, all microgels have the same bulk modulus. In good solvents, the microgels with longer chain lengths have a higher porosity and are thus softer.

Figure 4.2b shows the resultant bulk moduli $K$ for microgels with different $N$ through the volume phase transition. We find that the bulk modulus monotonically increases as the solvency decreases. This increase in $K$ is related to a decrease in the microgel porosity and an increase in the crosslink density $\rho_c$ as $a$ increases. In good solvent

$a \lesssim 25$ (swollen state), the bulk modulus decreases with $N$. In this case, increasing $N$ decreases the crosslink density resulting the gels softening. This softening of the microgels with increasing $N$ also leads to a sharper volume phase transition (Figure 2.5a).

Analytically, the microgel bulk modulus can be evaluated using Flory-Rehner theory, which postulates that, for nonionic gels, the total osmotic pressure $\Pi_{total}$ is composed of a mixing osmotic pressure $\Pi_{mix}$ due to polymer-solvent mixing and an elastic osmotic pressure $\Pi_e$ due to network elasticity [13]. Note that $\Pi_{total}$ corresponds to $\Pi_{network}$ in our simulations. At equilibrium with pure solvent, $\Pi_{mix}$ balances $\Pi_e$. Using that $K = \phi \frac{\partial \Pi_{total}}{\partial \phi}$ and Flory's description of $\Pi_{mix}$ and $\Pi_e$, we can obtain an expression for the microgel bulk modulus: $K = \frac{k_b T}{v_s}\left(\frac{N_c}{V_o} v_s \left[\frac{1}{2}\left(\frac{\phi}{\phi_o}\right) - \left(\frac{\phi}{2\phi_o}\right)^{1/3}\right] + \frac{\phi^2}{1-\phi} - 2\chi\phi^2\right)$, where $\phi = 1 - P$ is the polymer volume fraction, $N_c/V_0$ is the number of polymer chains in the preparation state per volume, which corresponds to the nearly collapsed state in our simulations, $v_s$ is the molar volume of the solvent, $\phi_o$ is the volume fraction in the preparation state, and $\chi$ is the solvency parameter. For our microgel, we evaluate the solvent molar volume as $v_s = r_{c,p}^3 N_A/\rho$, where $r_{c,p}$ is the physical size of cutoff radius $r_c$ of the DPD potential, $N_A$ is Avogadro's number, and $\rho$ is the density in our simulations [115].

**Table 4.1**. Fitting parameters from bulk modulus fits

| $N$ | $k_bT/v_s$ | $N_cv_s/V_o$ | $\chi_0$ | $\chi_1$ | $\chi_2$ |
|---|---|---|---|---|---|
| 6 | $1.02\times10^{-21}$ | $4.88\times10^{22}$ | 0.49102 | 0.05018 | 0.50264 |
| 9 | $1.05\times10^{-21}$ | $4.90\times10^{22}$ | 0.50956 | 0.05097 | 0.50783 |
| 12 | $9.97\times10^{-22}$ | $5.28\times10^{22}$ | 0.51357 | 0.05091 | 0.49995 |
| 24 | $1.08\times10^{-21}$ | $5.09\times10^{22}$ | 0.50725 | 0.05 | 0.49755 |

We fit our simulation results for $K$ versus $a$ with Flory-Rehner's theory, using the relation between $\Pi_{total}$, and thus $\phi$, with $a$. We consider the solvency parameter as a function of the polymer volume fraction $\chi = \chi_0 + \chi_1\phi + \chi_2\phi^2$ and set $k_bT/v_s$, $N_cv_s/V_o$, $\chi_0$, $\chi_1$, and $\chi_2$ as fitting parameters. In our simulations, the number of polymer chains per volume in the preparation state is $N_c/V_o \sim 0.25$. The obtained values of the fitting parameters are summarized in Table 1; these are nearly independent of chain length $N$.

The resulting fits to our bulk modulus data correctly describe our simulations results, as shown in Figure 4.2b. We note that if the fits are performed assuming $\chi$ is linearly dependent on $\phi$, good agreement between our simulations and the theory cannot be obtained. Thus, the quadratic dependence of $\chi$ on $\phi$ is essential. This is consistent with previous experiments, and suggests that many-body interactions become important near the swelling transition [13].

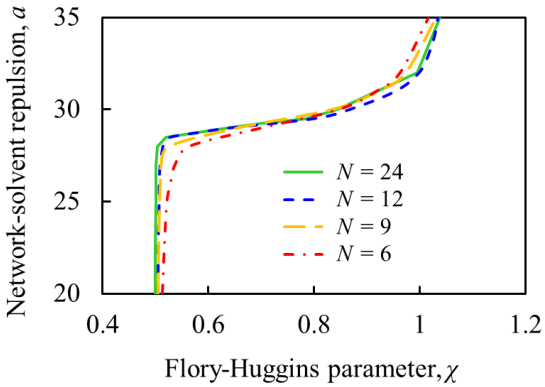


**Figure 4.3**. Relationship between the Flory-Huggins solvency parameter and the network-solvent repulsion in DPD simulations.

Using the results for $\chi$ from the fits, we can connect how this parameter depends on the network-solvent repulsion coefficient $a$. This is shown for different $N$ in Figure 4.3. We find that the $\chi - a$ dependence is not sensitive to the value of $N$. Furthermore, in good solvent the solvency parameter is about 0.5, whereas in bad solvent it increases to ~1. This behavior agrees reasonably well with experimental data [11, 14, 15].

To obtain the shear modulus of our particles we initially calculate the Young's modulus by deforming the microgel particles with 2D plates. For this case the Young's modulus is given as: $E = (1/2r_c)(dL/d\lambda)$, where $r_c$ is the Hertzian contact radius, $L$ is the applied load, and $\lambda$ is the displacement of the plate [116, 117]. The derivative $dL/d\lambda$ can be calculated by tracking the stresses one each plate along with the corresponding displacement $\lambda$. The Young's modulus measurements are taken in the linear stress-strain regime. The compression of a microgel particle is illustrated in Figure 4.4. For each measurement we compress the microgels in the $x$, $y$, and $z$ directions and then average the corresponding results for $E$. Once measurements for $E$ are obtained, we use the relation $G = 3KE / (9K - E)$ for isotropic linear elastic materials. Data for the case $N$ = 12 at

different solvent qualities along with the corresponding comparison to linear poroelastic theory ($G = \frac{N_c}{V} k_b T$) is shown in Figure 4.5 [61]. The plot in Figure 4.5a shows that microgel stiffness increases by about 2 orders of magnitude between good and bad solvent. The poroelastic theory shown in Figure 4.5b captures the trends in our data well. Some deviation from the theory is seen near $a \approx 32$, but this occurs due to the partially collapsed asymmetrical shapes of the gel particles. This is shown in inset of Figure 4.5b. The

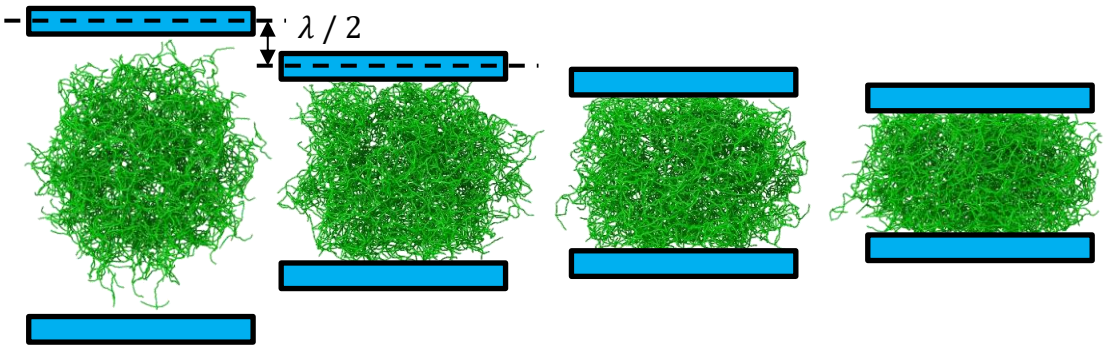


**Figure 4.4**. Illustration showing microgel compression between two plates. Throughout the compression process the force on each plate is calculated allowing the Young's modulus to be determined.

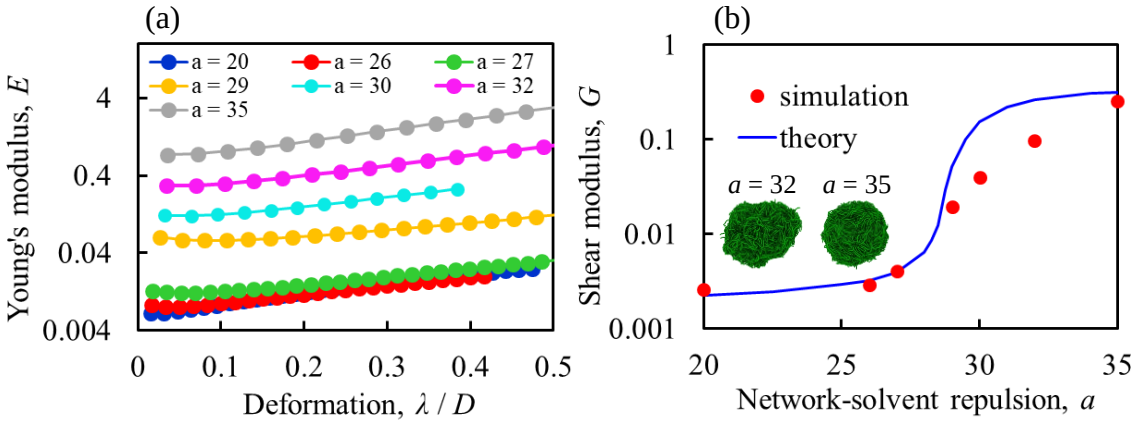


**Figure 4.5**. (a) Plot showing how $E$ changes with strain and solvent quality. As the particle collapses and approaches the dry state the Young's modulus increases approximately an order of magnitude. (b) In this plot we calculate the shear modulus using measurements for $K$ and $E$ and the relation for isotropic linear elastic materials $G = 3KE / (9K - E)$. The theoretical line is based on poroelastic theory.

agreement between simulations and theory in Figure 4.5b signifies that poroelastic theory could be used in leu of the Young's moduli measurements shown in Figure 4.4.

Considering that now both $K$ and $G$ are available, the friction factor of a microgel network with $N = 12$ throughout the swelling transition could be calculated using the data from Chapter 3, according to the relation $f = (K + 4G/3)/D$. The variation in the friction factor with $a$ is illustrated in Figure 4.6. The plot shows that near the critical point ($a \approx 29$) $f$ drastically increases as the collective diffusion coefficient $D$ decreases. The decrease in the collective diffusion coefficient is shown in Figure 3.6a. Away from the critical point in good solvent ($a \approx 25$) the friction coefficient is in the range of 2-10. Meanwhile in the bad solvent regime ($a \approx 32 - 35$) $f$ varies between 200-400.

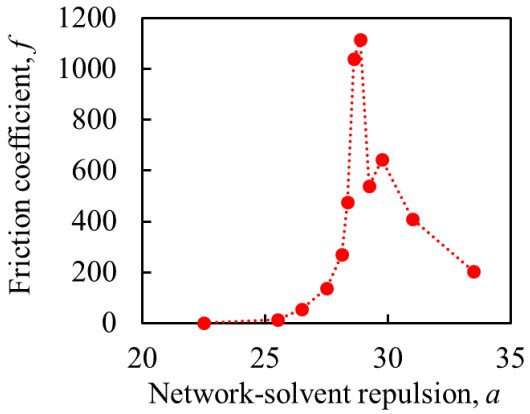


**Figure 4.6**. Plot showing how the friction coefficient changes throughout the swelling transition for a microgel network with $N = 12$. In good solvent ($a \approx 25$) the friction coefficient is approximatelly 2-10. In bad solvent ($a \approx 32 - 35$) $f$ ranges between 200-400, which represents more than an order of magnitude increase. Near the critical point ($a \approx 29$) $f$ is maximum, due to the significant decrease in $D$.

## 4.3 Summary

At this point we have characterized the variations in $K$, $E$, and $D$ independently, which has also allowed us to infer how $G$ and $f$ vary with solvency. The changes in the bulk modulus show good agreement with Flory-Rehner theory. More importantly, the

trends seen in experiments are captured well. In Chapter 2 we showed that as $N$ increases the volume phase transition becomes sharper. Previously, Hirotsu has indicated that this trend occurs due to a softening of the microgel networks [10]. The data in Figure 4.2b confirms that. Figure 4.2b shows that as the average number of beads per chain $N$ increases the bulk modulus $K$ in good solvent decreases. In addition, the Flory-Rehner fitting allows us to establish a connection between the network-solvent repulsion parameter in our DPD simulations and the experimentally trackable Flory-Huggins parameter.

We also showed that by compressing each microgel particle with 2D plates we can determine the Young's modulus. This procedure can be carried out for different microgel networks and different solvent conditions. An important observation in our measurements is that at different solvencies asymmetrical shapes can produce different values for $E$ depending on the direction of compression. Using the obtained Young's modulus data, we showed that the corresponding shear moduli $G$ values are in good agreement with poroelastic theory, which has been shown to describe experimental microgels well.

Lastly, we demonstrated that the mechanical measurements, coupled with the collective diffusion coefficient computations, from Chapter 3, can be used to determine the friction coefficient for a given microgel network. The results show that near the critical point the friction coefficient increases significantly owing to the decreasing collective diffusion coefficient. In the next chapter we build on the previous results by examining the collective behavior of microgel particles in a suspension at different packing fractions and solvent conditions.

# CHAPTER 5. COMPRESSED MICROGEL SUSPENSIONS

## 5.1 Introduction

Microgels suspensions are a class of soft matter systems with a very diverse and rich mechanical behavior [58-61, 91, 114, 118, 119]. The unique character of these systems is owed to the soft and responsive nature of the constituent microgel particles which typically vary in size from $50\ nm$ to $10\ \mu m$ [63, 113]. Microgels consist of fully flexible polymer chains which are chemically linked at crosslinking sites [120, 121]. The flexibility of the polymer chains imparts on each network a high degree of deformability [92]. The distribution of crosslinking sites throughout the microgel volume strongly impacts the shape, mechanics, and structure of the microgel [113].

Typically, microgels have a relatively low degree of crosslinking that allows these particles to obtain high porosities in the swollen state [59, 91]. When the solubility of the network is changed an osmotic pressure difference arises [13] that leads to network collapse, often resulting in a 10 and even 100-fold decrease in the microgel volume [122-124]. The large changes in volume and network internal structure yield discernable changes to the microgel mechanics drastically altering the bulk mechanical properties of microgel suspensions, as shown in Chapter 4. Variation in the solvency introduces an attractive force between polymer chains, which lead to microgel-microgel interpenetration [114]. Experimentally measuring the degree of interpenetration and deformation of individual microgels in the suspension is challenging, which makes understanding the impact on the mechanics of the suspension difficult [125, 126]. In this regard computational modelling

offers a unique opportunity to gain insight into the behavior of individual microgels at a variety of packing states and solvent conditions.

For suspensions of rigid particles, suspension properties are well described by the packing fraction, $\varphi = \kappa V / V_{sus}$, where $\kappa$ is the number of particles in a suspension with volume $V_{sus}$, and $V$ is the volume of a single particle. This definition relies on the instantaneous volume $V$, which in the case of rigid particles is constant, and leads to $\varphi < 1$. In the case of microgel suspensions, the microgel volume can vary significantly due to compression or variations in the solvency. We therefore introduce a generalized packing fraction, $\psi = \kappa V_{eq} / V_{sus}$, which uses the equilibrium microgel volume in dilute conditions $V_{eq}$ as a reference point. In a dilute suspension $V_{eq}$ approaches $V$ and thus $\psi \approx \varphi$, but as compression increases $\psi$ can increase significantly above one.

## 5.2 Computational Setup

Our simulations are conducted within the DPD framework outlined in Chapter 2, where we use beads with mass $m = 1$, $r_C = 1$, $\gamma = 4.5$, $k_B T = 1$ [70]. The integration time step is set to $\Delta t = 0.01$. Henceforth, all dimensional parameters are expressed in DPD units, unless indicated otherwise. All simulations are carried out using the LAMMPS software [127]. We use a bead-spring model to model individual microgel particles in the microgel suspension. Following our previous work from Chapters 2-4, for our bead-spring model we set $r_{c_{SRP}} = 0.5$, $C = 100$, $k_{bond} = 35$, $r_{eq} = 0.6$, and $k_{bend} = 5$ [120].

To mimic changes in the microgel solvability, we vary the repulsion between polymer and solvent beads $a$ in the range of 25-35 [120]. All other bead-bead interactions

$a_{ij}$ are set to 25. Good solvent is represented by $a = 25$ (swollen state), whereas $a = 35$ represents bad solvent (collapsed state). When $a$ is varied from 25 to 35, microgels undergo a reversible volume phase transition from a fully swollen to a fully collapsed state [120].

Figure 5.1 illustrates the four different microgel particles we used to construct our suspensions. The corresponding polymer network properties for each network are given in Table 5.1. Gel networks in Figures 5.1b and 1c are created by randomly distributing crosslink points that are then randomly connected by polymer chains [87]. The spatial distribution of crosslinkers in these gels is schematically shown in Figure 5.1a. In Figures 5.1e and 5.1f, we show microgel particles with crosslinkers that follow the normal distribution, $f(x) = \frac{1}{\sqrt{2\pi(2R/3)^2}} e^{-0.5x^2/(2R/3)^2}$ relative to the particle center, where $R$ is the microgel radius. This crosslinker distribution is illustrated in Figure 5.1d. Each crosslinker is limited to have a maximum of four connections. The polymer networks with normal crosslinker distribution are selected to more closely represent the crosslinking structure of experimental microgels [128]. Experimentally, comonomer reactivity rates usually differ, which restricts most microgels to have a normal or Gaussian crosslink distribution [113]. In these cases, the majority of polymer chains are located near the

particle center/core, where most of the crosslinking occurs. Near the gel-solvent interface the sparse distribution of crosslinking sites creates an irregular surface comprised of long dangling chains. For PNIPAM particles however, regularization of the polymerization process makes it possible to create microgel particles with a nearly uniform crosslink distribution [113]. These polymer networks have a homogeneous polymer chain distribution, as a result of the even distribution of crosslinking sites.

**Table 5.1**. Structural parameters for microgel networks

| Microgel particle | Crosslink distribution | Monomers | Crosslinkers | Average beads per chain | Swollen volume | % crosslinker by number |
|---|---|---|---|---|---|---|
| I | Uniform | 34,080 | 1,840 | 12 | 99,000 | 5.4 |
| II | Uniform | 35,030 | 845 | 20 | 132,000 | 2.4 |
| III | Normal | 48,236 | 2,903 | 11 | 135,000 | 6 |
| IV | Normal | 34,674 | 1,632 | 12 | 119,000 | 4.7 |

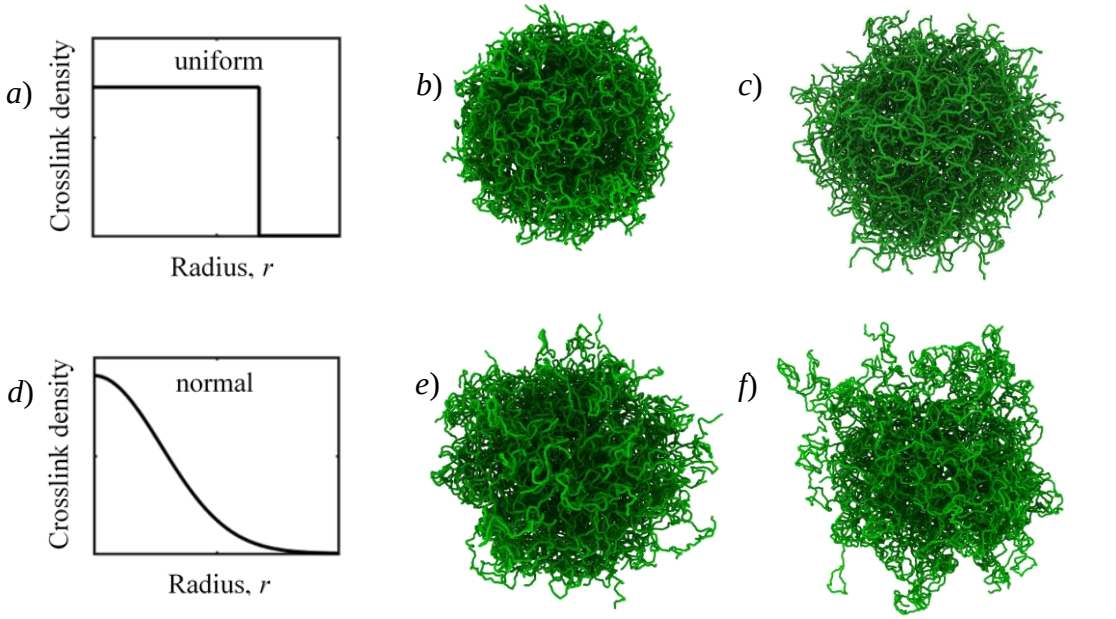


**Figure 5.1**. (a-d) Illustration of different microgel particles in swollen state used to construct suspensions. The plots in figure (a) and (d) illustrate what the crosslink distribution in each network looks like. Microgel particles I and II, which have a uniform crosslinker distribution are shown in (b) and (c), respectively. These particles tend to have on average fewer dangling chains than particles with a normal crosslink distribution. Particles III and IV, which have a normal crosslinker distribution are shown in (e) and (f), respectively. Particles (b), (c), and (f) have approximately the same number of monomers, whereas the number of monomers of particle (e) is approximately 40% higher than other particles.

The microgels in Figures 5.1b, 5.1c, and 5.1f have approximately the same number of monomers and hence have similar molecular weights, whereas the microgel in Figure 5.1e has a roughly 40% higher molecular weight. Figure 5.1e-f shows that microgels with a normal crosslink distribution tend to have longer dangling chains at the microgel outer surface. For microgels I, II, and III chain lengths are allowed to vary about 14% around the mean value. Meanwhile, for microgel IV, the chain length varies about 70% around the mean. Thus, while both networks III and IV have normal crosslink distributions the chain length distribution of network IV is much wider. Due to this network IV has much longer dangling chains at gel-solvent interface.

The volume of microgels is defined using a surface mesh that is constructed using a probe with a radius of about 2/3 of the average crosslink spacing. Such probe size corresponds to approximately 0.45 of the contour length of each chain. The crosslinking distance and chain length are evaluated for each network after equilibration in good solvent. We find that the use of a smaller probe radius can result in large voids inside the microgel. On the other hand, a larger probe radius does not allow us to capture minute changes in the volume occurring at the microgel surface. Surface meshing is done using the OVITO software [94], where internal voids in the mesh are removed [129, 130].

To create the microgel suspensions, we introduce $\kappa = 106$ identical microgel particles into a cubic computational domain with periodical boundaries and volume $V_{box}$. The packing fraction $\psi$ is defined as $\psi = \kappa V_{eq}/V_{box}$ , where $V_{eq}$ is the equilibrium volume of an isolated microgel at given solvent condition. In this study, we examine the suspension behavior when the packing fraction $\psi$ is varied by either changing $V_{eq}$ or $V_{box}$, which we refer to as the solvency method and the volumetric method for changing $\psi$, respectively.

In the volumetric method, we keep the network solvency fixed and vary $V_{box}$ to alter $\psi$ in the range between 0.2 and 5.5. To this end, the computational box is deformed in 0.2 box increments per 10,000 timesteps along each dimension. Once the required packing fraction is obtained, the suspension is equilibrated for an additional 500,000 timesteps. The largest computational box used in the simulations is $300 \times 300 \times 300$. The suspensions with low packing fractions $\psi < 0.5$ are generated by removing microgels from the suspension. The total particle density in the computational box is maintained at $\rho = 3$ [120]. Figures 5.2a-d illustrate the volumetric compression of a suspension of uniformly crosslinked microgels I.

## 5.3 Characterizing Individual Microgels in Suspension

Microgel suspensions are composed of highly compressible microgel particles that in the swollen state can retain a large quantity of liquid, with porosity $P = N_{solvent}/N_{total} > 0.9$, where $N_{solvent}$ is the number of solvent beads inside the microgel and $N_{total}$ is the total number of solvent and chain beads in the microgel. This gives microgel suspensions the ability to deform significantly when volumetrically compressed by external forces that drive the solvent out from the suspension. Thus, in contrast to rigid colloids, compressed microgel suspensions can have generalized packing fraction $\psi$ significantly exceeding one. Furthermore, for many microgel particles, solvent conditions

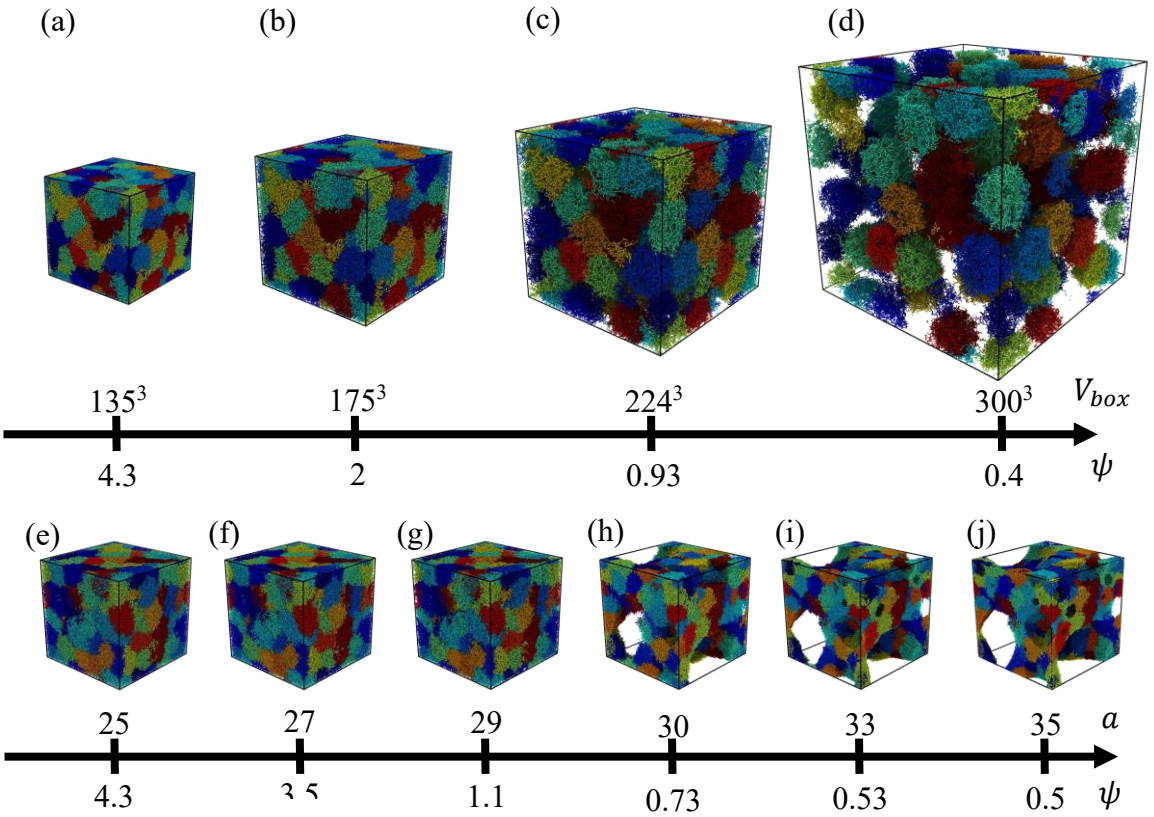


**Figure 5.2**. (a-d) Snapshots illustrating a decrease in $\psi$ for the volumetric method in suspension I. (e-j) Snapshots illustrating a decrease in $\psi$ for the solvency method in suspension I. Images (a) and (e) correspond to high compression in good solvent, $a = 25$ and $\psi = 4.3$. (g-h) The critical point for the solvency method occurs between $a = 29 - 30$. The volumetric (d) and solvency (j) methods produce very different low $\psi$ states.

could be varied via environmental stimuli, such as temperature and pH, thereby causing microgels to change their equilibrium volume $V_{eq}$. Thus, solvency change can be also used to alter $\psi$ for suspensions with fixed volume. Note that the change in solvency also affects interparticle interactions.

We examine these two different methods for changing $\psi$. As shown in Figure 5.2, both methods yield similar suspension structure at high $\psi > 1$. However, the suspension structure differs noticeably between these two methods at low packing states $\psi < 1$. With the volumetric method (Figure 5.2d), the suspension is in good solvent with microgels evenly distributed, forming a colloidal fluid phase. With the solvency method (Figures 5.2h-j), low packing states are achieved under bad solvent conditions, leading to colloidal gelation and the formation of a space-spanning colloidal microgel network.

In Figure 5.3a, for the volumetric method, we plot the average particle volume in the suspension as a function of the generalized packing fraction for suspensions comprised of microgels with different crosslink distributions. The average particle volume is normalized by $V_{eq25}$, which is the single particle equilibrium volume at solvency $a = 25$ (good solvent). For the volumetric method the particle volume equals $V_{eq25}$ at $\psi < 0.5$, since in this range of $\psi$ the suspension is relatively dilute and the microgels can adopt their equilibrium size and shape. As the generalized packing fraction increases to about 0.67 the particles jam. Figure 5.3a shows that for $0.67 < \psi < 1.5$ the average particle volume decreases as the particles deform and interpenetrate. For $\psi > 1.5$, the volume scales as $V \sim \psi^{-1}$ shown by the solid line in Figure 5.3a. This scaling can be derived with the assumptions that interpenetration is not significant and the volume of compressed

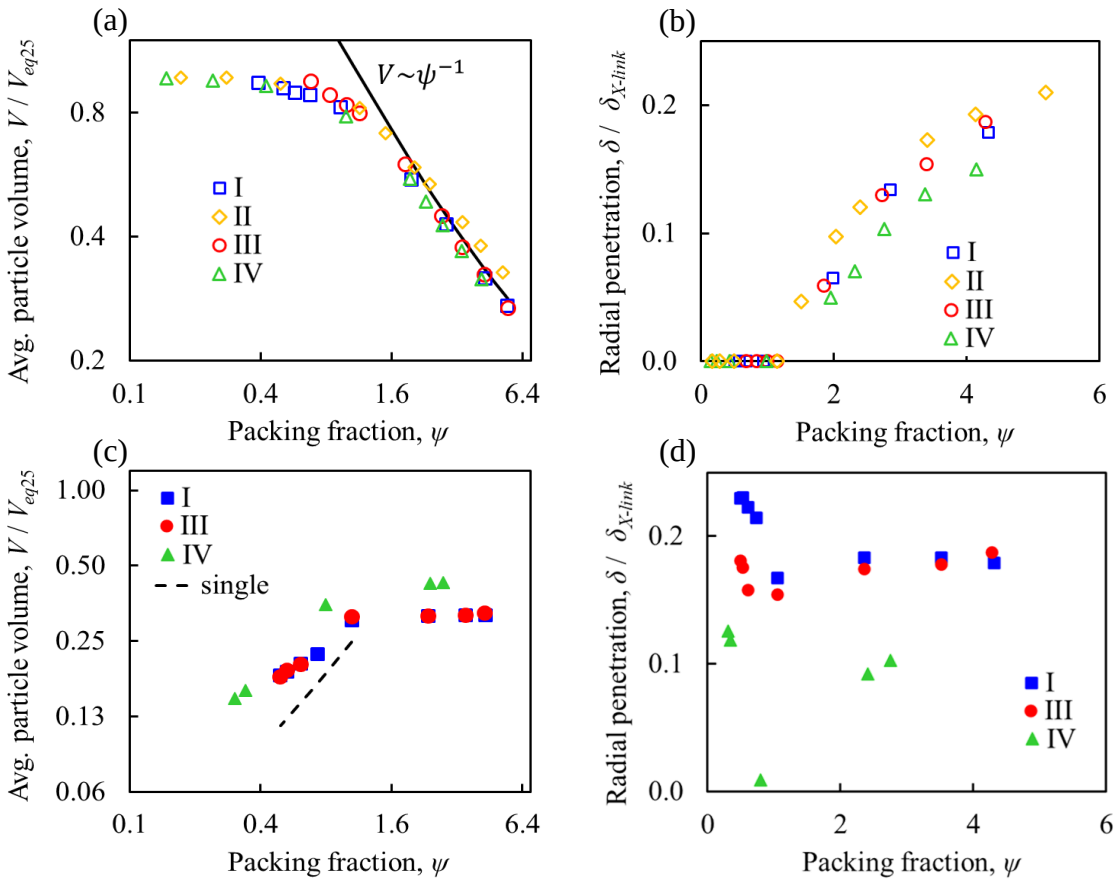


**Figure 5.3.** (a) Plot showing how the average microgel volume in the suspension varies with $\psi$ for volumetric method. (b) Plot showing how the average microgel volume in the suspension varies with $\psi$ for the solvency method. The solid black line in plots (a-b) represents the accessible volume per particle in the suspension, $V_{box}/\kappa$. Here $V_{eq25}$ is the particle volume in good solvent. The dotted line in plot (b) shows the equilibrium volume for microgel I in the bad solvent regime ($29 < a < 35$). Plot of radial penetration data for volumetric (c) and solvency (d) methods. At low $\psi$ large differences in radial penetration are observed between the two methods. For the solvency method, at low packing fractions phase separation leads to an increase in particle-particle penetration, due to gelation.

microgels approaches $V \approx V_{box}/\kappa$ and hence $\psi \approx V_{eq}/V$. The agreement of the simulation results with the $V \sim \psi^{-1}$ scaling indicates that for the volumetric method, at high generalized packing fractions, the suspension changes its volume via deswelling of individual microgel particles and the interpenetration does not play a major role. This is valid for microgels with normal and uniform crosslink distributions, and agrees with experimental data [118, 126, 131].

Figure 5.3b shows the magnitude of radial interpenetration of microgels for the same range of packing fractions as shown in Figure 5.3a. The penetration depth is normalized by the average crosslink distance of the microgel particles. When volumetric compression is applied to the suspension, the degree of interpenetration is nearly zero when $\psi \lesssim 1$ and gradually increases with packing fraction when $\psi > 1$. Note that even at the highest compression state considered in our simulations, the particle interpenetration remains much smaller than the average microgel crosslink distance. We note that we do not find any significant difference in radial penetration between microgels with normal and uniform crosslink distributions.

The dependence of the average microgel volume on $\psi$ varies between the volumetric and solvency methods. Figure 5.2e-j illustrates how state of the suspension changes when the solvency is varied. The figure shows that the suspension rapidly rearranges itself near the critical point ($a \approx 29.5$) where the gelation occurs. The gelation prevents relative motion microgel particles in the suspension. This is in contrast to the low packing state of the volumetric method (Figure 5.2d), where microgel particles can rearrange easily with time. As shown in Figure 5.3c indeed with the solvency method the average particle volume is nearly constant when $\psi > 1$ up to the largest $\psi$ we tested and decreases with decreasing $\psi$ for $\psi < 1$. Thus, when the swollen microgels fill $V_{box}$ resulting in $\psi > 1$, the particle volume does not change with solvency and remains equal to approximately $V_{box}/\kappa$. However, in bad solvent the microgels deswell and the suspension undergoes gelation, which in turn decreases the volume occupied by microgels below $V_{box}/\kappa$. Note that the normalized volume data for microgels with uniform and normal crosslink distributions exhibit similar behavior. Changing the box size at which the

solvency is varied shifts the volume curve along the vertical axis, as shown by suspension IV in Figure 5.3c.

To further analyze the microgel volume change in the suspension for the solvency method, we compare the volume data for suspension I to the volume of a single microgel particle (not in suspension) that is equilibrated under identical solvent conditions. The single microgel data $V_{single}$ is shown in Figure 5.3a by the dotted line. Given that for a single microgel particle the volume changes roughly 10-fold between the collapsed and swollen states, in bad solvent we expect $V/V_{eq}$ to approach $\sim$0.1. Indeed, the line for single particle volume $V_{single}$ shows this but interestingly this is not the case for microgels in the suspension. We find that at bad solvent, corresponding to $\psi < 1$, microgels in the suspension have greater volumes than $V_{single}$. Thus, at bad solvent conditions, microgels in the suspension remain more swollen. This can be attributed to the interpenetration of neighboring microgel particles. As shown in Figure 5.3d, for the solvency method interpenetration increases once gelation occurs, which for suspension I happens at $\psi \lesssim 1$.

At bad solvent, gel-solvent interactions are unfavorable which promotes interpenetration of neighboring microgels which is further enhanced by microgel gelation. As shown by suspension IV in Figure 5.3d when the solvency is varied at a lower $\psi$ the critical point can be shifted to $\psi < 1$ which causes the interpenetration to significantly decrease for $\psi_c < \psi < 1$. Here, $\psi_c$ is the generalized packing fraction at the critical point. In this case, microgel interpenetration is reduced by entropic forces that detach microgels and fluidize the suspension. Gelation of suspensions in $\psi < \psi_c$ results in interpenetration that increases as the solvency worsens and $\psi$ decreases. We find that for gelated

suspensions, the interpenetration depth is $\sim 10-20\%$ of the crosslink distance, which is very similar to interpenetration depth of the volumetric method in highly compressed state.

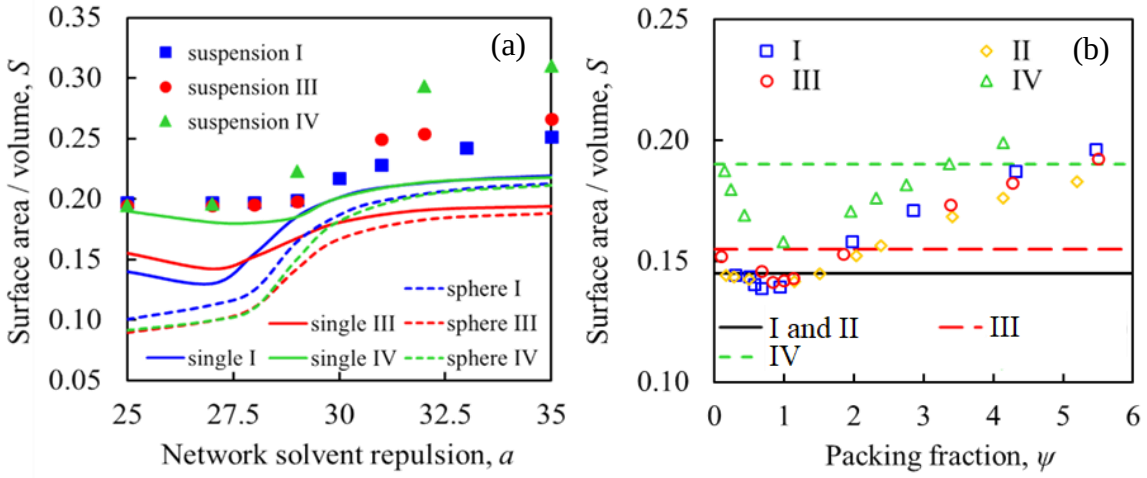


**Figure 5.4**. (a) Surface area to volume ratio $S$ of different microgel suspensions for the solvency method. Markers show $S$ for microgel particles in the suspension. The solid lines show the $S$ ratios for a single microgel particle that is freely equilibrated (i.e. not in suspension) in solvent. Dotted lines show $S$ ratios of spherical particles with same volume as the single microgel particles, represented by the solid lines. (b) $S$ of different microgel suspensions for the volumetric method. The solid black line shows $S$ for a single microgel particle with a normal crosslink distribution. The red and green dotted lines show $S$ for networks III and IV respectively.

The crosslink distribution does have a noticeable effect on the deformation of microgel particles in the suspension. Figure 5.4a illustrates how the ratio of surface area to microgel volume $S$ changes with solvency in the suspension I, III, and IV. The markers in the plots show $S$ for microgels in the suspension, whereas the solid lines show $S$ for a standalone microgel particle. The dotted lines show $S$ of a sphere with volume identical to the average microgel volume in the suspension.

Figure 5.4a shows that $S$ in the suspension increases when the solvency decreases in the range $30 < a < 35$. This increase of $S$ occurs due to increased deformation of microgels, which makes the particles more aspherical. The increase in $S$ is more pronounced for suspensions of microgels with normal crosslink distributions.

The largest increase in $S$ occurs for suspension IV which is comprised of microgels with a wider chain length distribution. This indicates that the chain length distribution can significantly affect the deformation of the particle. In good solvent, when $\psi$ is large, all suspension data converges to nearly the same $S$, indicating that all particles assume similar shapes. For standalone microgels, the transition to good solvent increases $S$. This occurs due to the expansion of polymer chains at the gel-solvent interface, which increase the effective surface area. Microgels in suspension in good solvent are highly compressed, and thus exterior polymer chains cannot extend. As a result, no increase in $S$ takes place for suspension in good solvent.

For spheres with radius $R$ the surface volume ratio is $S = 3/R$. As the sphere size decreases due to the solvency change from good to bad, $S$ increases monotonically. In bad solvent the dotted and solid lines converge as the standalone microgels collapse and assume spherical shapes. For microgels I and IV at bad solvent, the single particle data converges to the same $S$ since these microgels have nearly identical molecular weights (Table 1).

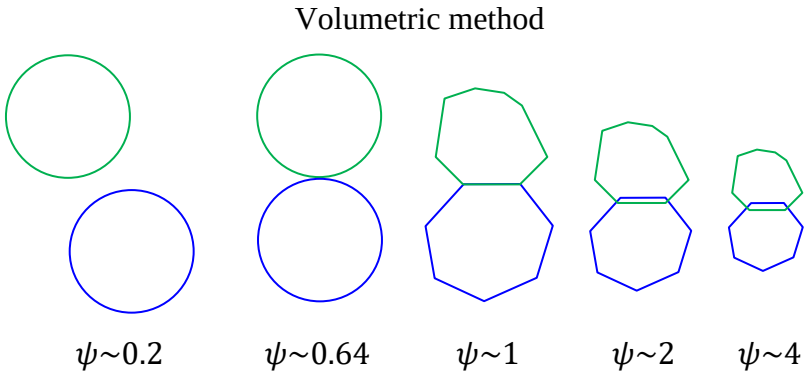


**Figure 5.5**. Schematic showing typical microgel shape changes throughout the volumetric method. At low $\psi$ the microgels are nearly spherical with little neighbor contact. As $\psi$ increases the microgels begin to make contact. Near $\psi \approx 1$, the microgel shape begin to change as neighbor contacts deform each particle. As $\psi$ increases further the particles shrink to accommodate the changes in volume. During this process microgels also begin to interpenetrate their neighbors. Microgel interpenetration is on the order of the crosslink distance.

Microgel III, which has a higher molecular weight and is larger in size converges to a lower $S$ than other microgels. For microgels in the suspension, $S$ increases, as microgels deform to maintain contact with neighboring particles and to minimize interactions with the solvent.

Figure 5.4b shows how $S$ changes for suspensions I-IV compressed by the volumetric method. For all the suspensions, we find a minimum of $S$ near $\psi = 1$. At low generalized packing fractions $\psi \approx 0.2$, when the particles are relatively dilute, $S$ matches the values for a standalone microgels, as shown by the dotted lines. In the range $0.4 < \psi < 1$, the surface area to volume ratio $S$ decreases with increasing $\psi$, for microgels with a normal crosslink distribution, as microgels begin to shrink, and polymer chains at the gel surface retract, reducing the overall surface area. The corresponding decrease in $S$ for microgels with a uniform crosslink distribution is smaller. This can be attributed to the fact that these networks are more homogeneous and do not have long dangling chains at the microgel surface. Near $\psi \approx 1$ the particles begin to lose their spherical shape. Figure 5.5 shows a schematic of the shape changes of two microgel particles in the suspension for the volumetric method. When $\psi > 1$, neighbor-neighbor contacts are relatively independent from $\psi$. Thus, increases in $\psi$ beyond 1 shrink the microgel volume and increase $S$, as shown in Figure 5.5 for suspension I. The figure shows that for $\psi > 1$ the microgels shrink with some minimal interpenetration while maintaining a nearly constant shape.

## 5.4 Suspension Mechanics

Figure 5.6a-b shows the bulk moduli for suspensions of microgel particles with uniform and normal crosslink distributions as a function of $\psi$, for both the volumetric and solvency methods. The data obtained using the volumetric method follows a linear trend with $\psi$, which agrees with the experimental results [59]. We find that increases in the microgel crosslink density make the suspensions mechanically stiffer. This trend become more dominant as $\psi$ increases. We find that for microgels I and III with similar crosslinking densities, the suspensions exhibit nearly identical mechanical response. This suggests that the crosslink distribution within microgel particles does not significantly affect the mechanical properties of the suspension. Figure 5.6b shows that the bulk modulus for the solvency method remains relatively constant as $\psi$ is varied. Figure 5.2e-j shows that as $\psi$ decreases below 1, the suspension experiences gelation. The suspension internal structure

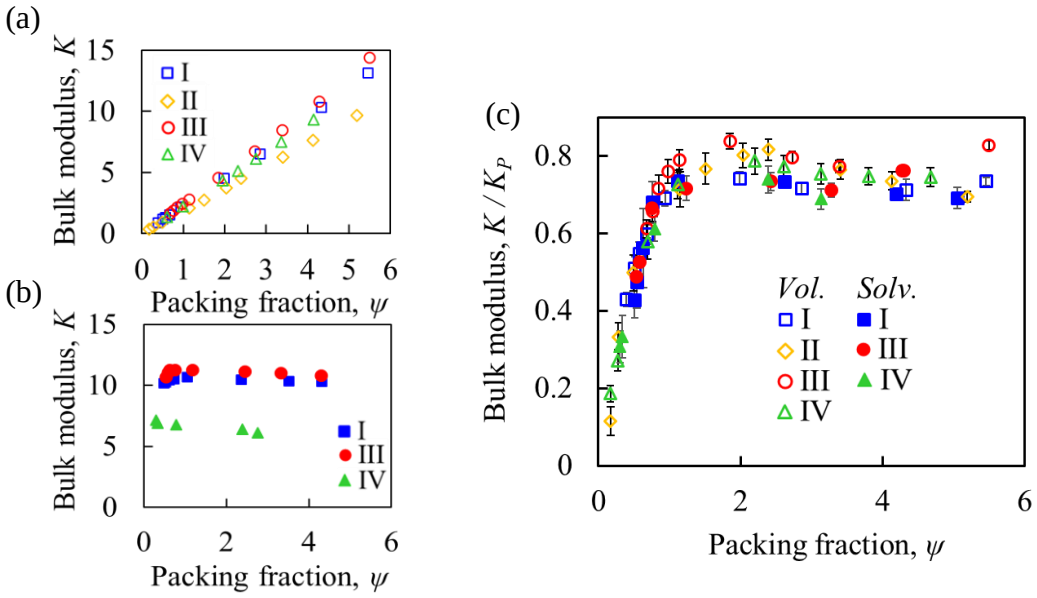


**Figure 5.6**. Bulk modulus data for suspensions consisting of microgel particles with uniform (I and II) and normal (III and IV) crosslink distributions for both volumetric (a) and solvency (b) methods. (c) Normalization by single particle bulk modulus shows $K/K_P$ data remains relatively constant for $\psi > 1$, indicating suspension mechanics are dictated by modulus of constituent particles.

in the kinetically arrested gelated state is drastically different from that of the compressed suspension in good solvent, but remarkably similar values of $K$ are obtained. This indicates that the formation of a colloidal gel at low $\psi$ stiffens the suspension. This behavior occurs irrespective of what generalized packing fraction the solvency is varied at and whether the uniform or normal crosslink distribution is used. This again signifies that crosslink distribution alone does not significantly impact the mechanics of the suspension.

As shown in Figure 5.6c, despite the large differences in $K$ between the volumetric and solvency methods at low $\psi$, normalizing $K$ by $K_P$, the bulk modulus of a standalone microgel particle at the specified $\psi$ and $a$ [59, 120], the bulk modulus data collapses onto a master curve. This was experimentally observed for volumetric compression of microgel suspensions with different crosslink concentrations. [59]. Our simulations indicate that the same scaling can be applied when $\psi$ is varied by changes in the solvency. Furthermore, based on results for suspensions III and IV we conclude that the width of the chain length distribution does not play a significant role.

Recall that for the volumetric method, at low $\psi$ the suspension is in a dilute state (Figure 5.2d) with $K < K_P$; hence the suspension is more compressible than a single microgel particle. As $\psi$ increases up to roughly 1 the initially dilute microgel suspension densifies and $K$ approaches $K_P$ [58, 61, 132]. For $\psi > 1$, the microgel particles completely fill the suspension volume. In this case, $K \sim K_P$ and the normalized bulk modulus then remains relatively constant.

For the solvency method at low $\psi$ a colloidal microgel network forms (Figure 5.2h-j). As the solvency shifts towards good solvent the normalized bulk modulus increases. This does not occur due to the stiffening of the suspension (Figure 5.6b), but rather due to

the softening of standalone microgels with increasing $\psi$. Remarkably the solvency method yields the same trend as the volumetric method, indicating the ratio $K/K_P$ is a universal measure of the mechanics of microgel suspensions. The result is insensitive to the type of the crosslink distribution within the microgel particles.

Figure 5.7 below shows how the rheological response for suspension I varies with frequency for both the volumetric and solvency methods. The viscoelastic behavior of each suspension is determined by the packing fraction and the particle-particle interactions [125]. Since the particle-particle repulsion for the volumetric data (empty symbols) is constant ($a = 25$) the critical parameter in this case is $\psi$. Meanwhile, for the solvency method (filled symbols) both $\psi$ and $a$ can impact the rheology. Once normalized by the crossover frequency $\omega_{crossover}$ and crossover modulus $G'_{crossover}$ all of our data collapses onto two master curves, for $G'$ and $G''$. Here $G'$ and $G''$ are the storage and loss moduli of the suspension. This is in agreement with previous results for soft matter suspensions [125].

Figure 5.7 shows that at low $\omega$ in both the volumetric and solvency methods the suspensions behave as an elastic solid and $G' > G''$. As $\omega$ increases damping increases and a critical point is passed ($\omega_{crossover}$) where $G' = G''$. Past this point the viscosity of the fluid begins to dominate the behavior of the suspension and $G'' > G'$. In this regime the suspension begins to flow.

The variation in $\omega_{crossover}$ and $G'_{crossover}$ with $\psi$ is shown in the plot in Figure 5.8. Given that the relaxation time $\tau_{relax} \approx 1/\omega_{crossover}$ it is clear that for the volumetric method $\tau_{relax}$ begins to significantly increase as the dilute regime is approached, as expected [133]. The increase in $\tau_{relax}$ at low $\psi$ for the solvency method is not as pronounced. Moreover, past the critical point $\tau_{relax}$ does not increase with further decreases in $\psi$. This happens because in the bad solvent regime (low $\psi$) the suspension forms a colloidal microgel network. Due to gelation the crossover modulus for the solvency method is approximately an order of magnitude higher than the crossover modulus for the volumetric method in low $\psi$ states. As shown by the dotted yellow line in Figure 5.8 at higher $\psi$, $G'_{crossover}$ increases only up to $\psi \approx 1$. The change in $G'_{crossover}$ across the critical point is abrupt due to gelation. For $\psi > 1$ average microgel volume remains fixed to $V = V_{box}/\kappa$. As shown in Figure 5.3d for suspension I (solvency method) microgel-

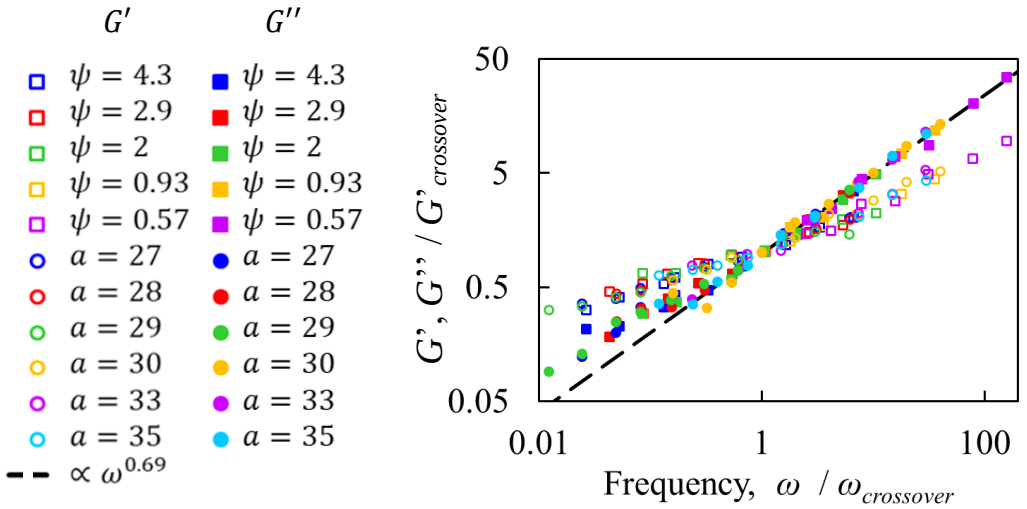


**Figure 5.7**. Master curve data showing frequency sweeps of the scaled storage and loss modulus for both the volumetric and solvency methods. Here we normalize the loss and storage moduli by the storage modulus at the crossover point, i.e. when $G' = G''$. Similarly, the frequency is normalized by the crossover frequency $\omega_{crossover}$. Doing this the plot shows that all our data collapses onto two master curves. At high frequencies $G''$ scales as $\propto \omega^{0.69}$, as shown by the black dotted line.

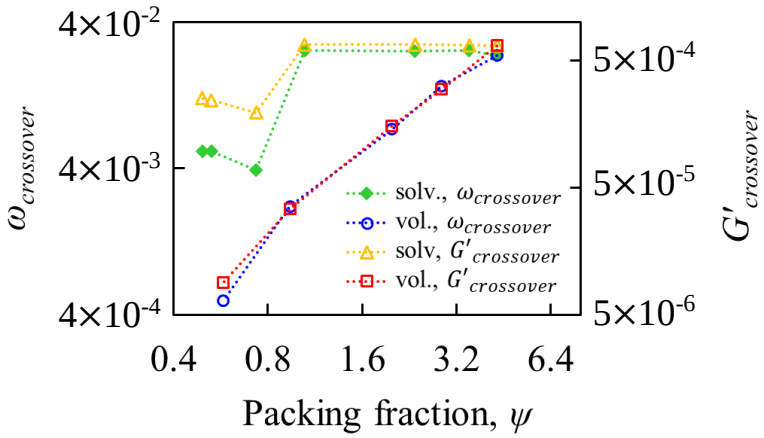


**Figure 5.8**. Plot showing how crossover frequency and storage modulus vary with packing fraction for both the volumetric and solvency methods. For the solvency method at $\psi > 1$ both $\omega_{crossover}$ and $G'_{crossover}$ become constant. This occurs because for $\psi > 1$ the volume of each microgel in the suspension is restricted to $V \approx V_{box}/\kappa$, since $V_{box}$ is constant for the solvency method. For the volumetric method both $\omega_{crossover}$ and $G'_{crossover}$ increase with $\psi$, indicating compression enables the suspensions to remain solid-like at higher frequencies. In the range $0.5 \lesssim \psi \lesssim 4$ $\omega_{crossover}$ and $G'_{crossover}$ for the solvency method are larger than the corresponding values for the volumetric method. This occurs due to the increase in $a$ for the solvency method which makes microgel-microgel interactions more favorable and leads to increased interpenetration between microgels. For the solvency method at the critical point near $\psi \approx 1$, gelation causes structural rearrangements in the suspension leading to a drop in $\omega_{crossover}$ and $G'_{crossover}$.

microgel interpenetration also remains approximately constant, $\sim 0.18\delta_{X-link}$. This behavior is significantly different than what is observed for the volumetric method where the crossover modulus monotonically increases with $\psi$. The monotonic increase indicates that compression allows the suspension to maintain its elastic character at higher $\omega$.

As shown by the black dotted line in Figure 5.7, at high packing fractions the loss modulus data $G''$ exhibits power law behavior, which is common for critical gels [133]. The power-law exponent reflects the internal relaxation modes of the microgel particles and is found to be ~0.69, which is similar to the ¾ exponent noted by Morse for loosely entangled semi-flexible polymer chains in good solvent [134]. For lower $\omega$ a deviation

from power law behavior occurs, as expected [125]. We are limited in the ability to probe the mechanics at low frequencies due to computational limitations, which arise from the large oscillation periods, which are in excess of 10,000 DPD time units. To obtain accurate frequency measurements several periods are also necessary which further increases the computational costs.

## 5.5 Summary

We examine the behavior of neutral microgel suspensions under different generalized packing fractions $\psi$. The suspensions are comprised of identical microgel particles with either uniform or normal crosslink distributions. We test two different methods for varying $\psi = \kappa V_{eq}/V_{box}$, volumetric and solvency methods. In the volumetric method, $\psi$ is varied by isotopically deforming the computational box to alter $V_{box}$. For the solvency method, $V_{box}$ is kept constant, whereas the interaction of gel with solvent $a$ is varied to alter $V_{eq}$.

Our results show that with the volumetric method at $\psi$ that is below close packing, the suspension is in a colloidal fluid state where the volume of microgel particles approaches the volume of a standalone microgel in good solvent. At high $\psi$, the average microgel volume scales as $V \sim \psi^{-1}$, indicating the particles prefer shrinking over interpenetration. For the volumetric method, interpenetration increases when $\psi$ increases above 1. The maximum radial interpenetration is found about $20\%$ of the average crosslink distance. This indicates that interpenetration is likely limited by the mesh size of the microgel network. For the solvency method, we show that the interpenetration can be non-zero for $\psi < 1$. When the volume of suspension is such that gelation occurs at $\psi < 1$,

interpenetration attains zero values between $\psi = 1$ and the gelation point $\psi_c$. Due to interpenetration of neighboring microgels in bad solvent, microgel volumes in suspension are greater than the volume of a standalone microgel at the same solvent conditions. The maximum radial penetration with the solvency method is found about 23% of the average crosslink distance.

Analysis of suspension microgels for the solvency method reveals that in bad solvent microgels with normal crosslink distributions attain higher surface to volume ratios than microgels with uniform crosslink distributions, which indicates that microgels with normal crosslink distributions are more deformable. For the volumetric method as $\psi$ decreases and the microgel volume increases the surface area to volume ratio increases due to the expansion of polymer chains at the gel-solvent interface. The increases in the surface to volume ratio is more significant for microgel networks with normal crosslink distributions. Low functionality crosslinking sites near the gel-solvent interface can create long polymer chains which significantly increase the surface area of the microgel. For the volumetric method at high $\psi$, we show that as the microgels shrink the surface to volume ratio steadily increases.

Our bulk modulus data indicates that in the tested suspensions the ratio of the microgel suspension bulk modulus to the single microgel bulk modulus, $K/K_P$, is a universal parameter that characterizes the mechanical behavior of the suspension. This scaling holds irrespective of the fact that at $\psi < 1$ the suspension structure and bulk modulus $K$ differs significantly between the volumetric and solvency methods. The differences in $K$ for the two methods are attributed to the gelation which occurs when the

solvency is varied below the critical point. Upon gelation the microgel particles form a colloidal network which stiffens the suspension.

Finally, our rheological results show that for both the volumetric and solvency methods all storage and loss moduli data can be scaled onto two master curves. This scaling agrees well with previous results for soft suspensions [125]. By tracking how the crossover frequency and storage modulus vary with $\psi$ we illustrate structural differences between microgel suspensions. At low $\psi$ suspensions in the solvency method have higher $\omega_{crossover}$ and $G'_{crossover}$ values indicating that due to gelation the suspension can maintain its elastic behavior at higher frequencies.

# CHAPTER 6. SELF ORGANIZING STRUCTURES

## 6.1 Introduction

The ability to create complex 3D microstructures has the potential to significantly improve existing drug therapies [39, 135, 136], tissue scaffolding methods [20, 137, 138], and *in vivo* bio-tracking approaches [30, 139, 140]. In addition to this, the capability to reversibly switch from a 2D to 3D geometry, in response to environmental stimuli can be leveraged to create novel micro-sensing devices [50]. Recent work has shown that proteins from *Bombyx mori* can be arranged in hydrophobic/hydrophilic blocks, forming supermolecular hydrogel structures [141-143], which can reversibly swell/deswell in response to changes in the pH [142]. These materials are ideal for *in vivo* applications because they are biocompatible and biodegrable. In addition, spider silk is remarkably strong and extensible material which is also stable under harsh environmental conditions [142, 143].

In this chapter we utilize computational modeling to study how the swelling induced, shape dependent, bi-axial stress distributions in silk-on-silk composites (polystyrene/silk-ionomer/beta-sheet) allows 2D sheets to transform into complex 3D structures like rings and tubules. The lateral dimensions of these microsheets range from 20-100 micrometers. Meanwhile, the thickness of the composite structure is varied in the range of 100-700 nm. The active silk-ionomer layer is relatively soft (~11 MPa) and is sandwiched between the stiffer polystyrene (PS, ~1.8 GPa) and $\beta$-sheet (~8.6 GPa) layers. In order to facilitate the design of self-activated microstructures we use computational modeling to investigate how the initial 2D geometry affects the final equilibrated 3D shape of the structure.

Doing this we examine how stresses develop in microstructures with different geometries and thickness ratios, underscoring the corresponding impact on the final 3D structure.

## 6.2 Computational Setup

Computationally the lattice spring model (LSM), a modeling technique for simulation of deformable solids [144-146], was utilized to simulate the self-rolling behavior of the silk-on-silk microsheets. In the simulation, the biopolymeric sheet was constructed using a regular network of interconnected beads placed on a simple cubic lattice. Each bead in the network was connected by stretching springs (bonds) to its closest and next-closest neighbors. The bulk elastic properties of the polymer structures were set by adjusting the stiffness of lattice springs to match the mechanics of polymer layers [147]. Thus, the network consisted of three different regions, corresponding to the PS, silk ionomer, and $\beta$-sheets layers. The thickness ratios and lateral aspect ratios of the networks were set to match the experimental morphology. In particular, the shaped silk sheets were created from initially rectangular network by removing beads outside the region of interest. The swelling response of the active silk ionomers layer was simulated by change the equilibrium length of the bonds in the "active" network region [40, 88] in which the length of the bonds gradually increased by 1% steps until the silk ionomer swelling ratio matched the experimental swelling ratio obtained from optical micrographs ($\sim$160%). To include the effect of thermal fluctuations on the bending, the dissipative particle dynamics thermostat was employed [70]. A viscous damping was imposed to mimic the effect of solvent viscosity. The dissipative force was set proportional to the bead velocity with a proportionally constant equal to 0.2.

To prevent interpenetration between LSM beads we discretize each microsheet into smaller rectangular regions. For each particle in a given region we apply a pairwise linear force potential. This potential is applied only between particle pairs which are not members of the same region or members of an adjacent region. This allows the microsheet to maintain the mechanical properties set forth by the network bond stiffness, while also preventing interpenetration during folding.

## 6.3 Deformation and Stress Analysis

In the analysis below we examine how the polystyrene layer thickness affects the folding behavior of the composite structure. In addition, we study how different initial geometries affect the final equilibrated shape. The two geometries we focus on are rhomboids and rectangles. For the rectangular microsheets we examine geometries with length to width ($L/W$) aspect ratios of 1, 2, and 8. For the rhomboid microsheets we look at rhomboids with minor angles of $15°$ and $30°$ degrees.

In the computational model, the thicknesses of the active silk ionomer layer and passive $\beta$-sheet layer were kept constant. Variations in the thickness ratio (PS layer / active silk ionomers layer) were obtained by changing the PS layer thickness. When the thickness ratio was 1.6 the simulations did not reveal any significant deformation of the composite structure (Figure 6.1a-b). This occurs because at this thickness the PS layer has approximately the same effective stiffness as the $\beta$-sheet layer. As a result, no deformation occurs even when the simulation time is extended (Figure 6.1c-d). In contrast, composites with a thinner PS layer and a decreased thickness ratio (~0.4) deform initially at the corners (Figure 6.1e-f) and eventually roll into a 3D microtube (Figure 6.1g-h). The computational

results for different polystyrene layer thicknesses are in good agreement with experimental findings [18].

As shown in Figure 6.2 a notable change in the self-rolling behavior can be observed when the aspect ratio of the composite sheet is varied. For high aspect ratios ($L/W = 8$, Figure 6.2a-d) the structure does bend, but it cannot roll into a tube. This behavior is also observed in experimental testing of spider-silk composites with $L/W = 8$ [18]. When the aspect ratio is reduced to $L/W = 1$ the composite sheets fold into cylindrical microtubules with a predetermined radius, as shown in Figure 6.2e-h. Our simulations show that for an aspect ratio of one ($L/W = 1$) isotropic swelling causes the structure to deform symmetrically, as shown in Figure 6.2f. The structure in Figure 6.2f is metastable, however. As time progresses small thermal fluctuations perturb the structure causing one of the corners to break the symmetry in Figure 6.2f and start locally rolling. This in turn produces a similar response in the other three corners, which ultimately leads the microsheet to bend. Once this is done deformation in adjacent corners can cause the

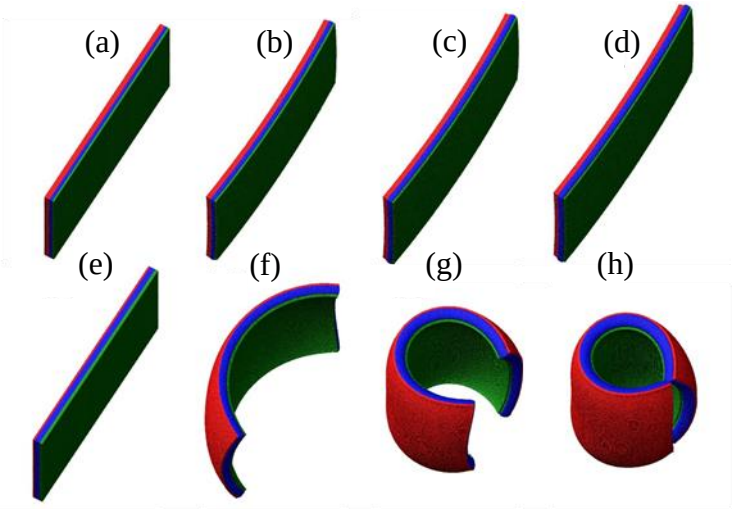


**Figure 6.1**. Activation of microsheets with an aspect ratio of 2 and thickness ratios of 1.6 (a-d) and 0.4 (e-h). For larger thickness ratios almost, no deformation is observed (a-d). Decreasing the thickness ratio allows the composite microsheet to roll into a microtube (e-h).

entire edge to roll over on itself. This is shown in Figure 6.2g where it can be seen that one of the sheet edges has started to roll, initiating microtube formation. In Figure 6.2g it can also be seen that the other two corners are independently trying to roll over. Ultimately, as rolling progresses these corners straighten out and conform to the cylindrical geometry of the microtube.

In Figure 6.3a-d the snapshots demonstrate that for rhomboid sheets with a shallow angle (15°), bending is initiated at the sharp corners. Deformation near the opposing wide-angle corners is minimal. As swelling proceeds, the corners continue to bend until the two minor angle corners meet each other as shown in Figure 6.3d. Since the rhomboid geometry is asymmetrical the deformation of the corners produces helical structures (Figure 6.3c-d) identical to what is seen in experiments [17, 18]. For small minor angles (15°) the pitch of the helix is decreased and as a result the structure in Figure 6.3d is ring-like. As shown in Figure 6.3e-h by increasing the minor angle from 15° to 30° the pitch of the rhomboid

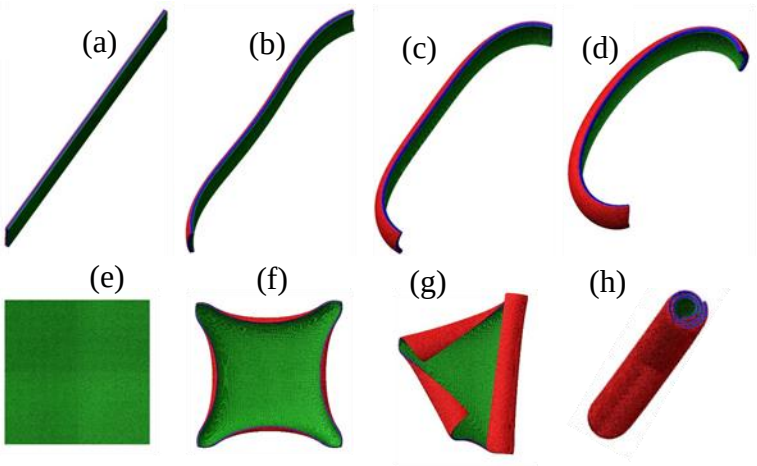


**Figure 6.2**. Simulation snapshots showing self-rolling of silk microsheets as a function of the aspect ratio (thickness ratio of PS layer/active layer: 1.5). Microsheet with aspect ratio of 8 is shown in images (a-d). Meanwhile images (e-h) show a microsheet with an aspect ratio of 1.

structure can be increased (Figure 6.3h), which agrees well with experimental observations [17, 18].

For rectangular sheets with an aspect ratio of 2 ($L/W = 2$, Figure 6.3i), if the microsheet is initially completely flat self-rolling occurs along the short edge in our simulations. If the sheet is initially bent slightly, as shown in Figure 6.3m swelling of the silk ionomer layer leads to self-rolling along the long edges. These results show that for rectangular sheets, depending on the initial microsheet deformation, two self-folding directions are possible. Experimentally, bending along the long edge is observed more often because the long edge area moment of inertia is smaller than the short edge area moment of inertia. Due to this, small perturbations in the fluid can more easily deform and bend the initial microsheet structure, which facilitates rolling along the long edge.

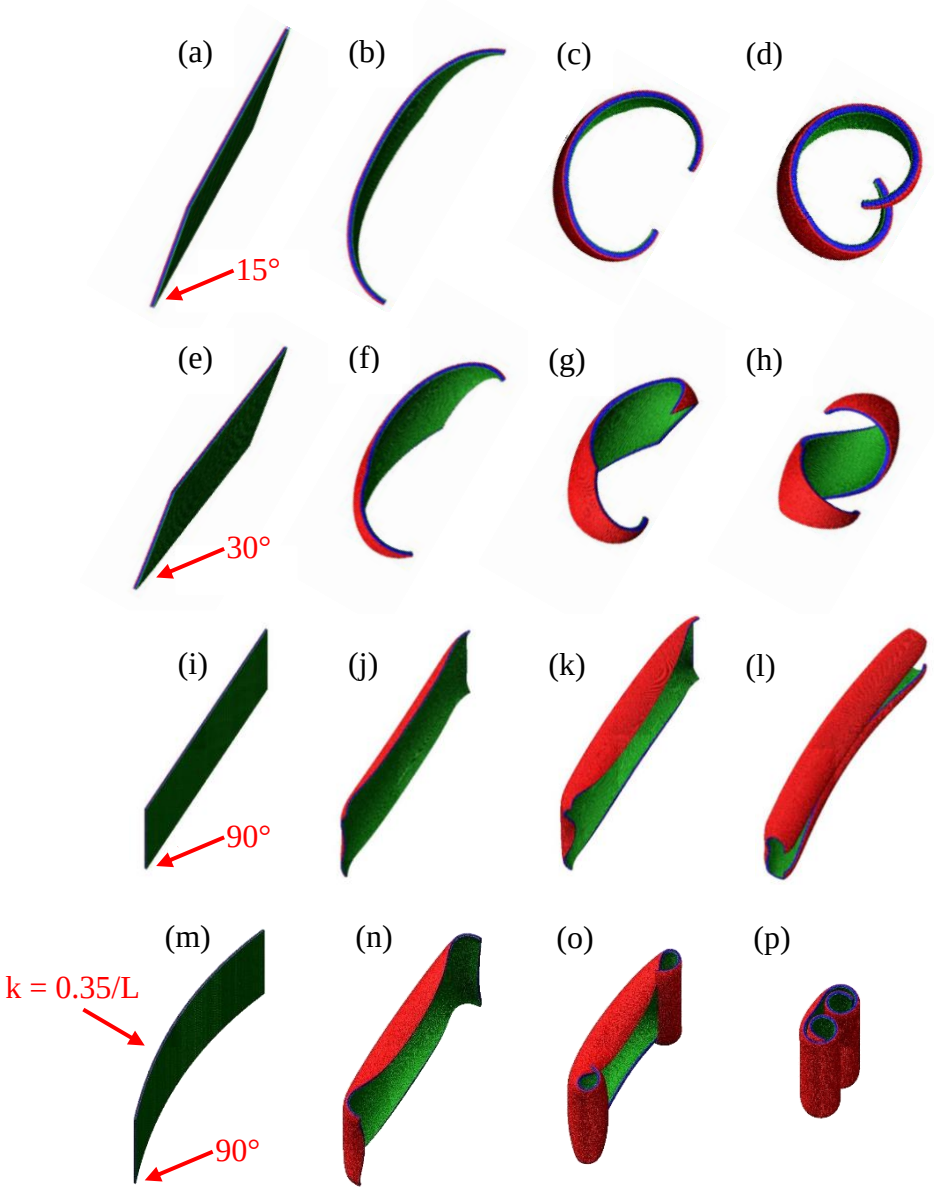


**Figure 6.3**. Simulated self-folding behavior of silk-on-silk microsheets. (a-d) Snapshots for rhomboid geometries with 15° minor angle. (e-h) Snapshots for rhomboid geometries with 30° minor angles. (i-l) Simulation renderings showing folding in an initially flat rectangular sheet with an aspect ratio of 2, $L/W = 2$. (m-p) Images showing folding in an initially bent rectangular sheet ($L/W = 2$) with curvature $k = 0.35L$.

We utilize our LSM model to confirm that self-rolling of silk-on-silk microsheets can indeed be ascribed to the mismatch in interlayer stresses, which occurs due to non-uniform swelling within the composite structure. In particular, we use the LSM model to examine how stresses are generated throughout the microsheet once the silk ionomer layer is swollen [145]. For the stress analysis the three geometries which we examine are rectangular sheets with aspect ratios of 1, 2, and 8 and 30° rhomboids. In these cases, we examine the stress field in each layer (PS, silk ionomer, and $\beta$-sheet) individually. In our analysis negative values of stress correspond to tension and positive values correspond to compression.

Swelling of the silk ionomer layer triggers a biaxial expansion field within the microsheet which exerts stresses on both the PS and $\beta$-sheet layers. The PS and $\beta$-sheet both stretch as they resist the deformation which the silk ionomer layer imposes. The silk

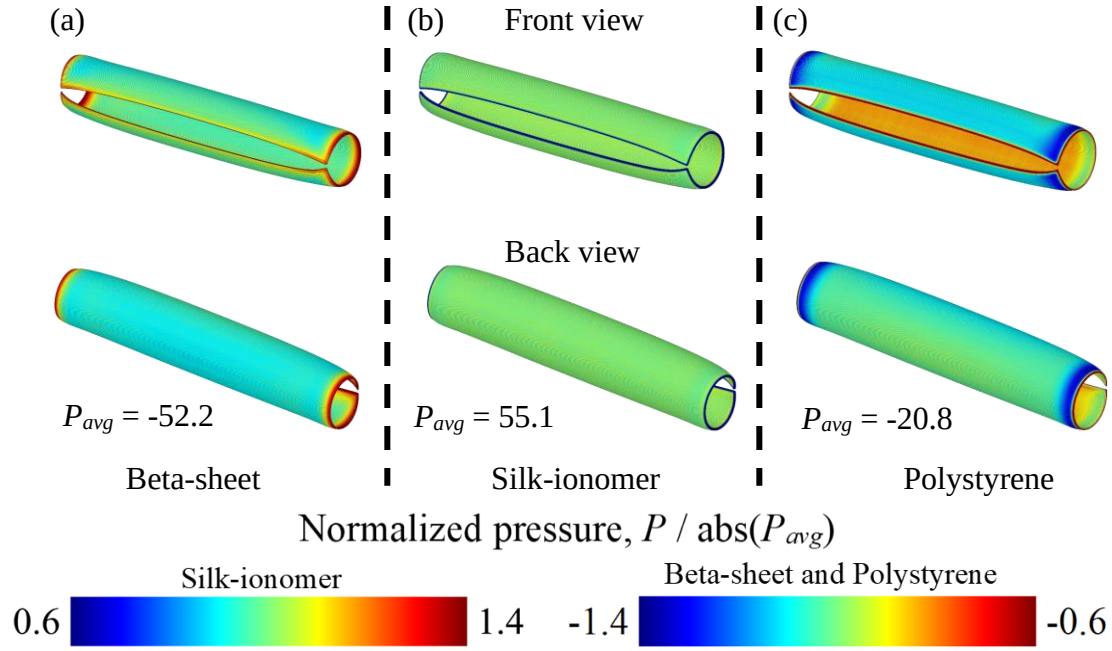


**Figure 6.4**. Stress map obtained from LSM model for individual layer within a composite silk microsheet an aspect ratio of 2. Top row indicated front view and the bottom row is the back view for each panel for the (a) $\beta$-sheet (b) silk ionomer layer and (c) PS layer.

ionomer layer meanwhile is compressed on both sides, as it can never reach its fully expanded equilibrium state. Thus, although the silk ionomer layer increases in volume it remains compressed throughout the entire swelling process (Figures 6.4b, 6.6b, and 6.8b). In contrast, both the polystyrene and $\beta$-sheet layers remain stretched (Figures 6.4a, 6.4c, 6.6a , 6.6c, 6.8a, 6.8c). The deciding factor in determining which side the structure rolls on is the stiffness of the passive (PS and $\beta$-sheet) layers. We can think of each layer as a spring, $F = kx$, where $k$ corresponds to the bulk moduli of each layer. As the silk ionomer swells it enforces a displacement ($x$) on both the PS and $\beta$-sheet, which in turn, exert a constraining force. Rolling occurs on the side for which the constraining force is larger. Since for the same thickness the force is governed by the bulk modulus (and displacement is the same for both layers) the structure will always prefer to fold on the stiffer side. The softer side will more easily (less force required) accommodate the displacements imposed

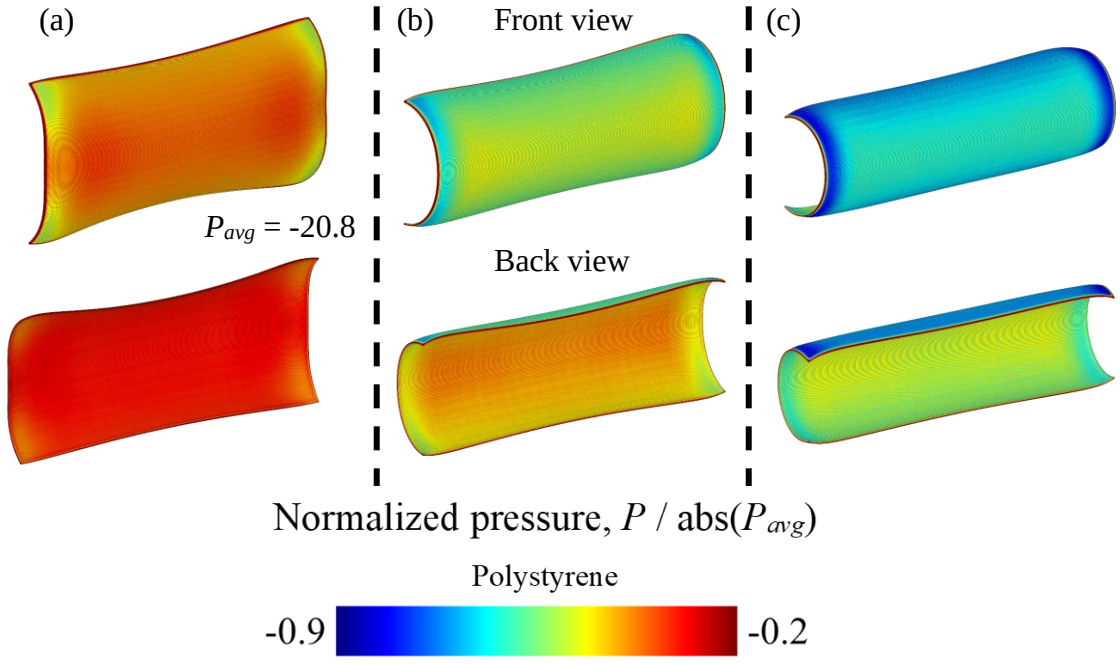


**Figure 6.5**. (a-c) LSM simulation stress distribution maps throughout the rolling process within the PS layer of a spider silk microsheet composite with an aspect ratio of 2. Front views are shown in top row and back views are shown in the bottom row.

by the silk ionomer layer. If the PS and $\beta$-sheet layers are roughly the same thickness, rolling will always occur on the beta-sheet side, which is also seen in experiments. This is supported by results in Figures 6.4, 6.5, and 6.8 which show that $|P_{avg}|$ for the $\beta$-sheet layer is larger than $|P_{avg}|$ for the PS layer, confirming that the constraining effect of the $\beta$-sheet layer is larger.

The presence of tensile and compressive forces is reflected in Figure 6.4 by the average pressure $P_{avg}$ in each layer. For the polystyrene and $\beta$-sheet layers $P_{avg}$ is negative, indicating the layers are under tension. Meanwhile for the silk ionomer layer $|P_{avg}|$ is positive, which confirms that the active layer is under compression.

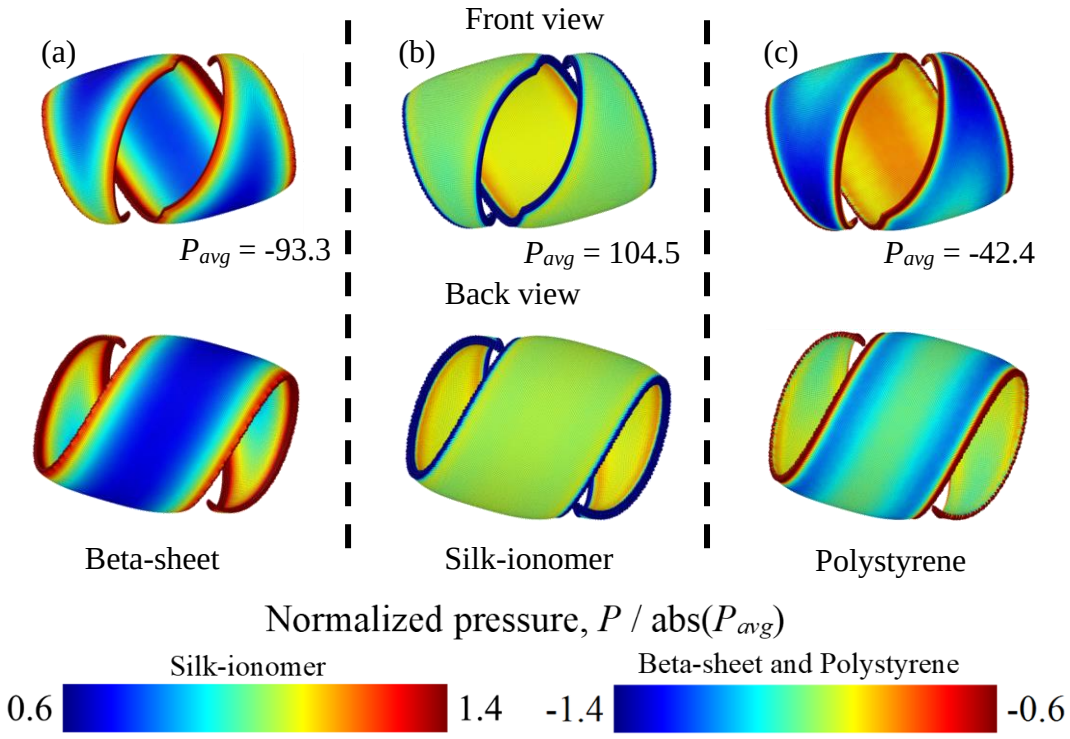


**Figure 6.6**. Stress map obtained from computational simulation for each individual layer within the sandwiched 30° parallelograms silk microsheet. a) $\beta$-sheet; b) silk ionomer layer; c) PS layer. Top row indicated front view and the bottom row is the back view for each panel.

As shown in the stress map of Figure 6.4c the stress concentration is higher along the shorter pair of edges. To understand why this occurs we examine how stresses develop in the PS layer (aspect ratio 2) with time, as shown Figure 6.5. When the silk ionomer layer is swollen, we observe higher tensional stresses in the corners (Figure 6.5a), which initiates bending. As the corners bend, they pull and deform the rest of the sheet. The deformation at the corners causes the moment of inertia along the longitudinal axis to decrease (Figure 6.5b). This transformation increases the bending moment and drives the deformation even further, helping the sheet roll into a tube (Figure 6.5c). It should be noted that the high

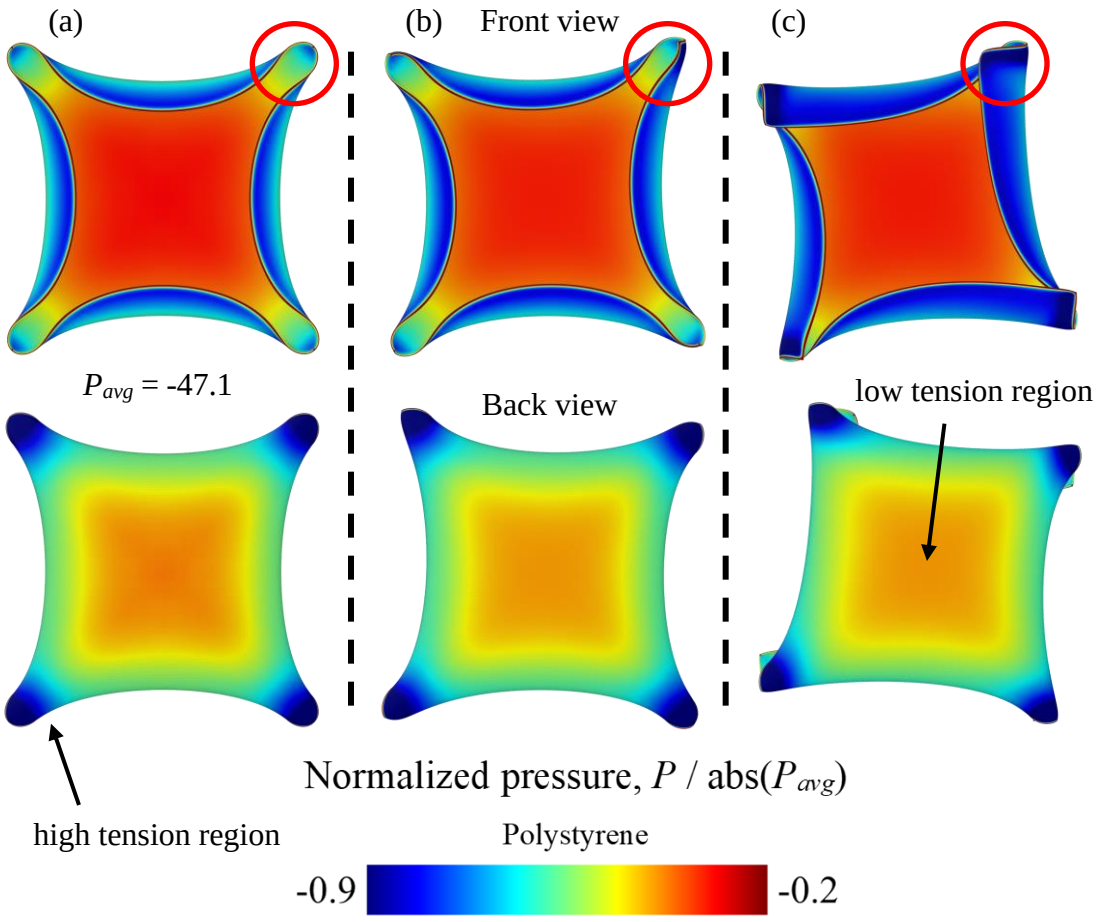


**Figure 6.7**. Color map of calculated stress within the PS layer as an example in the sandwiched silk microsheets with an aspect ratio of 1 over a time series (a-c) (from left to right). Front views as shown in top row and back views in the bottom row. Folding is initiated in the top right corner of the sheet (front view).

stress regions in the PS layer correspond to low stress regions in the $\beta$-sheet (Figure 6.4). This happens because $\beta$-sheet region is located below the neutral plane and the PS layer is above it. Therefore, any localized bending produces extra tension in the PS layer and extra compression in the $\beta$-sheet layer. However, since the $\beta$-sheet is strongly stretched by the silk ionomer layer, this localized compressive effect only serves to create areas of low tensional stress.

LSM simulations in Figures 6.6, 6.7 and 6.8 show that as the silk microsheet geometry is varied the stress distribution changes, altering the morphology of the activated composite structure. This illustrates how geometric changes to the initial 2D microsheet impact the final equilibrated 3D structure, after activation. For example, when the microsheet has a rhomboid geometry (Figure 6.6), stress concentrates in the minor angle corners. As stresses grow, the PS layer, which is above the neutral axis is put in tension.

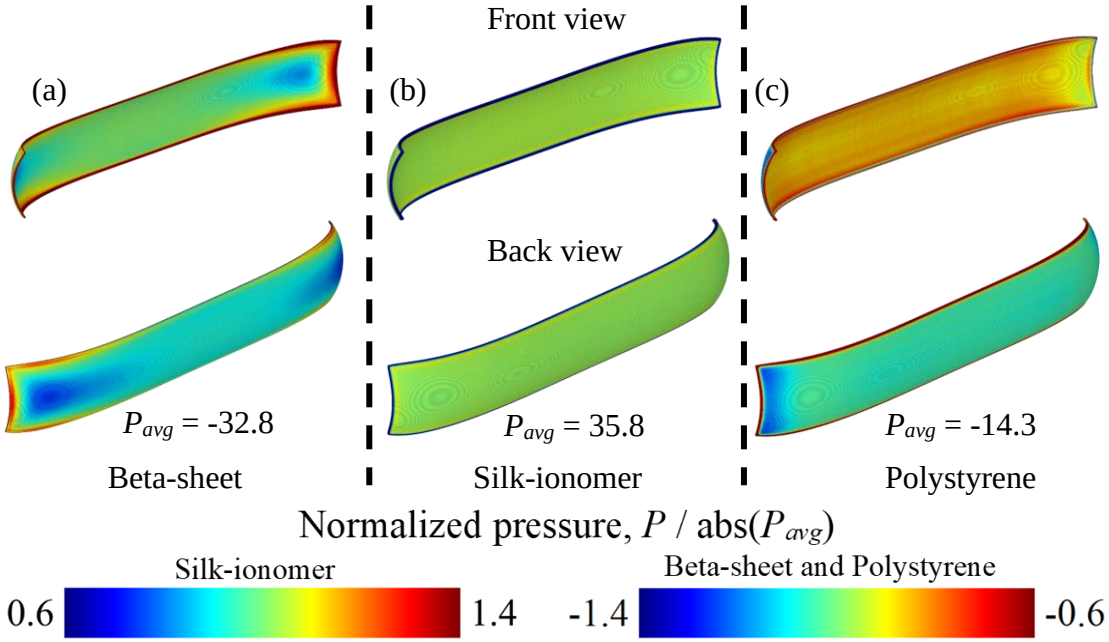


**Figure 6.8**. Stress map obtained from computational simulation for each individual layer within the sandwiched silk microsheet with an aspect ratio of 1:8. (a) $\beta$-sheet; (b) silk ionomer layer; (c) PS layer. Top row shows front view and the bottom row shows the back view for each panel.

Meanwhile, the $\beta$-sheet layer, which is below the neutral axis experiences compression locally. This effect leads to a decrease/increase in tensional stresses for the $\beta$-sheet/PS layer near the minor angle corners, producing localized bending. As the deformation progresses, the asymmetry of the structure causes the sheets to roll into helical structures (Figure 6.6).

For microsheets with an aspect ratio of 1 stress accumulation in the corners does again lead to bending, however due to the high symmetry, the structure is initially locked in a metastable state (Figures 6.2f and 6.7a). In this state each corner's deformation interferes with the deformation of the other 3 corners. With time however, random thermal fluctuations increase the stresses in one of the corners, which initiates rolling and pushes the structure out of the metastable state. Figure 6.7b-c shows how the structure deforms once the system is perturbed out of the metastable state. The path to the final cylindrical structure (Figure 6.2h) is not unique due to the random nature of the perturbations. This agrees well with prior experimental studies [148].

The deformation and pressure distribution for a sheet with an aspect ratio of 8 is also shown in Figure 6.8. Here we see than the folding occurs along the length of the structure. This occurs because the width of the sheet is very small. The stress concentrations in the corners merge right away and two high stress regions appear which dictate the deformation. Rolling along the longitudinal axis in this case however is not possible as observed in Figure 6.8c.

## 6.4 Comparison with Experiments

In order to analyze the deformation of the tri-layered structures we modified a thermomechanical model for bending in composite sections [149]. In doing this, we assumed that $\alpha T \approx \varepsilon$. Where $\alpha T$ is the thermal expansion and $\varepsilon$ is the experimental swelling ratio due to changes in the pH. The cross-sectional view of the composite network is shown in Figure 6.9. In this Figure, $2h_1$, $2h_2$, and $2h_3$ represent the thickness of the polystyrene, silk-ionomer, and $\beta$-sheet layers, respectively. Meanwhile, $h_{i,j}$represents the distance between the centroidal lines of the $i$ and $j$ layers. The final radius of curvature of the composite structure can be predicted by considering the mechanical and swelling stresses in each layer. Doing this the radius can be defined as:

$$r = \frac{E_1 I_1 + E_2 I_2 + E_3 I_3 + abs\left(\bar{y}\left(h_{12} E_1 A_1 - h_{23} A_3 E_3\right)\right) + h_{12} h_{23} A_3 E_3}{\left[h_{12} E_1 A_1 - h_{23} A_3 E_3\right] \bar{\varepsilon}} \quad (1)$$

Here $E_i$, $I_i$ and $A_i$ are the corresponding moduli of elasticity, area moments of inertia, and cross-sectional areas. The variables $\bar{y}$ and $\bar{\varepsilon}$ are given as:

$$\bar{y} = \frac{E_2 A_2 h_{12} + E_3 A_3 h_{13}}{E_1 A_1 + E_2 A_2 + E_3 A_3} \quad (2)$$

$$\bar{\varepsilon} = \frac{E_2 A_2 \varepsilon}{E_1 A_1 + E_2 A_2 + E_3 A_3} \quad (3)$$

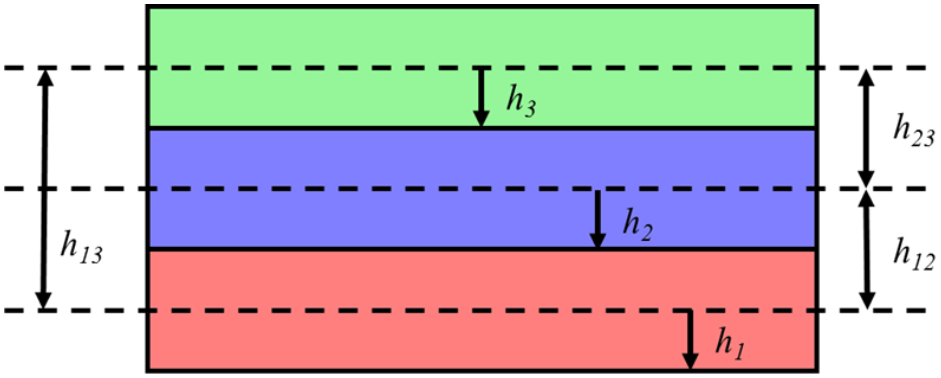


**Figure 6.9**. Cross-sectional view of composite structure. Green layer represents beta-sheet, blue layer represents the silk-ionomer, and red layer represents the polystyrene.

Using the scaling outlined in Equation 1-3, we can study how the final radius of curvature changes when we vary the $\beta$-sheet and silk ionomer layer thicknesses, and more importantly how these changes compare to experiments. Figure 6.10 shows how the radius of curvature changes as a function of PS thickness for five different $\beta$-sheet thicknesses. Here, the change in sign of the radius represents a switch in the folding direction. Negative values of the radius correspond to folding on the $\beta$-sheet side and positive values represent folding on the PS side. The dotted lines represent the PS thicknesses for which a switch in the folding direction occurs. From the figure it can be seen that as the $\beta$-sheet thickness is increased the dotted lines shift to the right, indicating the fact that as we increase the $\beta$-sheet thickness thicker PS layers are required to produce the switch in folding. When the $\beta$-sheet thickness is 34.4 nm the theory captures the experimental trend. The predicted $\beta$-sheet thickness also matches the experimental measurements for the $\beta$-sheet layer (33.5±0.9 nm).

Similar analysis can be applied as we vary the thickness of silk ionomer layer. A plot showing how the radius changes as a function of the PS thickness for different silk ionomer thicknesses is shown in Figure 6.11. From the figure it can be seen that as the silk ionomer layer thickness is increased, the dotted lines (indicating the switch in folding direction) again shift to the right. To fully understand this effect, we have to think of the

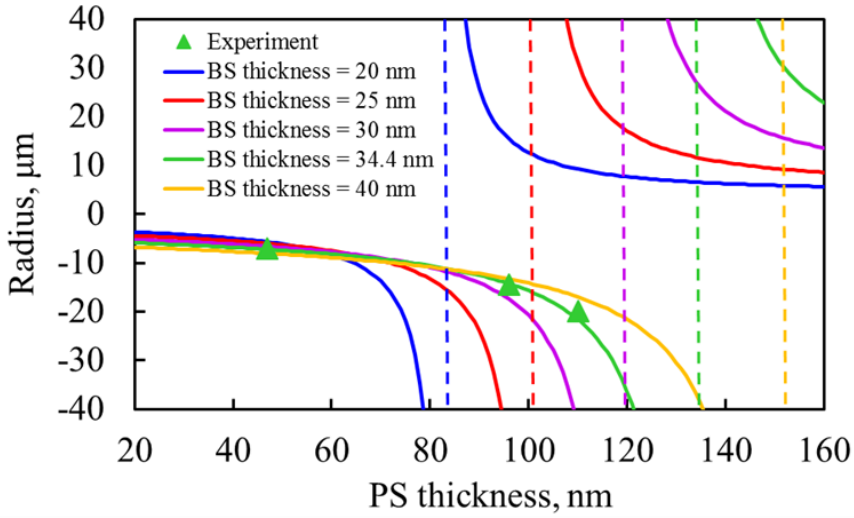


**Figure 6.10**. Plot showing how radius of curvature changes as a function of the PS thickness for different $\beta$-sheet (BS) thicknesses. For composite network we assumed a PS stiffness of 1.8 GPa, silk ionomer layer thickness of 388 nm and stiffness of 11 MPa, and $\beta$-sheet stiffness of 8.6 GPa.

limiting case when the silk ionomer layer thickness is very larger. In this case, the thickness of the PS and $\beta$-sheet layers is much smaller than the thickness of the silk ionomer layer and so we can think of each passive layer (PS layer and $\beta$-sheets) as a spring ($F = kx$).

For the limiting case when the silk ionomer thickness is very large the thickness of the passive layers is not important, and the stiffness is solely determined by the modulus of each layer. The shift in the dotted lines in Figure 6.11 represents the transition to this limiting case. From the figure we see that the theory predicts a silk ionomer layer thickness of 388 nm. Experimentally, the swollen thickness of the silk ionomer layer is ~380 nm. As such we can see that there is a nice agreement between scaling and experiments.

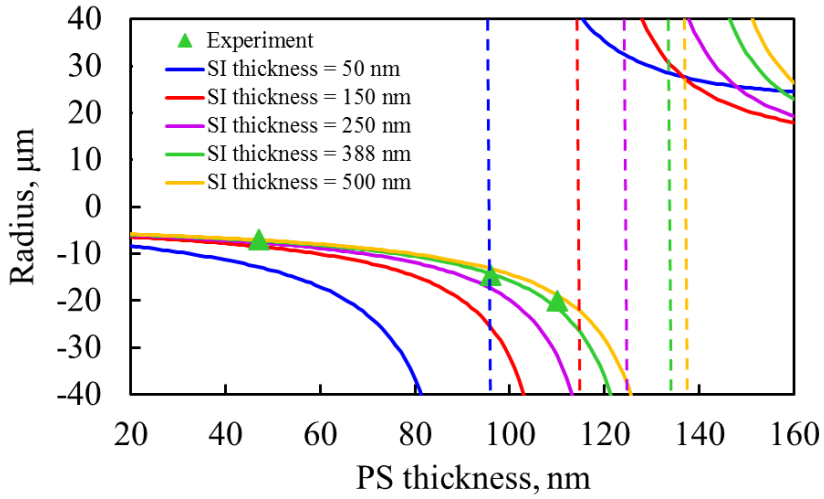


**Figure 6.11**. Plot showing how radius changes as a function of PS thickness for different silk ionomer layer thicknesses. Here we assume $\beta$-sheet thickness of 34.4 nm and stiffness of 8.6 GPa, PS stiffness of 1.8 GPa.

In Figure 6.12a-c we show experimental snapshots of the final equilibrated structure of rectangular microsheets with aspect ratios of 1, 2, and 8. In Figure 6.12d we show the final equilibrated structure of a 15° rhomboids. The rhomboid microsheets have lateral dimensions of $50\mu m \times 100\mu m$. Figure 6.12a shows that for rectangular microsheets with an aspect ratio of 1 the final equilibrated shape is a cylindrical microtube. Figure 6.12b shows that rectangular microsheets with an aspect ratio 2 have trouble forming cylindrical

microtubes. The equilibrated structure in this case closely resembles the structure shown in Figure 6.3p. As mentioned earlier, this indicates that before activation the microsheets have non-zero curvature along the long edge. Figure 6.12c shows that indeed for large aspect ratios ($L/W = 8$) the microsheet cannot fold at all. For the rhomboid microsheets in Figure 6.12d we observe the exact same structure as shown in Figure 6.3d. Overall, the data presented in Figure 6.12 shows strong agreement with our simulations indicating that the computational model is a good predictor for experimental behavior.

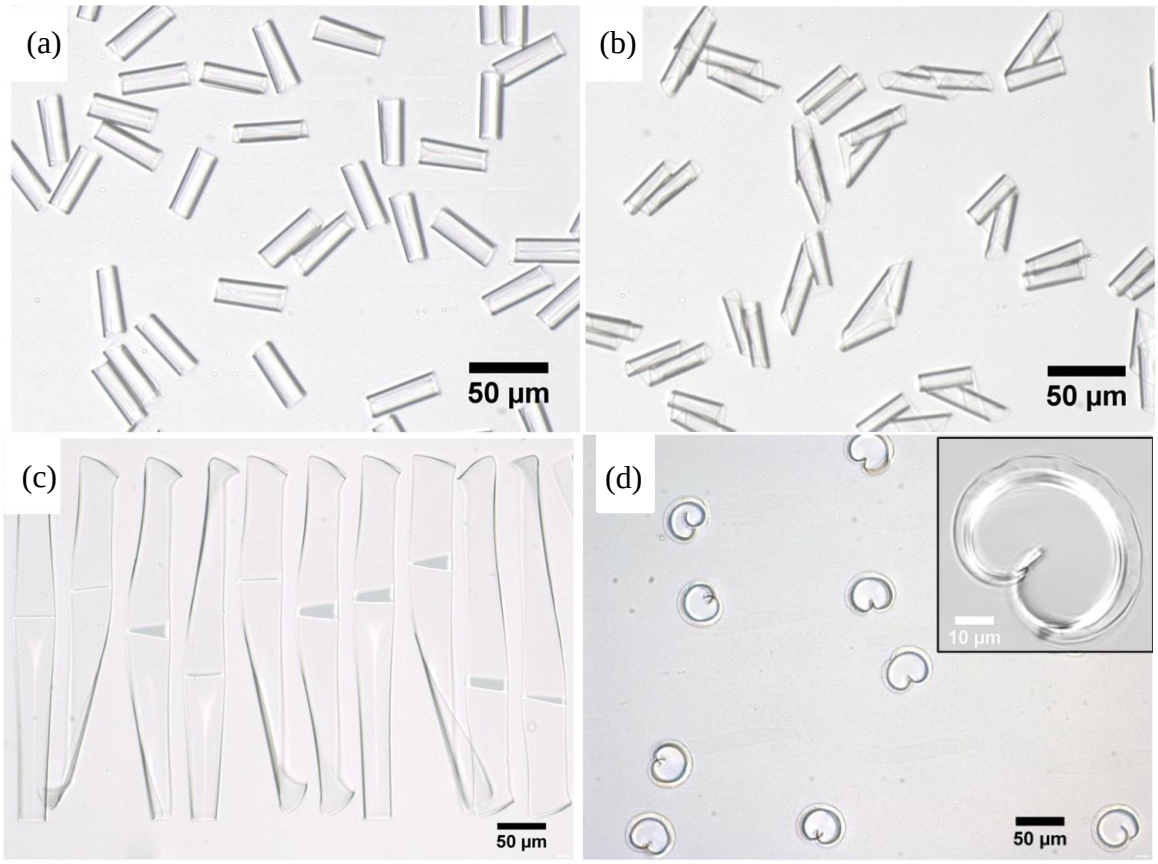


**Figure 6.12**. Experimental snapshots showing final equilibrated shape of spider-silk microsheets with aspect ratios of 1 (a), 2 (b), and 8 (c). The image in figure (d) show final equilibrated shape of a 15° rhomboid microsheet.

## 6.5 Summary

Using the outlined lattice spring method (LSM) we examine how non-uniform swelling proceeds in tri-layered spider-silk composite structures. These structures consist of an active silk ionomer layer that is sandwiched in between passive polystyrene and $\beta$-sheet layers. We illustrate that activation of the silk ionomer layer can be leveraged to achieve large deformations and shape transformations. In particular we show how initially 2D microsheets can be activated to transform into 3D rings, tubules, and helical structures. Our simulations reveal that activation of the silk ionomer layer generates a biaxial stress distribution, which creates a mismatch in interfacial stresses. Depending on the geometry, the stress mismatch at the interface, which arises from the different mechanical properties of each layer, can create large bending moments which alter the shape of the structure.

The LSM model for all geometries shows that stress accumulation is largest in the corners. The analysis of rhomboid geometries shows that stress accumulation can be accelerated by decreasing the angle at each corner. The large angle corners in a rhomboid geometry experience minimal deformation. Meanwhile, the minor corners encounter high stress accumulation, and as a result deform significantly by bending. Since deformation is always initiated at the vertices and can be increased by the angle at that vertex, tailoring the location of vertex points and the corresponding angles within a given geometry can potentially allow researchers to develop novel soft microdevices which can achieve complex tasks like grasping small objects [150-152] and self-locomotion [39, 153, 154].

An added benefit of the trilayered structured, as illustrated in our thermomechanical analysis, is that folding can occur on both sides of the microsheet. Thus, if two active layers

are used each microsheet can become dually responsive, which makes these active composites ideal for microsensing applications. In particular, spider-silk composites are ideal for *in vivo* applications owing to their biocompatible and biodegradable nature. The thermomechanical scaling presented in this study offers a simple method for estimating the folding direction and the final rolled radius of the activated microsheet.

# CHAPTER 7. SELF PROPELLING MICROSWIMMER

## 7.1 Introduction

As robotic swimmers become ever smaller and approach the micro-scale realm, researchers have developed a variety of clever methods to generate propulsion of miniature objects submerged in an aqueous solution. Such micro-scale swimmers could use biocatalytic propulsors, biomimetic nanowires that beat like synthetic flagella, responsive soft materials, and other approaches to propel themselves through a viscous fluid [153, 155-161]. Further advances in micro-swimmer development could yield highly maneuverable and controllable robots that can be targeted to specific locations and autonomously perform complex tasks [40, 162-164], and therefore can be effectively utilized in such applications as drug delivery, bio-sensing, micro-manufacturing, and micro-surgery [165-170].

A critical requirement of synthetic micro-swimmers is their ability to generate self-propelling motion in a fluid environment dominated by viscous forces without using complex mechanical machinery employed by larger macroscopic swimming devices. In this respect, soft responsive hydrogels are especially attractive for designing active microscopic devices. Responsive hydrogels can generate a large amplitude mechanical motion controlled by chemical reactions [171, 172] or in response to various external environmental changes [173, 174] that include changes in temperature, pH, electric and magnetic fields, and light [3, 5, 175, 176]. In other words, the motion of hydrogel swimmers can be directly controlled by changing their environment. Furthermore, hydrogels, which are soft and hydrophilic, are typically biocompatible which makes them

naturally suited to move and maneuver in the aqueous environments found inside living organisms.

In our study, we use computational modeling to design an efficient autonomous micro-swimmer that is actuated using a responsive hydrogel and features a simple, easy-to-implement design. Our simulations show that an on/off periodic application of an external stimulus on the gel swimmer can lead to a rapid self-propelled motion due to periodic swimmer deformations. More specifically, our gel micro-swimmer is made of a

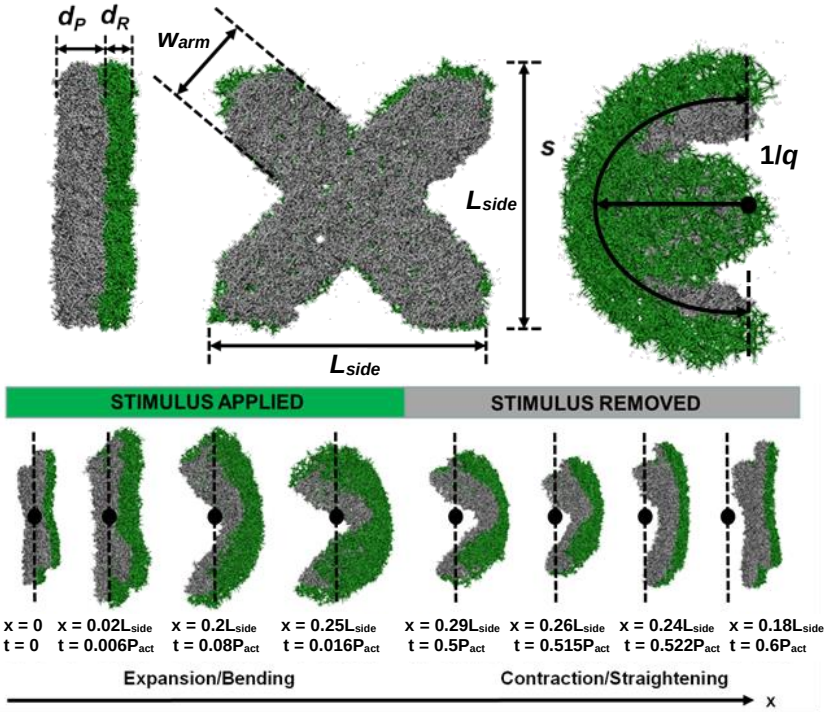


**Figure 7.1**. A micro-swimmer made of a bi-faced hydrogel. (a) The gel swimmer has two layers: responsive layer (green) and passive layer (gray) with thicknesses $d_R$ and $d_P$, respectively. The responsive layer swells and expands when an appropriate external stimulus is applied. (b) Front view of the X-shaped gel swimmer. The swimmer body has length $L_{side}$ and its arms have width $w_{arm}$. (c) The swimmer expands and bends in response to an external stimulus. Its deformation is characterized by curvature $\kappa$ and arc length $s$. (d) Simulation snapshots of the micro-swimmer during one period of its motion. The swimmer propels in the positive $x$ direction. The dotted lines indicate the initial $x$ position of the swimmer's center of mass (solid circle) at $t = 0$. When the stimulus is applied at $t = 0$ the swimmer expands and bends. When the stimulus is removed at $t = 0.5P_{act}$, the swimmer then contracts and straightens to its original configuration.

bifacial hydrogel sheet consisting of two thin gel layers that are bonded together. One layer with thickness $d_R$ swells in response to an external stimulus, whereas the second layer is non-responsive and has a thickness $d_P$ (Figure 7.1a). Except for stimuli sensitivity, both layers are characterized by identical material properties.

When the bi-layered Janus-like gel sheet is exposed to an appropriate stimulus, the initially flat material undergoes simultaneous expansion and bending. The bending is induced by a mismatch between stresses developing in the responsive and passive layers resulting in an internal bending moment. In addition to bending, the layers expand to equilibrate the internal stresses induced by the swelling of the responsive layer, thereby effectively increasing lateral size of the gel sheet.

As presented in Figure 7.1b, we adopt an X-shaped geometry for the gel swimmer with equal height and width dimensions, represented by body length $L_{side}$. With this configuration, four swimmer arms bend towards the swimmer center when a stimulus is imposed. Upon removal of the external stimulus the swimmer straightens back to the original configuration, assuming its initially flat shape. As we show below, this simple micro-swimmer made of bifacial hydrogel can effectively self-propel in highly viscous fluid environment when actuated by a periodically applied external stimulus.

## 7.2 Computational Setup

The responsive gel polymer network is modeled as a random network of interconnected elastic filaments [87, 177]. We generate this polymer network in three steps. First, we randomly distribute seed DPD beads with number density $n_s = 0.5$ within a $(d_R + d_P) \times L_{side} \times L_{side}$ box at the center of the computational domain. Next, we connect closest seed beads with elastic filaments with an average connectivity of 8. Then

we remove triangular portions out of the sides of the rectangular network to form the X-shaped geometry of the swimmer. In our simulations, we keep constant $L_{side} = 40$ and $d_R = 4$, whereas $d_P$ is varied to alter swimmer thickness.

The elastic filaments forming the gel network consists of DPD beads chained by harmonic bending and stretching springs. The stretching spring potential is given by $U_{bond} = \frac{k_{bond}}{2}(r - r_{eq})$, where $r_{eq} = 0.3$ is the equilibrium length and $k_{bond} = 30$ is the spring constant. The bending rigidity for the polymer network is governed by the bending potential, $U_{bend} = k_{bend}(1 + cos\,\theta)$, where $\theta$ is the angle between two interacting beads and $k_{bend} = 50$ is the bending stiffness. The swelling response of the bi-faced hydrogel swimmer is modeled by instantaneously increasing both the equilibrium length $r_{eq}$ and the repulsion $a_{ij}$ between beads forming the responsive gel layer to yield a desired value of the gel swelling ratio $\varepsilon$. When the stimulus is removed, the altered $r_{eq}$ and $a_{ij}$ are restored to their initial values.

### 7.3 Time-irreversible Motion and Swimming Performance

In our simulations we actuate the swimmer by applying an external stimulus with a period $P_{act}$. The stimulus is applied during the first half of the period and is turned off during the latter half. Thus, the swimmer exhibits periodical shape changes as illustrated in Figure 7.1d. When the stimulus is applied at $t = 0$ and the responsive layer swells, the swimmer rapidly expands by increasing the length of the arms. To characterize the forward motion of our gel swimmer in a viscous fluid, we tracked the position of the swimmer's center of mass as it moved. Figure 7.2a shows this position in the direction of the swimmer motion as a function of time. In this figure we normalized the swimmer's displacement $x$

by the initial body length $L_{side}$ and the time by the swelling period $P_{act}$. We find that the swimmer can rapidly propel itself forward in the positive $x$ direction. Analysis of the swimmer's trajectory indicates that the swimmer swelling and de-swelling produce,

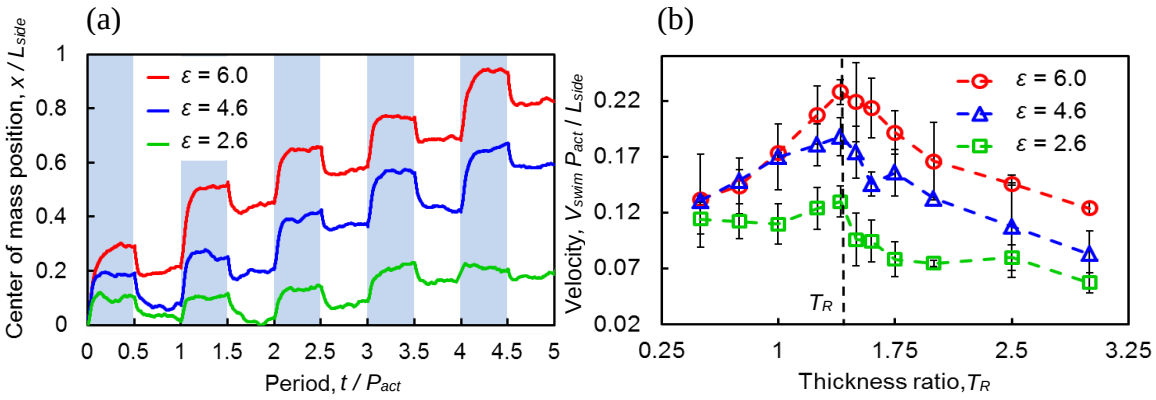


**Figure 7.2**. (a) Center of mass position vs. period for different swelling ratios of swimmer's responsive gel layer. Colored background indicates the portion of time when the stimulus is on. During one period, the swimmer undergoes bending and expansion, moving forward after the stimulus application. Upon stimulus removal, the swimmer undergoes contraction and straightening and moves backwards a shorter distance. The result is a net forward displacement. (b) Swimming velocity $V_{swim}$ as a function of thickness ratio $T_R = d_P/d_R$. Error bars indicate standard deviation from the average value. The optimal thickness ratio $T_R = 1.4$ leading to the fastest swimming speed is indicated by the vertical dash-dotted line.

respectively, forward and backward strokes. When the stimulus is applied and the gel swells, the center of mass moves forward until the swimmer equilibrates at a new position. Gel de-swelling associated with stimulus removal causes the center of mass to move backwards. During the backward stroke, however, the swimmer's displacement is smaller than during the forward stroke, thereby yielding a net forward displacement of the swimmer's body over one period. This motion repeats each time when the stimulus is periodically applied and removed, generating a steady forward motion.

We find that the swimmer moves forward faster when the swelling ratio of the responsive gel layer $\varepsilon = V_s/V_c$ is increased (Figure 7.2a). Here, $V_c$ and $V_s$ are, respectively,

the volumes of an unconstrained responsive gel before and after the stimulus is applied. A larger swelling ratio amplifies the swimmer's deformation and therefore leads to faster swimming. In addition to the swelling ratio, the motion of our simple X-shaped gel micro-swimmer is defined by the relative elasticity of the passive and responsive layers. In our simulations we change the thickness of the passive gel layer $d_P$ while keeping constant the thickness of the responsive layer $d_R$. Since the stiffness of individual network filaments in both gel layers is identical, changing $d_P$ therefore allows us to alter the stiffness ratio between the two layers. Indeed, as we discuss below, the magnitude of the swimmer's center of mass displacement depends on the relative thickness of the gel layers composing the swimmer body.

The average propulsion velocity of the swimmer is summarized in Figure 7.2b where the velocity $V_{swim}$, normalized by $L_{side}/P_{act}$, is shown as a function of the swimmer's thickness ratio $T_R = d_P/d_R$ for three selected values of the swelling ratio $\varepsilon$. Here, we find that increasing $\varepsilon$ systematically increases the swimmer's velocity. However, the dependence on the thickness ratio $T_R$ is not monotonic. The velocity decreases when the thickness of the passive layer is either too small or too large and is maximized for all values of $\varepsilon$ when the thickness ratio is about 1.4. The velocity maximum is most pronounced for the larger swelling ratio $\varepsilon = 6$. In this case the swimmer travels a distance equal to its body length in only about four stimulus cycles. Such a fast propulsion speed is quite remarkable for microscopic systems moving in a highly viscous fluid. In fact, this swimming speed is comparable to that of *E. coli*, which uses about 4 to 5 beating cycles to move one body length [178].

To examine the physics governing the micro-swimmer motion in the inertia-less (nearly zero Reynolds number) fluid, we introduce two parameters that characterize the swimmer shape (see Figure 7.1c). Specifically, we use the average arc length $s$ that represents the extent of the swimmer arms and the average swimmer curvature $q$ that characterizes the magnitude of bending. Figure 7.3a shows how these parameters (normalized by the initial length $L_{side}$ of the swimmer) change in time when the gel swimmer undergoes periodic swelling and de-swelling. When the stimulus is applied, the gel swimmer expands laterally and bends as indicated by the increasing values of the arc length $s$ and curvature $q$. Upon de-swelling of the responsive layer, the arm length decreases, and the swimmer straightens to nearly zero curvature. Since we set the stimulus application period $P_{act}$ to be much longer than the swelling time, the changes in $s$ and $q$ only occur immediately after the stimulus is applied or removed (see Figures 7.3b and 7.3c). During a significant part of the actuation cycle, these parameters remain nearly constant at their respective steady state values, showing slight changes induced by thermal fluctuations.

To swim at nearly zero Reynolds number, a swimmer has to be able to produce time irreversible motion [179]. In the case of our gel swimmer, time irreversible motion arises due to a difference in the rates of change of $s$ and $q$ when the stimulus is either applied or removed. Figure 7.3b and 7.3c show the evolution of $s$ and $q$ at moments immediately after these respective events. The figures indicate that in both of these situations, changes of the swimmer's arc length occur substantially faster than changes of the swimmer's curvature.

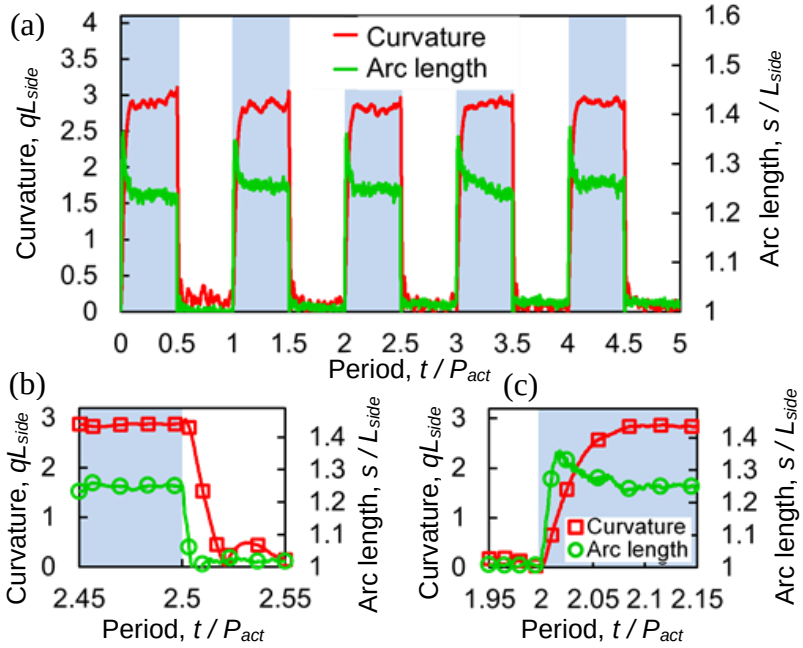


**Figure 7.3**. Swimmer deformation due to periodic application of the stimulus. Colored background indicates portion of time when stimulus is on. (a) Arc length and curvature vs. time for the micro-swimmer with $T_R = 1.5$ and $\varepsilon = 6$. The arc length and curvature rapidly increase to a new equilibrium state after the stimulus is applied and then revert back to their original states upon stimulus removal. The time scale difference between rates of change in arc length and curvature is illustrated during (b) swelling and (c) de-swelling. In both cases, changes in arc length occur more quickly than that of curvature. This results in a time-irreversible motion that yields propulsion in a highly viscous environment.

Thus, the swimmer motion can be approximated by four sequential steps. When the stimulus is applied, the swimmer first extends the arms and then bends. After the stimulus is removed, the arms contract and then straighten, recovering the initially flat shape. As a consequence of this cyclic motion, the swimmer's arm length is greater during bending (forward stroke), than during straightening (backward stroke), thus yielding the required time irreversible motion. In other words, the mismatch in time scales associated with swimmer stretching and bending allows the bi-layered swimmer to move forward throughout a highly viscous environment.

## 7.4 Summary

One of the major advantages of our swimmer is that it can be experimentally implemented using a variety of bi-layered polymeric materials. In fact, bi-layered swimmers could have different shapes, elasticity of layers, and stimuli-induced responsiveness provided that they yield relatively large magnitudes of stretching and bending deformations. The time ratio of these deformations must be relatively small, and the local velocities must satisfy the low-Reynolds number hydrodynamics. In other words, our swimmer design allows for a variety of experimental realizations that could involve a broad class of polymeric materials. Indeed, ongoing developments in designing actuating bi-layered responsive gels offer a number of materials that demonstrate large amplitude deformation response to external stimuli [148, 160, 180-184] that could be potentially used to build our gel swimmer. Furthermore, several groups have successfully demonstrated ground locomotion ("walkers" or "jumpers") using responsive gels, further emphasizing the utility of these materials in soft robotic applications [160, 173, 180, 185]. We note that the systems in these studies are on the order of hundreds of microns, a relatively large scale, whereas our gel swimmer design is directly applicable to micrometer-sized and even smaller systems. Recent progress in synthesizing bi-layered gels shows promise in downscaling such responsive materials to micrometer and nanometer scales [186]. For example, recombinant DNA (rDNA) technology is a promising method that can be utilized to synthesize micrometer sized gels with accurately controlled molecular architecture. Through this approach researchers were able to generate film assemblies as thin as $100\ nm$ [187].

In summary, we used computer simulations to design a self-propelling gel micro-swimmer actuated by a periodically applied external stimulus that can move unidirectionally in a fluid environment dominated by viscous forces. Our simple design establishes design principles and paves the way for developing more sophisticated swimmers that can be enriched with additional functions and capabilities. For example, adding extra responsive sections may be employed for directing the swimmer in three dimensions and controlling its turning [40]. Using binding molecules at the front, our swimmer could be potentially used for uploading and transporting different microscopic cargo [188]. Finally, since external stimuli can simultaneously actuate multiple independent gel swimmers, a swarm of such microscopic devices could be harnessed to accomplish tasks that are unachievable for a single micro-swimmer. Future computational studies and experiments are therefore needed to explore these exciting research paths.

# CHAPTER 8. ACTIVE MICROCAPSULES

## 8.1 Introduction

Micrometer-sized functional devices are currently paving the way for future advances in medicine. By leveraging new developments in polymer science and nanotechnology researchers are achieving *in vivo* tasks which were previously not possible, like closed-loop insulin delivery [189], on-site drug testing [190], and lactate tracking via enzymatic bioreactors [30]. Performing *in vivo* tasks like these is challenging due to toxicity constraints and the immune response from the host's body [191], which put a significant limitation on the materials from which such microdevices can be fabricated. Bio-friendly hydrogels like dextran and chitosan become a promising material of choice for designing biomedical microdevices [192, 193]. Their inherent high porosity and hydrophilic nature makes them structurally similar to natural tissue.

The large volume changes throughout the volume phase transition (VPT) that can be controlled by specific environmental stimuli provide an effective mechanism for microscale actuation. In recent years the stimuli-sensitive hydrogels have been successfully harnessed to achieve actuation in microscopic swimmers [39, 40], self-folding materials [17, 18, 194], micro-sensors [195, 196], and controlled release of drugs [88, 197-199].

Here, we use mesoscale computer simulations [51] to design a gel-actuated microdevice that mimics the function of phagocytes, biological cells that protect the organism by collecting cellular debris and harmful foreign particles, such as viruses. When actuated by an appropriate external stimulus, our phagocyte-inspired synthetic microdevice can selectively capture and isolate specific nanoparticles dispersed in the surrounding

solvent. An active microcapsule such as this could be potentially used to monitor and track molecular biomarkers in real time [200]. Alternatively, the device itself could be viewed as a primitive cell model [201]. In the swollen state, a hydrogel has high porosity and structurally resembles the mammalian cytoplasm [202].

The components of our microdevice are shown in Figure 8.1. The microdevice consists of a rigid shell with perforated holes (Figure 8.1a), a spherical microgel particle that is located inside the shell (Figure 8.1b), and a copolymer brush with sticky end groups that is tethered to the spherical shell at the perforation sites (Figure 8.1c). The shell provides structural integrity to our device and separates the device interior from the external solvent, whereas the shell perforations serve as entry ports, allowing controlled transfer of nanoparticles into the capsule interior. The stimuli-responsive lightly cross-linked microgel that undergoes an order of magnitude change in volume near the critical point induces transport into the microcapsule by enabling formation of large bulbs at the perforation sites when swollen. The nanoparticle flux at the perforations is regulated by the polymer brush that keeps captured nanoparticles from escaping and prevents the undesired transfer of nanoparticles from outside the capsule when the gel is collapsed.

The size of the active microcapsule considered here is in the micrometer range. The size of the microgel is such that in the collapsed state it is fully enclosed within the internal capsule cavity, whereas in the swollen state it is sufficiently large and compliant to protrude through the capsule pores. Thermosensitive microgels in this size range have characteristic swelling times from microseconds to seconds [107]. Capsule pores are selected to be smaller than the collapsed microgel to prevent the microgel from leaving the capsule, but large enough to allow the formation of large microgel bulbs. Finally, the gating brush

copolymers are set to be sufficiently long to gate the pore and to bind to attractive end groups of copolymers tethered to the opposite pore side.

In practice, a variety of experimental realizations are possible for microcapsule components. For example, the rigid shell can be fabricated from silica or polystyrene, which have been used to create mesoporous shells in the past [203, 204]. Rigidity can be enforced by tailoring the shell thickness. Examples of suitable hydrogel materials include biocompatible dextran [205], chitosan [206], and poly(N-vinylcaprolactam) (PVCL) gels [207]; however, if biocompatibility is not a concern, then PNIPAM-based gels could be used. Temperature-sensitive microgels with embedded electromagnetic particles, such as carbon microcoils and plasmonic gold nanorods, can be controlled via electromagnetic irradiation [105, 208]. PEG chains with methyl and amine end groups could be used to create the polymer brushes gating the shell ports. The amine end groups could be functionalized to the shell [209-211] and the methyl end groups, which when immersed in solvent experience a mutual attraction due to their hydrophobic nature, could be used to close the perforations in the shell.

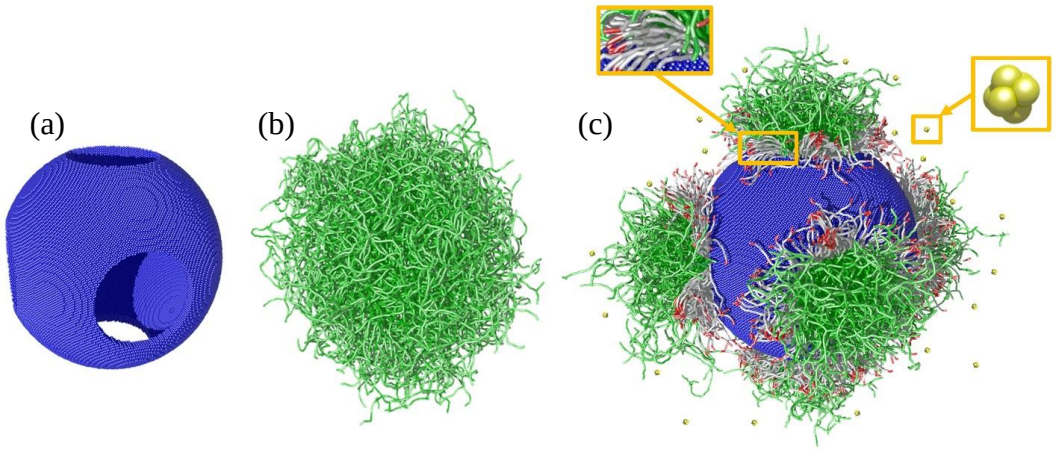


**Figure 8.1**. (a) Rigid shell with six perforated pores. (b) Spherical microgel swollen in good solvent. (c) Phagocyte-inspired microdevice in swollen state immersed in nanoparticle-rich solvent. The close-ups show diblock-copolymer brush decorating shell pores (red and gray) and a nanoparticle (yellow). The red monomers at the ends of copolymer chains are mutually attracted to each other, while the gray monomers are repelling.

The smart microcapsule operates as follows. Initially, when the microgel is collapsed inside the shell, the end groups of the polymer brush experiencing mutual attraction bridge the pores and prevent nanoparticle access to the shell interior. When the microgel swells due to temperature changes, it breaks through the polymer brush, enabling contact with the nanoparticle-rich external solvent. Once the nanoparticles bind to the microgel and the stimulus is removed, they are brought into the shell interior by the retracting microgel and remain isolated by the gating brush. We probe the capturing efficiency of our active microcapsule and examine how parameters, such as the actuation frequency and nanoparticle adhesiveness, affect nanoparticle capture and retention inside the microcapsule interior.

## 8.2 Computational Setup

To model the polymeric chains in the gel and polymer brush, we add on top of the DPD potential, a harmonic bond potential and a bending angle potential. The energy for the bond potential is given by $U_{bond} = k_{bond}(r - r_{eq})^2$, where $k_{bond}$ is the bond stiffness and $r_{eq}$ is the equilibrium separation length between beads. The energy for the angle potential is given by $U_{bend} = k_{bend}(1 + \cos(\theta))$, where $k_{bend}$ is the bending stiffness and $\theta$ is the angle between two polymer bonds sharing a common bead. The bending stiffness for all polymers (microgel and polymer brush) is set to $k_{bend} = 10$ and the bond stiffness is set to $k_{bond} = 35$. For our DPD parameters we specify $r_c = 1$, $\gamma = 4.5$, $k_BT = 1$, $\rho = 3$, and $\Delta t = 0.01$. All dimensional values hereafter are expressed in DPD units.

We conduct our simulations in a periodic box with a size of $100x100x100$. The spherical gel which sits inside the shell is generated by first randomly distributing 3,600

crosslink points inside a $60x60x60$ cubic domain [120]. The crosslink points are then connected with elastic filaments, where the average connectivity and number of beads per chain are approximately 4 and 12, respectively [120]. Once the gel is created the spherical shape is cut out of the cubic domain and disconnected segments are removed using a depth first search algorithm [120] (Figure 8.1b). After this, the final spherical gel is equilibrated in DPD solvent. This approach allows us to create lightly crosslinked polymer networks which are capable of experiencing large changes in volume. To swell the gel, we change the network-solvent repulsion to $a_{P-S} = 65$ and to collapse the gel we set it to $a_{P-S} = 125$. The self-repulsion for beads of the same species is set to $a_{ii} = 75$. The parameters $a_{P-S} = 65$ and $a_{P-S} = 125$ correspond to respective Flory-Huggins [120] values of approximately 0.5 (swollen state) and 0.9 (collapsed state), typical for PNIPAM [10]. The volume change for a spherical particle between the collapsed and swollen states is approximately 12 times. The volume change can be amplified by increasing the chain length and decreasing the crosslink density. Using gels with a low swelling ratio ($\alpha = V_s/V_c$) will hinder bulb formation when the gel protrudes through the perforation. To embed the gel in the shell we first collapse the gel and then generate the perforated shell decorated with polymer brushes around the gel (Figure 8.1c).

The characteristic swelling time for an unconstrained gel is determined by first collapsing the spherical gel and then instantaneously changing the solvency to swell the gel. The volume evolution of the gel during swelling is compared with the gel swelling kinetics predicted by Tanaka's theory [120], as outlined in Chapter 3. The characteristic swelling time $\tau_{swell}$ and collective diffusion coefficient $D$ are extracted by fitting the simulation data to the Fourier series solution.

The rigid spherical shell (Figure 8.1a) is comprised of ~169,000 DPD particles which are placed on a cubic lattice with a spacing of 0.5. The radius of the shell is 25 and the thickness is 2. The shell has six symmetric holes with a radius of 10. The perforations were chosen to be symmetric for simplicity. The radius of the perforations controls the amount of gel that exits the microcapsule, in our case 40% of the gel exits through the circular microcapsule pores. The mass of the DPD beads in the shell is adjusted so that the shell density is 3. The area around each perforated hole is functionalized with 215 diblock-copolymer chains which make up the polymer brush (1290 chains total). Each copolymer chain is formed from 20 DPD beads and is attached to the shell at randomly selected sites near the perforation (Figure 8.1c). End groups of the copolymers are composed of three DPD beads that experience a mutual attraction $a_{EG-EG} = 55$ allowing the polymer brush to close the perforated holes when the gel is in the collapsed state. The interaction between the gel network and the polymer brush is set to $a_{N-PB} = 100$ to prevent entanglements during swelling/deswelling transitions. The bending stiffness for all polymers (gel and polymer brush) is set to $k_{bend} = 10$ and the bond stiffness is set to $k_{bond} = 35$, with $r_{eq} = 0.6$.

Each of the nanoparticles, which is comprised of six DPD beads, is treated as a rigid body (Figure 8.1c). We disperse 500 of these nanoparticles in the solution, which corresponds to a concentration of $5.35x10^{-4}$ nanoparticles per unit volume. The polymer network-nanoparticle repulsion $a_{P-Nano}$ is set to 60, 65, and 75, respectively, for attractive, neutral, and repulsive nanoparticles. It should be noted that when referring to the nanoparticles, the words attractive, neutral, and repulsive are used with respect to the swollen gel, where $a_{P-S} = 65$. When the gel is in the deswollen state $a_{P-S} = 125$ all

nanoparticles are effectively attracted to the gel since $a_{P-S} = 125 > a_{P-Nano}$. Initially, the nanoparticles are randomly distributed outside the capsule.

We can estimate the number of nanoparticles captured by the smart microcapsule through advection using the volume of the gel bulbs $V_{bulb}$ and the nanoparticle concentration in the external solvent $C_{ext}$. To find the volume of the gel bulbs we construct a surface mesh which encloses the corresponding gel network [94, 120]. By multiplying the bulb volume by the nanoparticle concentration in the external solvent and assuming perfect attachment of nanoparticles to the gel chains, we estimate that approximately $N_{adv} = V_{bulb}C_{ext} = 20$ nanoparticles can be captured through advection per actuation period. A similar estimate for diffusive transport can be made using Fick's first law $N_{diff} = D_P C_{ext} A_{bulb} \tau / l_{diff}$ . Here, $N_{diff}$ is the number of captured particles that were brought in by diffusion, $D_P$ is the nanoparticle diffusion coefficient, $A_{bulb}$ is the area of the bulbs exposed to the external solvent, $\tau$ is time, and $l_{diff} = \sqrt{4D_P \tau}$ is the characteristic diffusion length scale. We define the Peclet number $Pe = \frac{advective\ capture}{diffusive\ capture}$ and find that for the most efficient nanoparticle capture in our device ($P_{act} = 3\tau_{swell} - 10\tau_{swell}$) that corresponds to a Peclet number between 2 to 4.

The above analysis can be applied to estimate expected performance of different experimental implementations of our microdevice. Consider a swollen $5\mu m$ diameter PNIPAM gel particle placed in a rigid perforated shell that would produce bulbs with volume 200 $\mu m^3$ (assuming 40% of the gel exits the perforations). The corresponding surface area of the bulbs is roughly 30% of the surface area of a freely swollen microgel.

Assuming the nanoparticles are dispersed in water and have the diffusion coefficient $D_P \approx 20 \frac{\mu m^2}{s}$, for a 50 $ms$ activation period we estimate that $N_{diff} \approx 17$ and $N_{adv} \approx 60$.

## 8.3 Characterizing Activation Period

In Figure 8.2, we illustrate the function of our microdevice over one period $P_{act}$ of application of the external stimulus, leading to a gel temperature change. The external stimulus is applied from $t = 0$ to $t = P_{act}/2$ and is removed during the second half of the period. We set $P_{act} = 100\tau_{swell}$, where $\tau_{swell}$ is the characteristic swelling time of an

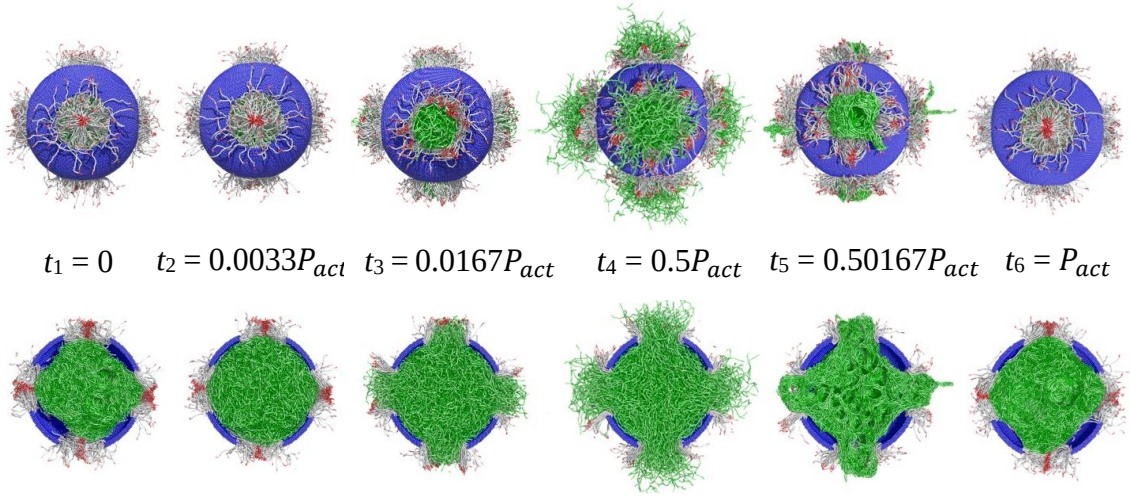


**Figure 8.2**. (a) The top row shows snapshots of the microdevice during swelling/deswelling transition for period $P_{act} = 100\tau_{swell}$. (b) The second row shows the corresponding cross-sectional views of the microdevice. Initially, the microgel is collapsed inside the shell and polymer brushes close the pores. At $t_1$, the external stimulus is applied causing the microgel to swell. Swelling is achieved via a three-step process. First, the gel rapidly adsorbs solvent within the capsule and swells to fill the shell volume ($t_2$). Further swelling proceeds via diffusion of the external solvent through the semi-permeable polymer brush closing the shell pores. The gating brush experiences outward pressure due to expanding microgel. Once the pressure exceeds the critical magnitude the polymer brush yields, allowing the gel to exit through the pores ($t_3$). The microgel continues to expand forming bulbs protruding from the shell pores until it reaches its final equilibrium shape ($t_4$). At $t_4$, the external stimulus is removed causing the microgel to deswell and retract. Upon deswelling, the polymer network becomes highly heterogeneous, as the gel and solvent phase separate ($t_5$). After the microgel fully retracts, polymer brushes bridge the pore isolating collapsed microgel within the shell ($t_6$).

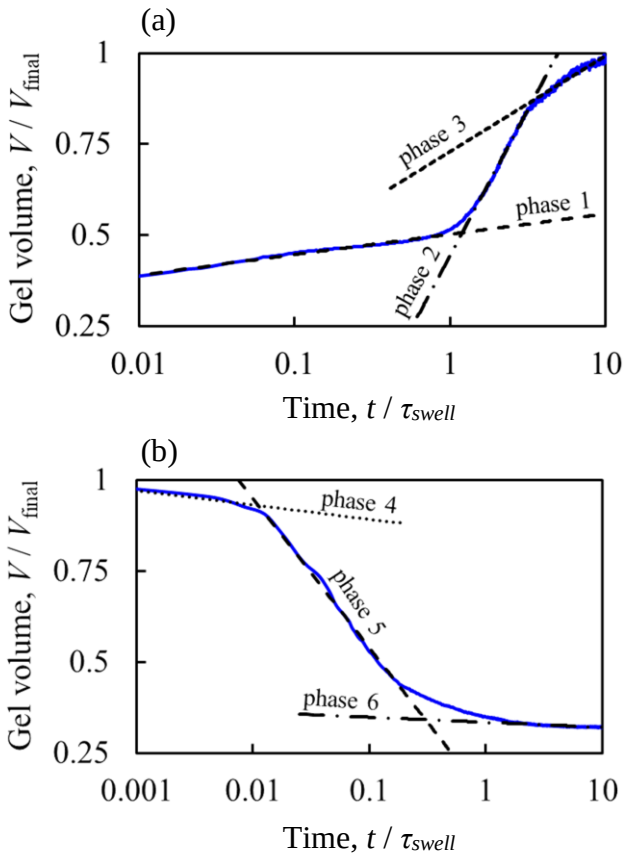


**Figure 8.3**. Figures showing how gel volume changes during swelling/deswelling in a phagocyte-like microdevice. Six different swelling/deswelling regimes are found, which are highlighted by the black dotted lines. Plot (a) shows the first 3 regimes for swelling and plot (b) shows the other 3 regimes for deswelling.

unconstrained microgel. Upon application of the stimulus, favorable gel−solvent interactions lead to microgel hydration and swelling, which causes the gel to dramatically expand in volume. The changes in temperature in our model are implemented by varying the polymer network−solvent repulsion parameter, $a_{P-S}$ which accounts for a change in the Flory−Huggins parameter [120]. Decreasing $a_{P-S}$ corresponds to gel swelling, whereas increasing $a_{P-S}$ causes the gel to collapse.

Swelling/deswelling of a gel enclosed in a microcapsule involves six phases as shown in Figures 8.2 and 8.3. In phase 1, the gel adsorbs the solvent within the microcapsule and expands to fill its internal space ($t_2$). This initial swelling happens on a

time scale comparable to $\tau_{swell}$. Further swelling in phase 2 proceeds by adsorbing solvent that diffuses though the polymer brush, gating the shell ports. Brush porosity and pore size define the solvent influx rate. Gel swelling imposes an outward pressure on the gating brush until contact between the brush end groups is broken and the pores fully open, allowing the gel to expand through the pores ($t_3$). After this, the microgel continues to swell, forming bulb-like structures that feather out of the capsule. In phase 3 the bulbs grow in size until the microgel attains its final shape ($t_4$). As the microgel exits the capsule, the solvent penetrates into the capsule interior. In the fully swollen state, nearly 40% of the gel exits through the microcapsule pores. This amount depends on the swelling ratio of the gel, the perforation size, and the difference between the shell and microgel volumes. The bulb formation is relatively slow compared to $\tau_{swell}$ due to the friction between the microgel and the solid shell.

When the stimulus is removed, the gel collapses and retracts into the capsule interior, expelling solvent from within the capsule. At the onset of deswelling, in phase 4, the gel chains bundle, leading to a rapid gel contraction. In phase 5 the microgel chains collapse, decreasing bulb porosity and impeding solvent outflow through the pores, which slows gel contraction ($t_5$). In phase 6, the collapsed bulbs slowly retract into the microcapsule interior. Once this is done, the polymer brushes bridge the capsule ports, isolating the capsule interior from the outer solvent ($t_6$).

### 8.4 Diffusive vs. Advective Capture

To explore the ability of our microdevice to selectively capture and isolate nanoparticles, we placed the microcapsule into a nanoparticle-rich solvent. In our

microdevice, the transport of nanoparticles into the capsule interior is facilitated by advection and diffusion, whereas the retention of nanoparticles in the capsule depends on the strength of gel-nanoparticle adhesion. Advective transport arises from the gel volume change as the gel swells/deswells. During swelling, solvent rushes into the network to hydrate the polymer, bringing along suspended nanoparticles. Thus, the number of nanoparticles transferred into the capsule by advection is proportional to the volume of solvent entering the shell. Once the gel is swollen and forms the bulbs protruding from the shell pores, the nanoparticles can diffuse into the gel network. The number of nanoparticles captured through diffusion is proportional to the bulb area and the time the microgel is in contact with the external solvent. During gel deswelling, the collapsing microgel expels solvent from the shell interior. If the nanoparticle-gel adhesion is not sufficiently strong, the escaping solvent can wash some nanoparticles away, reducing the device capture efficiency. Thus, microgel-nanoparticle affinity facilitates nanoparticle retention.

Figure 8.4a shows how the nanoparticle concentration changes within the microdevice over one period for attractive, neutral, and repelling nanoparticles. The color dotted lines represent the concentration in the microgel, whereas the color solid lines show the concentration inside the shell. The black solid line shows the microgel volume. In this simulation, we set $P_{act} = 100\tau_{swell}$, which is sufficiently long for the swelling microgel to form fully developed bulbs. During the first half of the period, $0 < t/P_{act} < 0.5$, when the stimulus is applied and the microgel swells, the nanoparticle concentration in the microgel rapidly increases. Almost all of the nanoparticles remain trapped in the bulbs, protruding outside the shell, with practically no particles reaching the capsule interior. For $0 < t/P_{act} < 0.5$, we find a weak dependence of the particle concentration on the

nanoparticle-gel interaction. The rapid concentration increase during the initial microgel swelling $t/P_{act} < 0.1$ is associated with advection of nanoparticles into the expanding gel network, adsorbing solvent. Comparing the black line with the colored dotted lines in Figure 8.4a, one can see that the initial rapid increase in the nanoparticle concentration coincides with the rapid increase in swelling gel volume. After that advection-driven concentration jump, the concentration gradually increases with time due to nanoparticle

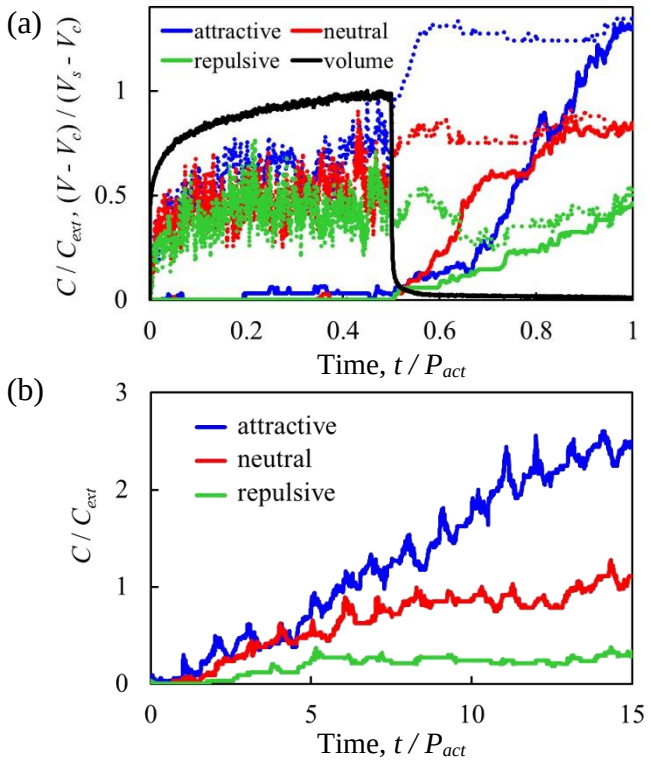


**Figure 8.4**. (a) Evolution of nanoparticle concentration during one period of actuation with $P_{act} = 100\tau_{swell}$ for nanoparticles with different adhesiveness. The dotted color lines show the concentration in the microgel. The solid color lines show the nanoparticle concentration inside the microcapsule. The solid black line shows the volume of the microgel. (b) Nanoparticle concentration in the microcapsule during 15 periods with $P_{act} = 6.7\tau_{swell}$ for particles with different adhesiveness. Note that after multiple actuation periods the concentration of attractive particles exceeds the concentration in the external solvent $C_{ext}$, whereas the concentration of repulsive particles remains below that concentration. The attractive, neutral, and repulsive particles have $a_{N-Nano}$ equal to 60, 65, and 75, respectively. Microgel volume $V$ is normalized with respect to the volumes in collapsed $V_c$ and swollen $V_s$ states.

diffusion. Diffusive transport is more pronounced for attractive particles that bind to the microgel, whereas advective transport acts equally well on all types of nanoparticles.

The stimulus is removed during the second half of the period, $0.5 < t/P_{act} < 1$. This causes the microgel network to collapse and retract into the capsule interior. As the bulbs begin to collapse, the solid color lines in Figure 8.4a, representing the concentration of nanoparticles within the shell, start to increase, indicating that microgel retraction brings nanoparticles into the capsule interior. By the end of the actuation period, the dotted and solid concentration lines converge as the microgel retraction completes transferring the nanoparticles into the capsule. During the retraction phase, nanoparticle concentration within the capsule is strongly affected by the type of nanoparticle-microgel interaction. When nanoparticles are sticky, they remain attached to the gel as the bulbs retract. As a result, the concentration within the capsule grows, exceeding the concentration in the outer solvent. When the nanoparticle-microgel interaction is repulsive, the majority of nanoparticles that enter the hydrogel network during the swelling phase are removed by the solvent escaping from the collapsing gel network. This causes the concentration of repelling nanoparticles within the capsule to remain relatively low, with a small number trapped sterically in the polymer network. Neutral nanoparticles are more likely to remain within the gel network during the deswelling than repulsive particles, confirming that the interaction strength regulates the capture efficiency. Thus, the microdevice can selectively capture nanoparticles with favorable microgel interactions from a nanoparticle mixture. We note that the nanoparticle concentration does not change after the microgel collapses and the gating brushes close the capsule ports, suggesting that the brushes indeed prevent transport of nanoparticles into the capsule interior.

When the microgel swells, nanoparticle capture first happens due to the faster advective nanoparticle transport and then due to the slower diffusive transport. For a given nanoparticle concentration, the advective transport is proportional to the amount of solvent that enters the capsule, whereas the diffusive transport is proportional to the time that the gel stays in the swollen state with bulbs exposed to the nanoparticle-rich solution. Thus, the length of the actuation period can alter the capture performance of the microdevice. When the period length decreases, the relative contribution of the slow diffusive transport is reduced, whereas the capture due to advective transport remains unaffected. One can thus expect that, for a fixed time interval, a shorter actuation period can enhance the overall capture performance by increasing the contribution of fast advective capture. This relationship, however, breaks down for $P_{act} < 2\tau_{swell}$ due to poor bulb formation

In Figure 8.4b, we keep the same simulation time as in Figure 8.4a, $T_{tot} = 100\tau_{swell}$, and set a shorter actuation period, $P_{act} = 6.7\tau_{swell}$. The simulations show that by decreasing the period from $P_{act} = 100\tau_{swell}$ to $P_{act} = 6.7\tau_{swell}$, the adhesive nanoparticle concentration (blue line) increases approximately $2.1x$. This indicates an increased contribution of advective transport due to the periodic swelling/deswelling of the microgel. Figure 8.4b shows that the nanoparticle concentration depends on the nanoparticle-microgel interactions. Similar to the longer actuation period, repelling particles do not accumulate in the capsule, even after 15 actuation periods. Their concentration remains approximately the same as after the first period and below the concentration outside the capsule. Furthermore, the concentration of neutral nanoparticles remains nearly constant over multiple periods and is approximately equal to the concentration in the external solvent.

In Figure 8.5, we examine how the nanoparticle capture rate varies with the actuation period $P_{act}$. The figure reveals that particle capture is maximized when $P_{act}$ is between $3 - 10\tau_{swell}$. In this optimum range, the period of actuation is long enough to ensure that the gel has enough time to swell and form bulbs that, in turn, enable the advective transport of nanoparticles into the swelling microgel. A longer than optimum actuation period reduces the overall capture efficiency by increasing the time during which the transport of nanoparticles relies on the relatively slow diffusion. The physical time scales corresponding to the optimum actuation period are determined by the size and collective diffusion of the microgels [107]. For thermosensitive microgels like PNIPAM, with sizes from $100\ nm$ to $200\ \mu m$, the optimal actuation is achieved for periods from $10\ \mu s$ to $100\ s$, depending on the specific microgel size.

Figure 8.5 also shows that the maximum rate of particle capture depends strongly on the nanoparticle-microgel interaction. The capture rates of neutral and repulsive particles are $\sim 3 - 10x$ slower than that of attractive particles. This points to the high

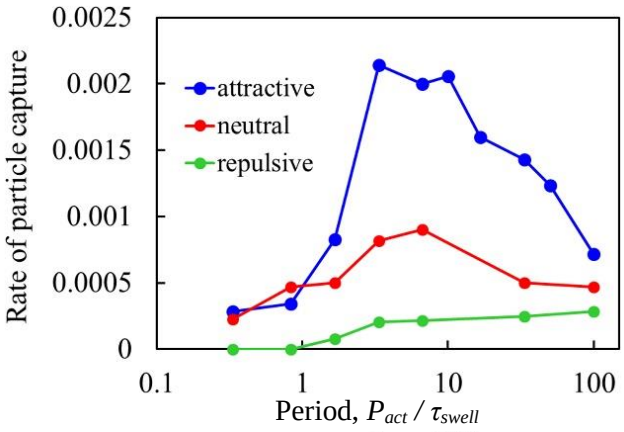


**Figure 8.5**. Capture rate for nanoparticles with different adhesiveness as a function of the actuation period $P_{act}$. The capture rate is maximized for attractive and neutral nanoparticles when actuation period is about $\tau_{swell}$, indicating that the capture is enhanced by advective transport of solvent into periodically swelling microgel. The attractive, neutral, and repulsive nanoparticles have $a_{N-P}$ equal to 60, 65, and 75, respectively.

selectivity of the microdevice toward capturing nanoparticles that have an affinity with the polymeric microgel. We find that repulsive particles do not exhibit a local maximum with increasing $P_{act}$, suggesting a weak effect of the advective transport on capturing of repulsive particles. Such particles are washed away by the solvent leaving the capsule as the gel deswells, unless they have sufficient time to diffuse deeper into the gel network, increasing the probability of being sterically trapped. Overall, Figure 8.5 shows that capture selectivity can be realized by altering the gel-nanoparticle interactions and that the period of microdevice actuation is a defining parameter that determines the optimal operation of the device for nanoparticle capture.

## 8.5 Experimental Realization

Numerous fabrication methods have been developed for mesoporous microshells. Haufova et al. [204] use alkoxysilane precursors in a sol-gel process to grow a silica shell onto a spherical alginate microgel. The average diameter of the alginate particles was approximately $40 - 60\ \mu m$ and the average shell thickness varied between $230\ nm$ and $2.3\ \mu m$. The thickness of the silica shell was dependent on the quantity of alkoxysilanes precursor used. In addition to the silica shells, researchers have also shown that mesoporous polystyrene (PS) particles can be fabricated using a variety of methods, such as radical polymerization [212] and toulane swelling and evaporation [203].

Takahashi et al. [212] mix hydrocarbon (styrene), fluorocarbon oil, and sodium dodecylsulfa (surfactant) to create an emulsion of Janus styrene and fluorocarbon oil droplets. Upon polymerization the styrene is converted to polystyrene and a hollow shell around each fluorocarbon oil droplet is formed. A single hole in the structure is created

when the fluorocarbon oil is removed from the PS shell. The average diameter of the PS particles was 1.3 $\mu m$ and the average hole size was 0.8 $\mu m$ with a 0.9 $\mu m^3$ volume. In the work of Im et al. [203], the PS beads were initially swollen with toluene and then immersed in liquid nitrogen. The volume shrinkage associated with the freezing of toluene created voids in the PS structure. Upon reheating, the toluene evaporates, and the corresponding evaporative flux creates a hole in the PS shell. This method of freezing then evaporating solvent domains to created voids in the underlying structure can be applied equally well to non-spherical geometries and other organic polymers besides PS. The average PS shell diameter in the work of Im et al. was around $560\ nm$. The size of the holes can be directly estimated from the diameter of the non-swollen and swollen PS beads. It should be noted that both PS and silica shells discussed above have been shown to be biocompatible [213, 214] and are amenable to amine and carboxyl functionalization [209-211].

Thermosensitive microgels have been extensively investigated over the years. As a result a variety of fabrication methods using microfluidic devices [215], emulsion/precipitation polymerization [216], and lithographic techniques [217] have been developed [218]. Droplet-based microfluidic techniques can generally produce microgel particles ranging from $10\ \mu m$ to $1\ mm$ in size. Photo lithographic techniques are also capable of producing similarly sized gel particles. Both microfluidic and lithographic methods allow good control over the size and morphology of individual microgel particles. These methods however are usually slower than batch processing techniques like emulsion and precipitation polymerization. Batch fabrication methods are also capable of producing much smaller particles, around $100\ nm$ in diameter [63, 216, 218]. The fabrication technique chosen should be balanced with the crosslinking chemistry of the gel. For pH

sensitive gels like chitosan and alginate photolithographic techniques like electrospraying [139, 218, 219] are common. Meanwhile, for thermosensitive gels like PNIPAM, precipitation polymerization is more widely used [13, 218].

The specific elastic properties of a given thermosensitive microgel largely depend on the polymer network (PNIPAM, dextran, chitosan, etc.) and degree of crosslinking. Throughout the volume phase transition typically an order of magnitude change in the elastic modulus is observed. In the swollen state the Young's modulus of PNIPAM is roughly $10\ kPa$ [12, 220]. In the deswollen state the Young's modulus can increase by an order of magnitude to roughly $100\ kPa$ [12, 220]. For some microgels the volume phase transition can be discontinuous which is also reflected in the mechanical properties, where a jump in stiffness can be seen [12]. The swelling/deswelling time for a given microgel tends to decrease as the gel stiffness increases. Thus, for shorter sampling times stiffer gels may be preferred. In the work of Muniz et al. the authors showed that the microgel stiffness can be improved by crosslinking a polymer network (PNIPAM) within another network (polyacrylamide) to create a semi-interpenetrated polymer network [221]. Comparing the elastic moduli in the swollen (deswollen) state to the corresponding moduli for a single component polyacrylamide gel the authors note a $17\%$ ($50\%$) increase in stiffness. Devices with different sizes can be fabricated depending on the application. However, increasing the size of the embedded gel, can dramatically increase the swelling time and, hence, negatively affect the capture rate. As such, sufficiently short gel swelling time limits the overall size of the microgel and the device.

Recently locally heated thermosensitive microgels have been shown to experience fast kinetics with $60\ ns$ collapse times. This is significantly faster than the predictions of

Tanaka's theory [9], due to nonhomogeneous heating which facilitates the ejection of solvent during gel collapse. Thus, such locally heated thermosensitive gels may offer shorter sampling times which are not accessible with similarly sized pH or light sensitive gels [105]. Utilization of such gels can be preferable for the use in the smart microcapsule since it allows overall faster actuation times and therefore more efficient nanoparticle capture. The polymer brush in our active microcapsule design can be realized using linear heterobifunctional chains. The polymer chain could be functionalized with an end group like carboxyl or amine on one end which would permit attachment to the mesoporous shell. On the opposite end a methyl end group could provide a mutual attraction between chains due to hydrophobic interactions. One example of such a heterobifunctional chain is Methyl-PEGn-Amine [222]. The flexibility of this chain could be controlled by varying the number of PEG monomers between the Methyl and Amine end groups. It should be noted that Methyl-PEGn-Amine is just one example of a potential chain which could be used to construct the proposed polymer brush. A variety of alternative functional groups could be used instead of the amine and methyl end groups [223].

## 8.6 Summary

Using mesoscale computer simulations, we designed a phagocyte-inspired active microcapsule that is capable of selectively capturing nanoparticles from external solutions. The microdevice is comprised of a temperature-responsive microgel embedded inside a perforated rigid shell. The radius of the perforations determines the amount of gel that exits the microcapsule interior during swelling. The radius of the perforations is also important for defining the minimum microgel size that can be used in the device. If the perforations are larger than the collapsed microgel size, the microgel could leave the porous shell when

it is in the collapsed state. To gate solute access to the capsule interior, we incorporated a polymer brush with mutually sticky end groups, which is attached at the shell perforations. The length of the brush chains is roughly 40% longer than the radius of the perforations to enable pore closure. We showed that, upon stimulus application, the microgel increases in volume, imposing pressure on the polymer brush. Once the pressure is sufficiently large, the polymer brush yields and the gel extrudes through the perforations, making contact with the external solvent. Removal of the external stimulus causes the gel to retreat back into the shell, allowing the brush to seal the shell pores. We showed that periodic applications of the external stimulus enhance nanoparticle transfer into the capsule interior via advective transport, leading to the optimum actuation. We also showed that nanoparticle capture depends on nanoparticle-microgel interactions which can be used to tune the microdevice to pick and isolate specific nanoparticles from a nanoparticle mixture.

The measurement of physiological biomarkers, like blood pressure and body temperature, have been critical diagnostic tools over the last 100 years. A much anticipated benefit of the recent advancements in nanotechnology is the ability to easily detect molecular biomarkers like proteins, antigens, and small molecules within the human body [224, 225]. The continuous in vivo tracking of such molecular biomarkers via an active microcapsule, like the one designed here, can unlock a multitude of new diagnostic strategies, making the development of more personalized treatment therapies possible [200]. In addition to biomedical applications, synthetic phagocyte-like microdevices can also have a strong impact on diverse research areas ranging from origin of life studies to pollutant clean up, making it a promising direction for future research. Just recently, researchers have demonstrated phagocytosis-like behavior in water droplets inside a

magnetic Pickering emulsion by varying oleic acid concentrations in the emulsion and inducing an opening in the magnetic nanoparticle shell [201]. Similar biocompatible hydrogel-based devices would be able to immobilize enzymes and catalyst-containing nanoparticles, which could allow various chemical reactions to occur within the microdevice, serving as an essential element in the development of an artificial cell [205, 226]. Synthetic devices, like the active microcapsule reported here, could then be used to understand cooperative and social behavior of communities of artificial cells [227].

# CONCLUDING REMARKS AND FUTURE DIRECTION

In our work we leverage mesoscale computational techniques to gauge both static and dynamic properties of microgel-based soft matter systems. In Chapters 2-4 the properties of individual spherical microgel particles, and the constituent polymer chains were examined. To model high porosity microgels we demonstrated that polymer chains with a nonzero bending stiffness are ideal. Care must be taken however to ensure fully flexible behavior is maintained. In the current study Flory's theory was utilized to gauge the chain flexibility. Polymer networks were created by distributing crosslinking sites throughout the computational domain using either a random or Gaussian distribution. We showed that as the average chain length in the polymer network increases the volume phase transition becomes sharper near the critical point, which is consistent with experiments. For large porosities and smaller microgel sizes, we demonstrated that the bundling of polymer chains speeds up the collapse of the network. In these cases, the kinetics are in good agreement with Tanaka's theory. Increases in the microgel size and decreases in the network porosity can both however lead to kinetic arrest during deswelling. This can significantly extend the timescale for deswelling and cause deviations from Tanaka's theory.

For high aspect ratio toroidal microgels we demonstrated that the formation of the dehydrated skin layer, which occurs as a result of a rapid change in the solvency, can lead to large out-of-plane deformations during deswelling. Meanwhile, for quasistatic deswelling no out-of-plane deformations are observed and the aspect ratio of the toroids is maintained throughout the deswelling process. In the future we anticipate utilizing our

mesoscale microgel model to better characterize local changes in skin layer growth near geometrical features like corners, edges, and high/low curvature regions. This could help facilitate the design of future microdevices. The dehydrated skin layer could also be used for micro-compartmentalization which can pave the way to designing novel biomimetic materials. The ability to swell/deswell and buckle out-of-plane also makes toroidal microgels ideal for micro-sensing applications.

To probe how the bulk modulus $K$ of spherical microgel particles changes at different solvent conditions we varied the osmotic pressure and monitored the corresponding changes in the network volume and pressure. Fitting the bulk moduli data to Flory-Rehner's theory established a connection between the network-solvent repulsion coefficient $a$ in the DPD model and the Flory-Huggins solvency parameter $\chi$. To measure the Young's modulus $E$, a spherical microgel particle was compressed quasistatically between two plates, as the change in deformation with applied load was tracked. The mechanical results indicated good agreement with both poroelastic and Flory-Rehner theory, signifying that the DPD model can capture not only the microgel kinetics but mechanics as well. In the future we aim to incorporate into our model the cooperative-hydration concepts put forth by Kojima *et al.* This should allow us to capture the dip in the bulk modulus and the corresponding negative Poisson ratios which are observed near the critical point for some microgels. Additionally, we plan on adding ionic interactions into the model which will enable us to study polyelectrolyte microgels.

After characterizing the single particle properties, we examined how the mechanical and rheological responses of microgel suspensions vary at different packing fractions and solvencies. At high packing fractions deformation was found to occur mainly

as a result of particles shrinking. This is true regardless of the solvency of the suspension. It was also found that the suspension rheology and mechanics are defined by the single particle modulus, which sets the scale for shrinking. For the loss and storage moduli it was found that regardless of the solvent conditions or packing fraction all data can be scaled onto two master curves, when normalizing by the crossover frequency and storage modulus. The crossover frequency and storage modulus ($\omega_{crossover}$ and $G'_{crossover}$) are both minimized near the critical point for the solvency method. Meanwhile, for the volumetric method $\omega_{crossover}$ and $G'_{crossover}$ monotonically increase with packing fraction. Future work is aimed at examining how different network parameters impact the suspension rheology. Moreover, we plan on studying the impact of polydispersity on microgel mechanics. The ultimate goal is to couple computational and experimental data into a machine learning algorithm which will facilitate the discovery of novel soft materials.

In the last 3 chapters we introduce three novel hydrogel-based microdevices: self-folding microsheets, a self-propelling bi-layered microswimmer, and a biomimetic microcapsule. The self-folding microsheets were comprised of a trilayered spider-silk composite. Changes in the pH swelled the responsive silk ionomer layer, generating stresses in both the polystyrene (PS) and $\beta$-sheet layers. We showed that for thinner PS layers folding always occurs on the $\beta$-sheet side, which is stiffer. Varying the aspect ratios of the microsheets we illustrated that the folding patterns observed in our lattice spring model (LSM) are in good agreement with experimental observations. Stress analysis of each microsheet illustrated how folding is initiated in each composite structure. A modified version of Timoshenko's beam theory was employed to study the final self-rolled radius of

the composite spider-silk structures, as a function of the thickness of individual layers. The calculated tube radii were shown to be in good agreement with experimentally measured values.

The microswimmer design which was introduced consists of two hydrogel layers which have identical material properties but have different responses to environmental stimuli. When exposed to an appropriate external stimulus one of the polymeric layers swells/deswells while the other layer remains passive. We demonstrated that by cycling the external stimulus on/off in a periodic fashion self-propulsion in a low Reynolds number environment could be achieved. The generation of time-irreversible motion was shown to arise from the timescale mismatch between de/swelling and bending. The optimal microswimmer velocity was shown to occur for a passive layer which is approximately 1.4 times thicker than the active layer. Future work is focused on examining the collective behavior of large groups of microswimmers. Such systems could be easily leveraged for on-demand micromixing and more complex microtasks like cargo transport.

The active microcapsule, which was introduced consisted of an active spherical microgel, a perforated spherical shell, and a copolymer brush with sticky end groups. In the collapsed state the microgel sits inside the perforated spherical shell, as the polymer brush closes each of the openings in the shell. Upon swelling, the microgel rapidly fills the internal volume of the shell and slowly pushes the polymer brush open as it makes contact with the external solvent. We demonstrated that the active microcapsule accumulates adhesive nanoparticles into the internal volume at predefined rates. The capture rate of the microdevice was shown to vary in a non-monotonic fashion with the length of the actuation period. Capture rates were maximized for actuation periods which are 3-10 times larger

than the characteristic swelling time of the microgel. Active microcapsules, such as the one introduced here, can be used for oil recovery. In addition, such microcapsules are good primitive cell models. Large suspensions of active microcapsules can thus potentially be used to study the formation of multicellular organisms.

The results of our studies indicate that DPD is an excellent method for simulating the behavior of microgels and soft-matter systems. One major benefit of the current computational approach is that any polymer network topology can be easily studied. The close relation between DPD and molecular dynamics makes the inclusion of ionic interactions and hydrogen bonding possible. In the context of larger systems, like microgel suspensions, the incorporation of machine learning algorithms in future work is critical as it can strengthen the link between simulations and experiments.

# SCIENTIFIC CONTRIBUTIONS

One of the major scientific contributions of this work is the development of a mechanically and kinetically compliant mesoscale microgel model. This model offers a direct connection between the network-solvent repulsion coefficient and the Flory-Huggins interaction parameter. An important feature of our model is the ability to evaluate skin layer growth during rapid deswelling. Experimentally, it is difficult to gauge how the thickness of the skin layer changes with time and the corresponding impact on solvent outflow [54]. As shown in Chapter 3, the model presented here offers a direct way of quantifying these properties.

Another significant contribution of the current work is that for microgel suspensions we illustrate how microgel-microgel interpenetration and microgel surface area to volume ratios vary with changes in the generalized packing fraction. Such measurements experimentally are difficult to make. Our simulations fill this gap, showing that microgel interpenetration in highly compressed states is roughly 20-25% of the crosslink distance. Interestingly, we find that this is true regardless of the microgel network structure. In bad solvent conditions microgel particles with normal crosslink distributions have higher surface area to volume ratios, indicating higher deformation. These findings can be utilized to generate novel soft materials and structures.

Three additional, notable, scientific contributions are also included in Chapters 6-8. In the self-folding composite study, we illustrate how active 2D geometries could be exploited to create different 3D structures, like rings and microtubules. In the microswimmer study we demonstrate how the timescale mismatch between bending and

de/swelling can be exploited to create propulsion in a low Reynolds number environment. Lastly, in Chapter 8 we show how the large volume changes of microgels could be leveraged to selectively capture nanoparticles from an external solvent at predefined rates.

# REFERENCES


1. Chang, Y.-W., et al., *Extreme thermodynamics with polymer gel tori: Harnessing thermodynamic instabilities to induce large-scale deformations.* Physical Review E, 2018. **98**(2): p. 020501.

2. Filipcsei, G., J. Feher, and M. Zrınyi, *Electric field sensitive neutral polymer gels.* Journal of Molecular Structure, 2000. **554**(1): p. 109-117.

3. Ahn, S.-k., et al., *Stimuli-responsive polymer gels.* Soft Matter, 2008. **4**(6): p. 1151-1157.

4. Roy, D., J.N. Cambre, and B.S. Sumerlin, *Future perspectives and recent advances in stimuli-responsive materials.* Progress in Polymer Science, 2010. **35**(1-2): p. 278-301.

5. Zrinyi, M., *Intelligent polymer gels controlled by magnetic fields.* Colloid and Polymer Science, 2000. **278**(2): p. 98-103.

6. Shibayama, M. and T. Tanaka, *Volume phase transition and related phenomena of polymer gels,* in *Responsive gels: volume transitions I*. 1993, Springer. p. 1-62.

7. Hirotsu, S., Y. Hirokawa, and T. Tanaka, *Volume-phase transitions of ionized N-isopropylacrylamide gels.* The Journal of chemical physics, 1987. **87**(2): p. 1392-1395.

8. Tanaka, T., et al., *Critical kinetics of volume phase transition of gels.* Physical Review Letters, 1985. **55**(22): p. 2455.

9. Tanaka, T. and D.J. Fillmore, *Kinetics of swelling of gels.* The Journal of Chemical Physics, 1979. **70**(3): p. 1214-1218.

10. Hirotsu, S., *Static and time-dependent properties of polymer gels around the volume phase transition.* Phase Transitions: A Multinational Journal, 1994. **47**(3-4): p. 183-240.

11. Hirotsu, S., *Coexistence of phases and the nature of first-order phase transition in poly-N-isopropylacrylamide gels.* Responsive Gels: Volume Transitions II, 1993: p. 1-26.

12. Hirotsu, S., *Softening of bulk modulus and negative Poisson's ratio near the volume phase transition of polymer gels.* The Journal of chemical physics, 1991. **94**(5): p. 3949-3957.

13. Sierra-Martin, B., et al., *Bulk modulus of poly (N-isopropylacrylamide) microgels through the swelling transition.* Physical Review E, 2011. **84**(1): p. 011406.

14. Lopez-Leon, T. and A. Fernandez-Nieves, *Macroscopically probing the entropic influence of ions: Deswelling neutral microgels with salt.* Physical Review E, 2007. **75**(1): p. 011801.

15. Fernández-Barbero, A., et al., *Structural modifications in the swelling of inhomogeneous microgels by light and neutron scattering.* Physical Review E, 2002. **66**(5): p. 051803.

16. Wu, S., et al., *Nanofiber-structured hydrogel yarns with pH-response capacity and cardiomyocyte-drivability for bio-microactuator application.* Acta Biomaterialia, 2017.

17. Ye, C., et al., *Self-(Un)rolling Biopolymer Microstructures: Rings, Tubules, and Helical Tubules from the Same Material.* Angewandte Chemie International Edition, 2015. **54**(29): p. 8490-8493.

18. Ye, C., et al., *Bimorph Silk Microsheets with Programmable Actuating Behavior: Experimental Analysis and Computer Simulations.* ACS Applied Materials & Interfaces, 2016. **8**(27): p. 17694-17706.

19. Ren, C.D., et al., *Liposomal delivery of horseradish peroxidase for thermally triggered injectable hyaluronic acid–tyramine hydrogel scaffolds.* Journal of Materials Chemistry B, 2015. **3**(23): p. 4663-4670.

20. Puppi, D., et al., *Polymeric materials for bone and cartilage repair.* Progress in Polymer Science, 2010. **35**(4): p. 403-440.

21. Seol, D., et al., *Biocompatibility and preclinical feasibility tests of a temperature-sensitive hydrogel for the purpose of surgical wound pain control and cartilage repair.* Journal of Biomedical Materials Research Part B: Applied Biomaterials, 2013. **101**(8): p. 1508-1515.

22. Muzzarelli, R.A., et al., *Chitosan, hyaluronan and chondroitin sulfate in tissue engineering for cartilage regeneration: a review.* Carbohydrate Polymers, 2012. **89**(3): p. 723-739.

23. Walker, K.J. and S.V. Madihally, *Anisotropic temperature sensitive chitosan-based injectable hydrogels mimicking cartilage matrix.* Journal of Biomedical Materials Research Part B: Applied Biomaterials, 2015. **103**(6): p. 1149-1160.

24. Cho, E.C., et al., *Highly responsive hydrogel scaffolds formed by three-dimensional organization of microgel nanoparticles.* Nano letters, 2008. **8**(1): p. 168-172.

25. Li, Z., et al., *Injectable polysaccharide hydrogels as biocompatible platforms for localized and sustained delivery of antibiotics for preventing local infections.* Macromolecular bioscience, 2017. **17**(4).

26. Kurisawa, M., et al., *Methods for producing crosslinked flavonoid hydrogels*. 2016, Google Patents.

27. Ying, J.Y., J.E. Chung, and M. Kurisawa, *Method of delivering an anti-cancer agent to a cell*. 2016, Google Patents.

28. Kurisawa, M., et al., *Anti-cancer agent delivery vehicles capable of improved loading*. 2017, Google Patents.

29. Dubey, N.C., et al., *Bienzymatic sequential reaction on microgel particles and their cofactor dependent applications.* Biomacromolecules, 2016. **17**(5): p. 1610-1620.

30. Biswas, A., et al., *Composite hydrogels containing bioactive microreactors for optical enzymatic lactate sensing.* ACS sensors, 2017. **2**(11): p. 1584-1588.

31. Chaudhuri, O., et al., *Hydrogels with tunable stress relaxation regulate stem cell fate and activity.* Nature materials, 2016. **15**(3): p. 326.

32. Shin, S.R., et al., *Carbon nanotube reinforced hybrid microgels as scaffold materials for cell encapsulation.* ACS nano, 2011. **6**(1): p. 362-372.

33. Kim, M.Y. and J. Kim, *Chitosan Microgels Embedded with Catalase Nanozyme-Loaded Mesocellular Silica Foam for Glucose-Responsive Drug Delivery.* ACS Biomaterials Science & Engineering, 2017. **3**(4): p. 572-578.

34. Utech, S., et al., *Microfluidic generation of monodisperse, structurally homogeneous alginate microgels for cell encapsulation and 3D cell culture.* Advanced healthcare materials, 2015. **4**(11): p. 1628-1633.

35. Hardin, J.O., et al., *Altering Colloidal Surface Functionalization Using DNA Encapsulated Inside Monodisperse Gelatin Microsphere Templates.* Langmuir, 2013. **29**(18): p. 5534-5539.

36. Brown, A.C., et al., *Ultrasoft microgels displaying emergent platelet-like behaviours.* Nat Mater, 2014. **13**(12): p. 1108-1114.

37. Douglas, A.M., et al., *Dynamic assembly of ultrasoft colloidal networks enables cell invasion within restrictive fibrillar polymers.* Proceedings of the National Academy of Sciences, 2017. **114**(5): p. 885-890.

38. Vikram Singh, A. and M. Sitti, *Targeted drug delivery and imaging using mobile milli/microrobots: A promising future towards theranostic pharmaceutical design.* Current pharmaceutical design, 2016. **22**(11): p. 1418-1428.

39. Nikolov, S.V., P.D. Yeh, and A. Alexeev, *Self-Propelled Microswimmer Actuated by Stimuli-Sensitive Bilayered Hydrogel.* ACS Macro Letters, 2015. **4**(1): p. 84-88.

40. Masoud, H., B.I. Bingham, and A. Alexeev, *Designing maneuverable micro-swimmers actuated by responsive gel.* Soft Matter, 2012. **8**(34): p. 8944-8951.

41. Ren, C.D., et al., *Cartilage synthesis in hyaluronic acid–tyramine constructs.* Journal of Materials Chemistry B, 2015. **3**(9): p. 1942-1956.

42. Kaderli, S., et al., *Efficacy study of two novel hyaluronic acid-based formulations for viscosupplementation therapy in an early osteoarthrosic rabbit model.* European Journal of Pharmaceutics and Biopharmaceutics, 2015. **96**: p. 388-395.

43. Park, H. and K.Y. Lee, *Cartilage regeneration using biodegradable oxidized alginate/hyaluronate hydrogels.* Journal of Biomedical Materials Research Part A, 2014. **102**(12): p. 4519-4525.

44. Kim, J., et al., *TGF-β1 conjugated chitosan collagen hydrogels induce chondrogenic differentiation of human synovium-derived stem cells.* Journal of biological engineering, 2015. **9**(1): p. 1.

45. Shibayama, M., M. Morimoto, and S. Nomura, *Phase separation induced mechanical transition of poly (N-isopropylacrylamide) water isochore gels.* Macromolecules, 1994. **27**(18): p. 5060-5066.

46. Shibayama, M., et al., *Simple scaling rules on swollen and shrunken polymer gels.* Macromolecules, 1997. **30**(23): p. 7307-7312.

47. Shibayama, M. and K. Nagai, *Shrinking kinetics of poly (N-isopropylacrylamide) gels T-jumped across their volume phase transition temperatures.* Macromolecules, 1999. **32**(22): p. 7461-7468.

48. Deshmukh, S., D.A. Mooney, and J.M.D. MacElroy, *Molecular simulation study of the effect of cross-linker on the properties of poly(N-isopropyl acrylamide) hydrogel.* Molecular Simulation, 2011. **37**(10): p. 846-854.

49. Groot, R.D. and K.L. Rabone, *Mesoscopic simulation of cell membrane damage, morphology change and rupture by nonionic surfactants.* Biophysical Journal, 2001. **81**(2): p. 725-736.

50. Kang, M.K. and R. Huang, *A variational approach and finite element implementation for swelling of polymeric hydrogels under geometric constraints.* Journal of Applied Mechanics, 2010. **77**(6): p. 061004.

51. Mills, Z.G., W. Mao, and A. Alexeev, *Mesoscale modeling: solving complex flows in biology and biotechnology.* Trends in biotechnology, 2013. **31**(7): p. 426-434.

52. Yeh, P.D. and A. Alexeev, *Mesoscale modelling of environmentally responsive hydrogels: emerging applications.* Chemical Communications, 2015. **51**(50): p. 10083-10095.

53. Español, P. and P.B. Warren, *Perspective: Dissipative particle dynamics.* The Journal of Chemical Physics, 2017. **146**(15): p. 150901.

54. Dimitriyev, M.S., et al., *Swelling thermodynamics and phase transitions of polymer gels.* Nano Futures, 2019. **3**(4): p. 042001.

55. Yoshida, R., et al., *Comb-type grafted hydrogels with rapid deswelling response to temperature changes.* Nature, 1995. **374**(6519): p. 240-242.

56. Wrede, O., et al., *Volume phase transition kinetics of smart N-n-propylacrylamide microgels studied by time-resolved pressure jump small angle neutron scattering.* Scientific Reports, 2018. **8**(1): p. 13781.

57. Wu, X.S., A.S. Hoffman, and P. Yager, *Synthesis and characterization of thermally reversible macroporous poly (N-isopropylacrylamide) hydrogels.* Journal of Polymer Science Part A: Polymer Chemistry, 1992. **30**(10): p. 2121-2129.

58. Sierra-Martin, B. and A. Fernandez-Nieves, *Phase and non-equilibrium behaviour of microgel suspensions as a function of particle stiffness.* Soft Matter, 2012. **8**(15): p. 4141-4150.

59. Liétor-Santos, J.J., B. Sierra-Martín, and A. Fernández-Nieves, *Bulk and shear moduli of compressed microgel suspensions.* Physical Review E, 2011. **84**(6): p. 060402.

60. Pelaez-Fernandez, M., et al., *Impact of single-particle compressibility on the fluid-solid phase transition for ionic microgel suspensions.* Physical review letters, 2015. **114**(9): p. 098303.

61. Fernandez-Nieves, A., et al., *Microgel suspensions: fundamentals and applications*. 2011: John Wiley & Sons.

62. Kojima, H. and F. Tanaka, *Cooperative hydration induces discontinuous volume phase transition of cross-linked poly (N-isopropylacrylamide) gels in water.* Macromolecules, 2010. **43**(11): p. 5103-5113.

63. Gnan, N., et al., *In Silico Synthesis of Microgel Particles.* Macromolecules, 2017. **50**(21): p. 8777-8786.

64. Gavrilov, A., A. Chertovich, and E.Y. Kramarenko, *Dissipative particle dynamics for systems with high density of charges: Implementation of electrostatic interactions.* The Journal of chemical physics, 2016. **145**(17): p. 174101.

65. Gavrilov, A.A., A.V. Chertovich, and E.Y. Kramarenko, *Conformational Behavior of a Single Polyelectrolyte Chain with Bulky Counterions.* Macromolecules, 2016. **49**(3): p. 1103-1110.

66. Rumyantsev, A.M., A.A. Rudov, and I.I. Potemkin, *Communication: Intraparticle segregation of structurally homogeneous polyelectrolyte microgels caused by long-range Coulomb repulsion*. 2015, AIP Publishing.

67. Schmid, A.J., et al., *Multi-shell hollow nanogels with responsive shell permeability.* Scientific Reports, 2016. **6**: p. 22736.

68. Yashin, V.V., O. Kuksenok, and A.C. Balazs, *Modeling autonomously oscillating chemo-responsive gels.* Progress in Polymer Science, 2010. **35**(1-2): p. 155-173.

69. He, X., et al., *Synthetic homeostatic materials with chemo-mechano-chemical self-regulation.* Nature, 2012. **487**(7406): p. 214.

70. Groot, R.D. and P.B. Warren, *Dissipative particle dynamics: Bridging the gap between atomistic and mesoscopic simulation.* Journal of Chemical Physics, 1997. **107**(11): p. 4423-4435.

71. Hoogerbrugge, P.J. and J.M.V.A. Koelman, *Simulating Microscopic Hydrodynamic Phenomena with Dissipative Particle Dynamics.* Europhysics Letters, 1992. **19**(3): p. 155-160.

72. Espanol, P. and P. Warren, *Statistical-mechanics of dissipative particle dynamics.* Europhysics Letters, 1995. **30**(4): p. 191-196.

73. Glotzer, S.C. and W. Paul, *Molecular and mesoscale simulation methods for polymer materials.* Annual Review of Materials Research, 2002. **32**: p. 401-436.

74. Chen, S., et al., *Dissipative particle dynamics simulation of polymer drops in a periodic shear flow.* Journal of Non-Newtonian Fluid Mechanics, 2004. **118**(1): p. 65-81.

75. Fedosov, D.A., G.E. Karniadakis, and B. Caswell, *Dissipative particle dynamics simulation of depletion layer and polymer migration in micro- and nanochannels for dilute polymer solutions.* Journal of Chemical Physics, 2008. **128**(14): p. 144903.

76. Spenley, N.A., *Scaling laws for polymers in dissipative particle dynamics.* Europhysics Letters, 2000. **49**(4): p. 534-540.

77. Ripoll, M., M.H. Ernst, and P. Espanol, *Large scale and mesoscopic hydrodynamics for dissipative particle dynamics.* Journal of Chemical Physics, 2001. **115**(15): p. 7271-7284.

78. Lee, M.-T., A. Vishnyakov, and A.V. Neimark, *Modeling proton dissociation and transfer using dissipative particle dynamics simulation.* Journal of chemical theory and computation, 2015. **11**(9): p. 4395-4403.

79. Li, N.K., et al., *Salt Responsive Morphologies of ssDNA-Based Triblock Polyelectrolytes in Semi-Dilute Regime: Effect of Volume Fractions and Polyelectrolyte Length.* Macromolecular Rapid Communications, 2017.

80. Groot, R.D., *Electrostatic interactions in dissipative particle dynamics-simulation of polyelectrolytes and anionic surfactants.* Journal of Chemical Physics, 2003. **118**(24): p. 11265-11277.

81. Ibergay, C., P. Malfreyt, and D.J. Tildesley, *Electrostatic Interactions in Dissipative Particle Dynamics: Toward a Mesoscale Modeling of the Polyelectrolyte Brushes.* Journal of Chemical Theory and Computation, 2009. **5**(12): p. 3245-3259.

82. Boek, E.S., et al., *Simulating the rheology of dense colloidal suspensions using dissipative particle dynamics.* Physical Review E, 1997. **55**(3): p. 3124-3133.

83. Symeonidis, V., G.E. Karniadakis, and B. Caswell, *Dissipative particle dynamics simulations of polymer chains: Scaling laws and shearing response compared to DNA experiments.* Physical Review Letters, 2005. **95**(7): p. 076001.

84. Ganzenmuller, G.C., S. Hiermaier, and M.O. Steinhauser, *Shock-wave induced damage in lipid bilayers: a dissipative particle dynamics simulation study.* Soft Matter, 2011. **7**(9): p. 4307-4317.

85. Xiaolei Chu, F.A. and M. Dutt, *Modeling Interactions between Multicomponent Vesicles and Antimicrobial Peptide-Inspired Nanoparticles.* ACS Nano, 2016. **10**(8): p. 7351 - 7361.

86. Pivkin, I.V., et al., *Biomechanics of red blood cells in human spleen and consequences for physiology and disease.* Proceedings of the National Academy of Sciences of the United States of America, 2017. **114**(22): p. E4521-E4521.

87. Masoud, H. and A. Alexeev, *Permeability and diffusion through mechanically deformed random polymer networks.* Macromolecules, 2010. **43**(23): p. 10117-10122.

88. Masoud, H. and A. Alexeev, *Controlled Release of Nanoparticles and Macromolecules from Responsive Microgel Capsules.* Acs Nano, 2012. **6**(1): p. 212-219.

89. Sirk, T.W., et al., *An enhanced entangled polymer model for dissipative particle dynamics.* Journal of Chemical Physics, 2012. **136**(13): p. 134903.

90. Tarjan, R., *Depth-first search and linear graph algorithms.* SIAM journal on computing, 1972. **1**(2): p. 146-160.

91. Senff, H. and W. Richtering, *Influence of cross-link density on rheological properties of temperature-sensitive microgel suspensions.* Colloid and Polymer Science, 2000. **278**(9): p. 830-840.

92. De Gennes, P.-G., *Scaling concepts in polymer physics*. 1979: Cornell university press.

93. Annabi, N., et al., *Controlling the porosity and microarchitecture of hydrogels for tissue engineering.* Tissue Engineering Part B: Reviews, 2010. **16**(4): p. 371-383.

94. Stukowski, A., *Visualization and analysis of atomistic simulation data with OVITO–the Open Visualization Tool.* Modelling and Simulation in Materials Science and Engineering, 2009. **18**(1): p. 015012.

95. Liu, P., et al., *Drug release kinetics from monolayer films of glucose-sensitive microgel.* Polymer, 2010. **51**(12): p. 2668-2675.

96. Pjanović, R., et al., *Diffusion of drugs from hydrogels and liposomes as drug carriers.* Journal of Chemical Technology & Biotechnology, 2010. **85**(5): p. 693-698.

97. Missirlis, D., et al., *Doxorubicin encapsulation and diffusional release from stable, polymeric, hydrogel nanoparticles.* European journal of pharmaceutical sciences, 2006. **29**(2): p. 120-129.

98. Kabanov, A.V. and V.Y. Alakhov, *Pluronic® block copolymers in drug delivery: From micellar nanocontainers to biological response modifiers.* Critical Reviews™ in Therapeutic Drug Carrier Systems, 2002. **19**(1).

99. Lustig, S.R. and N.A. Peppas, *Solute diffusion in swollen membranes. IX. Scaling laws for solute diffusion in gels.* Journal of Applied Polymer Science, 1988. **36**(4): p. 735-747.

100. Vinogradov, S.V., *Colloidal microgels in drug delivery applications.* Current pharmaceutical design, 2006. **12**(36): p. 4703-4712.

101. Oh, J.K., et al., *The development of microgels/nanogels for drug delivery applications.* Progress in Polymer Science, 2008. **33**(4): p. 448-477.

102. Lynch, I. and K.A. Dawson, *Release of model compounds from "plum-pudding"-type gels composed of microgel particles randomly dispersed in a gel matrix.* The Journal of Physical Chemistry B, 2004. **108**(30): p. 10893-10898.

103. Wang, Q., et al., *Thermosensitive phase behavior and drug release of in situ gelable poly (N-isopropylacrylamide-co-acrylamide) microgels.* Colloid and Polymer Science, 2007. **285**(5): p. 515-521.

104. Dušková-Smrčková, M. and K. Dušek, *How to Force Polymer Gels to Show Volume Phase Transitions.* ACS Macro Letters, 2019. **8**(3): p. 272-278.

105. Zhao, J., et al., *Localized Nanoscale Heating Leads to Ultrafast Hydrogel Volume-Phase Transition.* ACS nano, 2018. **13**(1): p. 515-525.

106. Wang, K., et al., *Chitosan-gelatin-based microgel for sustained drug delivery.* Journal of Biomaterials science, Polymer edition, 2016. **27**(5): p. 441-453.

107. Suarez, I.J., A. Fernandez-Nieves, and M. Marquez, *Swelling kinetics of poly (N-isopropylacrylamide) minigels.* The Journal of Physical Chemistry B, 2006. **110**(51): p. 25729-25733.

108. Geissler, E., H.B. Bohidar, and A.M. Hecht, *Collective diffusion in semi-dilute gels at the. THETA. temperature.* Macromolecules, 1985. **18**(5): p. 949-953.

109. Shibayama, M., M. Morimoto, and S. Nomura, *Phase separation induced mechanical transition of poly (N-isopropylacrylamide)/water isochore gels.* Macromolecules, 1994. **27**(18): p. 5060-5066.

110. Patil, N., et al., *Swelling-induced optical anisotropy of thermoresponsive hydrogels based on poly (2-(2-methoxyethoxy) ethyl methacrylate): Deswelling kinetics probed by quantitative Mueller matrix polarimetry.* The Journal of Physical Chemistry B, 2012. **116**(47): p. 13913-13921.

111. Koyama, T. and H. Tanaka, *Volume-shrinking kinetics of transient gels as a consequence of dynamic interplay between phase separation and mechanical relaxation.* Physical Review E, 2018. **98**(6): p. 062617.

112. Gao, D., et al., *Ultrafine hydrogel nanoparticles: synthetic approach and therapeutic application in living cells.* Angewandte Chemie International Edition, 2007. **46**(13): p. 2224-2227.

113. Acciaro, R., T. Gilanyi, and I. Varga, *Preparation of monodisperse poly (N-isopropylacrylamide) microgel particles with homogenous cross-link density distribution.* Langmuir, 2011. **27**(12): p. 7917-7925.

114. Lyon, L.A. and A. Fernandez-Nieves, *The polymer/colloid duality of microgel suspensions.* Annual review of physical chemistry, 2012. **63**: p. 25-43.

115. Sliozberg, Y.R., et al., *Modeling viscoelastic properties of triblock copolymers: a dpd simulation study.* Journal of Polymer Science part B: polymer physics, 2010. **48**(1): p. 15-25.

116. Zhao, J., et al., *Size-dependent mechanical behavior of nanoscale polymer particles through coarse-grained molecular dynamics simulation.* Nanoscale research letters, 2013. **8**(1): p. 541.

117. Valentini, P., W. Gerberich, and T. Dumitrică, *Phase-transition plasticity response in uniaxially compressed silicon nanospheres.* Physical review letters, 2007. **99**(17): p. 175701.

118. Gasser, U. and A. Fernandez-Nieves, *Crystal structure of highly concentrated, ionic microgel suspensions studied by small-angle x-ray scattering.* Physical Review E, 2010. **81**(5): p. 052401.

119. Romeo, G., et al., *Origin of de-swelling and dynamics of dense ionic microgel suspensions.* The Journal of chemical physics, 2012. **136**(12): p. 124905.

120. Nikolov, S., A. Fernandez-Nieves, and A. Alexeev, *Mesoscale modeling of microgel mechanics and kinetics through the swelling transition.* Applied Mathematics and Mechanics, 2018. **39**(1): p. 47-62.

121. Omari, A., et al., *Soft water-soluble microgel dispersions: Structure and rheology*. Journal of colloid and interface science, 2006. **302**(2): p. 537-546.

122. Burmistrova, A., et al., *The effect of co-monomer content on the swelling/shrinking and mechanical behaviour of individually adsorbed PNIPAM microgel particles.* Polymers, 2011. **3**(4): p. 1575-1590.

123. Fernández-Nieves, A., et al., *Charge controlled swelling of microgel particles.* Macromolecules, 2000. **33**(6): p. 2114-2118.

124. Kratz, K., T. Hellweg, and W. Eimer, *Structural changes in PNIPAM microgel particles as seen by SANS, DLS, and EM techniques.* Polymer, 2001. **42**(15): p. 6631-6639.

125. Trappe, V. and D. Weitz, *Scaling of the viscoelasticity of weakly attractive particles.* Physical review letters, 2000. **85**(2): p. 449.

126. Gasser, U., et al., *Form factor of pNIPAM microgels in overpacked states.* The Journal of chemical physics, 2014. **141**(3): p. 034901.

127. Plimpton, S., *Fast parallel algorithms for short-range molecular dynamics.* Journal of computational physics, 1995. **117**(1): p. 1-19.

128. Heyes, D. and A. Brańka, *Interactions between microgel particles.* Soft Matter, 2009. **5**(14): p. 2681-2685.

129. Ahrens, J., B. Geveci, and C. Law, *Paraview: An end-user tool for large data visualization.* The visualization handbook, 2005. **717**.

130. Ayachit, U., *The paraview guide: a parallel visualization application*. 2015: Kitware, Inc.

131. Conley, G.M., et al., *Jamming and overpacking fuzzy microgels: Deformation, interpenetration, and compression.* Science advances, 2017. **3**(10): p. e1700969.

132. Romeo, G., et al., *Temperature-Controlled Transitions Between Glass, Liquid, and Gel States in Dense p-NIPA Suspensions.* Advanced Materials, 2010. **22**(31): p. 3441-3445.

133. Jaishankar, A. and G.H. McKinley, *Power-law rheology in the bulk and at the interface: quasi-properties and fractional constitutive equations.* Proceedings of the Royal Society A: Mathematical, Physical and Engineering Sciences, 2013. **469**(2149): p. 20120284.

134. Morse, D.C., *Viscoelasticity of tightly entangled solutions of semiflexible polymers.* Physical Review E, 1998. **58**(2): p. R1237.

135. Fusco, S., et al., *An integrated microrobotic platform for on-demand, targeted therapeutic interventions.* Advanced Materials, 2014. **26**(6): p. 952-957.

136. Huang, T.Y., et al., *3D printed microtransporters: Compound micromachines for spatiotemporally controlled delivery of therapeutic agents.* Advanced Materials, 2015. **27**(42): p. 6644-6650.

137. Gómez, S., et al., *Design and properties of 3D scaffolds for bone tissue engineering.* Acta biomaterialia, 2016. **42**: p. 341-350.

138. Pecci, R., et al., *3D printed scaffolds with random microarchitecture for bone tissue engineering applications: Manufacturing and characterization.* Journal of the Mechanical Behavior of Biomedical Materials, 2020. **103**: p. 103583.

139. Gu, Z., et al., *Glucose-responsive microgels integrated with enzyme nanocapsules for closed-loop insulin delivery.* ACS nano, 2013. **7**(8): p. 6758-6766.

140. Rizvi, S.B., et al., *Semiconductor quantum dots as fluorescent probes for in vitro and in vivo bio-molecular and cellular imaging.* Nano reviews, 2010. **1**(1): p. 5161.

141. Serban, M.A., et al., *Modular elastic patches: Mechanical and biological effects.* Biomacromolecules, 2010. **11**(9): p. 2230-2237.

142. Ye, C., et al., *Robust and responsive silk ionomer microcapsules.* Biomacromolecules, 2011. **12**(12): p. 4319-4325.

143. Vollrath, F. and D.P. Knight, *Liquid crystalline spinning of spider silk.* Nature, 2001. **410**(6828): p. 541-548.

144. Buxton, G.A. and A.C. Balazs, *Lattice spring model of filled polymers and nanocomposites.* The Journal of chemical physics, 2002. **117**(16): p. 7649-7658.

145. Buxton, G.A., C.M. Care, and D.J. Cleaver, *A lattice spring model of heterogeneous materials with plasticity.* Modelling and simulation in materials science and engineering, 2001. **9**(6): p. 485.

146. Zhao, G.F., J. Fang, and J. Zhao, *A 3D distinct lattice spring model for elasticity and dynamic failure.* International Journal for Numerical and Analytical Methods in Geomechanics, 2011. **35**(8): p. 859-885.

147. Mao, W., *Modeling particle suspensions using lattice Boltzmann method*. 2013, Georgia Institute of Technology.

148. Stoychev, G., et al., *Shape-programmed folding of stimuli-responsive polymer bilayers.* ACS nano, 2012. **6**(5): p. 3925-3934.

149. Nayfeh, A.H. and S.R. Baker, *Thermomechanical distortion of composite panels.* Fibre Science and Technology, 1977. **10**(2): p. 139-149.

150. Breger, J.C., et al., *Self-folding thermo-magnetically responsive soft microgrippers.* ACS applied materials & interfaces, 2015. **7**(5): p. 3398-3405.

151. Homberg, B.S., et al. *Haptic identification of objects using a modular soft robotic gripper*. in *2015 IEEE/RSJ International Conference on Intelligent Robots and Systems (IROS)*. 2015. IEEE.

152. Manti, M., et al., *A bioinspired soft robotic gripper for adaptable and effective grasping.* Soft Robotics, 2015. **2**(3): p. 107-116.

153. Gao, W., et al., *Bioinspired Helical Microswimmers Based on Vascular Plants.* Nano Letters, 2014. **14**(1): p. 305-310.

154. Huang, H.-W., et al., *Adaptive locomotion of artificial microswimmers.* Science Advances, 2019. **5**(1): p. eaau1532.

155. Roper, M., et al., *Do magnetic micro-swimmers move like eukaryotic cells?* Proceedings of the Royal Society, Series A: Mathematical, Physical, and Engineering Sciences, 2008. **464**(2092): p. 877-904.

156. Dreyfus, R., et al., *Microscopic artificial swimmers.* Nature, 2005. **437**(7060): p. 862-865.

157. Lin, C.T., et al., *Efficient designs for powering microscale devices with nanoscale biomolecular motors.* Small, 2006. **2**(2): p. 281-287.

158. Wang, J. and W. Gao, *Nano/microscale motors: biomedical opportunities and challenges.* ACS nano, 2012. **6**(7): p. 5745-5751.

159. Hess, H., *Engineering applications of biomolecular motors.* Annual review of biomedical engineering, 2011. **13**: p. 429-450.

160. Geryak, R. and V.V. Tsukruk, *Reconfigurable and actuating structures from soft materials.* Soft matter, 2014. **10**(9): p. 1246-1263.

161. Golestanian, R., T.B. Liverpool, and A. Ajdari, *Designing phoretic micro- and nano-swimmers.* New Journal of Physics, 2007. **9**: p. 126.

162. Ebbens, S.J., et al., *Synthetic running and tumbling: an autonomous navigation strategy for catalytic nanoswimmers.* Soft Matter, 2012. **8**(11): p. 3077-3082.

163. Weibel, D.B., et al., *Microoxen: Microorganisms to move microscale loads.* Proceedings of the National Academy of Sciences of the United States of America, 2005. **102**(34): p. 11963-11967.

164. Zhang, L., et al., *Controlled Propulsion and Cargo Transport of Rotating Nickel Nanowires near a Patterned Solid Surface.* Acs Nano, 2010. **4**(10): p. 6228-6234.

165. Hu, J. and S. Liu, *Responsive polymers for detection and sensing applications: current status and future developments.* Macromolecules, 2010. **43**(20): p. 8315-8330.

166. Döring, A., W. Birnbaum, and D. Kuckling, *Responsive hydrogels–structurally and dimensionally optimized smart frameworks for applications in catalysis, micro-system technology and material science.* Chemical Society Reviews, 2013. **42**(17): p. 7391-7420.

167. Deligkaris, K., et al., *Hydrogel-based devices for biomedical applications.* Sensors and Actuators, B: Chemical, 2010. **147**(2): p. 765-774.

168. Stuart, M.A.C., et al., *Emerging applications of stimuli-responsive polymer materials.* Nature materials, 2010. **9**(2): p. 101-113.

169. Smeets, N. and T. Hoare, *Designing responsive microgels for drug delivery applications.* Journal of Polymer Science, Part A: Polymer Chemistry, 2013. **51**(14): p. 3027-3043.

170. Mano, J.F., *Stimuli-Responsive Polymeric Systems for Biomedical Applications.* Advanced Engineering Materials, 2008. **10**(6): p. 515-527.

171. Yoshida, R. and T. Ueki, *Evolution of self-oscillating polymer gels as autonomous polymer systems.* NPG Asia Materials, 2014. **6**.

172. Yashin, V.V. and A.C. Balazs, *Pattern formation and shape changes in self-oscillating polymer gels.* Science, 2006. **314**(5800): p. 798-801.

173. Morales, D., et al., *Electro-actuated hydrogel walkers with dual responsive legs.* Soft matter, 2014. **10**(9): p. 1337-1348.

174. Osada, Y. and J.P. Gong, *Stimuli-responsive polymer gels and their application to chemomechanical systems.* Progress in Polymer Science, 1993. **18**(2): p. 187-226.

175. Roy, D., J.N. Cambre, and B.S. Sumerlin, *Future perspectives and recent advances in stimuli-responsive materials.* Progress in Polymer Science, 2010. **35**(1): p. 278-301.

176. Filipcsei, G., J. Feher, and M. Zrínyi, *Electric field sensitive neutral polymer gels.* Journal of Molecular Structure, 2000. **554**(1): p. 109-117.

177. Masoud, H. and A. Alexeev, *Controlled release of nanoparticles and macromolecules from responsive microgel capsules.* Acs Nano, 2011. **6**(1): p. 212-219.

178. Chattopadhyay, S., et al., *Swimming efficiency of bacterium Escherichia coli.* Proceedings of the National Academy of Sciences of the United States of America, 2006. **103**(37): p. 13712-13717.

179. Purcell, E.M., *Life at low Reynolds number.* American Journal of Physics, 1977. **45**(1): p. 3-11.

180. Ionov, L., *Hydrogel-based actuators: possibilities and limitations.* Materials Today, 2014: p. DOI: 10.1016/j.mattod.2014.07.002.

181. Ji, M., et al., *Near-Infrared Light-Driven, Highly Efficient Bilayer Actuators Based on Polydopamine-Modified Reduced Graphene Oxide.* Advanced Functional Materials, 2014: p. DOI: 10.1002/adfm.201401011.

182. Li, W., et al., *Fabrication and stimuli-responsive behavior of flexible micro-scrolls.* Soft Matter, 2012. **8**(27): p. 7103-7107.

183. Dai, M., et al., *Humidity-Responsive Bilayer Actuators Based on a Liquid-Crystalline Polymer Network.* ACS applied materials & interfaces, 2013. **5**(11): p. 4945-4950.

184. Wen, H., et al., *Photomechanical bending of linear azobenzene polymer.* RSC Advances, 2014. **4**(23): p. 11776-11781.

185. Maeda, S., et al., *Self-Walking Gel.* Advanced Materials, 2007. **19**(21): p. 3480-3484.

186. Tsukruk, V.V. and A. Alexeev, *Compliant and Reconfigurable Nanocomposites: Fabrication, Testing, and Simulations*, in *2013 MRS Fall Meeting*. 2013: Boston, MA.

187. Krishnaji, S.T., et al., *Thin film assembly of spider silk-like block copolymers.* Langmuir, 2011. **27**(3): p. 1000-1008.

188. Wang, J., *Cargo-towing synthetic nanomachines: Towards active transport in microchip devices.* Lab on a Chip, 2012. **12**(11): p. 1944-1950.

189. Chu, M.K., et al., *In vitro and in vivo testing of glucose-responsive insulin-delivery microdevices in diabetic rats.* Lab on a Chip, 2012. **12**(14): p. 2533-2539.

190. Jonas, O., et al., *An implantable microdevice to perform high-throughput in vivo drug sensitivity testing in tumors.* Science translational medicine, 2015. **7**(284): p. 284ra57-284ra57.

191. Chung, J.E., et al., *Self-assembled micellar nanocomplexes comprising green tea catechin derivatives and protein drugs for cancer therapy.* Nature nanotechnology, 2014. **9**(11): p. 907.

192. Peng, K., et al., *Dextran based photodegradable hydrogels formed via a Michael addition.* Soft Matter, 2011. **7**(10): p. 4881-4887.

193. Molinaro, G., et al., *Biocompatibility of thermosensitive chitosan-based hydrogels: an in vivo experimental approach to injectable biomaterials.* Biomaterials, 2002. **23**(13): p. 2717-2722.

194. Kwag, H.R., et al., *A self-folding hydrogel in vitro model for ductal carcinoma.* Tissue Engineering Part C: Methods, 2016. **22**(4): p. 398-407.

195. Cai, Z., et al., *Photonic crystal protein hydrogel sensor materials enabled by conformationally induced volume phase transition.* Chemical science, 2016. **7**(7): p. 4557-4562.

196. Cai, Z., et al., *Two-dimensional photonic crystal chemical and biomolecular sensors.* Analytical chemistry, 2015. **87**(10): p. 5013-5025.

197. Qiu, Y. and K. Park, *Environment-sensitive hydrogels for drug delivery.* Advanced drug delivery reviews, 2001. **53**(3): p. 321-339.

198. Maya, S., et al., *Smart stimuli sensitive nanogels in cancer drug delivery and imaging: a review.* Current pharmaceutical design, 2013. **19**(41): p. 7203-7218.

199. Garg, T., S. Singh, and A.K. Goyal, *Stimuli-sensitive hydrogels: an excellent carrier for drug and cell delivery.* Critical Reviews™ in Therapeutic Drug Carrier Systems, 2013. **30**(5).

200. Cass, A.E. and S. Sharma, *Microneedle enzyme sensor arrays for continuous in vivo monitoring*, in *Methods in enzymology*. 2017, Elsevier. p. 413-427.

201. Rodríguez-Arco, L., M. Li, and S. Mann, *Phagocytosis-inspired behaviour in synthetic protocell communities of compartmentalized colloidal objects.* Nature materials, 2017. **16**(8): p. 857.

202. Fels, J., S.N. Orlov, and R. Grygorczyk, *The hydrogel nature of mammalian cytoplasm contributes to osmosensing and extracellular pH sensing.* Biophysical journal, 2009. **96**(10): p. 4276-4285.

203. Im, S.H., U. Jeong, and Y. Xia, *Polymer hollow particles with controllable holes in their surfaces.* Nature materials, 2005. **4**(9): p. 671.

204. Haufová, P., et al., *Towards the inkjet fabrication of artificial cells.* Colloids and Surfaces A: Physicochemical and Engineering Aspects, 2012. **410**: p. 52-58.

205. Klouda, L. and A.G. Mikos, *Thermoresponsive hydrogels in biomedical applications.* European journal of pharmaceutics and biopharmaceutics, 2008. **68**(1): p. 34-45.

206. Shukla, S.K., et al., *Chitosan-based nanomaterials: A state-of-the-art review.* International journal of biological macromolecules, 2013. **59**: p. 46-58.

207. Ramos, J., A. Imaz, and J. Forcada, *Temperature-sensitive nanogels: poly (N-vinylcaprolactam) versus poly (N-isopropylacrylamide).* Polymer Chemistry, 2012. **3**(4): p. 852-856.

208. Asaka, K. and H. Okuzaki, *Soft Actuators: Materials, Modeling, Applications, and Future Perspectives*. 2014: Springer.

209. Lunov, O., et al., *Amino-functionalized polystyrene nanoparticles activate the NLRP3 inflammasome in human macrophages.* ACS nano, 2011. **5**(12): p. 9648-9657.

210. Cheah, W.-K., Y.-L. Sim, and F.-Y. Yeoh, *Amine-functionalized mesoporous silica for urea adsorption.* Materials Chemistry and Physics, 2016. **175**: p. 151-157.

211. Schmidt, S.W., et al., *Simple coupling chemistry linking carboxyl-containing organic molecules to silicon oxide surfaces under acidic conditions.* Langmuir, 2010. **26**(19): p. 15333-15338.

212. Takahashi, Y., et al., *Preparation of Hollow Polystyrene Particles and Microcapsules by Radical Polymerization of Janus Droplets Consisting of Hydrocarbon and Fluorocarbon Oils.* JoVE (Journal of Visualized Experiments), 2018(131): p. e56922.

213. Nakaoka, R. and T. Tsuchiya, *Biocompatibility of various kinds of polymer microspheres estimated from their effect on gap junctional intercellular communication of fibroblasts.* Materials Transactions, 2002. **43**(12): p. 3122-3127.

214. Asefa, T. and Z. Tao, *Biocompatibility of mesoporous silica nanoparticles.* Chemical research in toxicology, 2012. **25**(11): p. 2265-2284.

215. Shah, R.K., et al., *Fabrication of monodisperse thermosensitive microgels and gel capsules in microfluidic devices.* Soft Matter, 2008. **4**(12): p. 2303-2309.

216. Pelton, R. *Unresolved issues in the preparation and characterization of thermoresponsive microgels*. in *Macromolecular Symposia*. 2004. Wiley Online Library.

217. Kanai, T., et al., *Preparation of monodisperse PNIPAM gel particles in a microfluidic device fabricated by stereolithography.* Polymer journal, 2011. **43**(12): p. 987.

218. Liu, A.L. and A.J. García, *Methods for generating hydrogel particles for protein delivery.* Annals of biomedical engineering, 2016. **44**(6): p. 1946-1958.

219. Kim, P.-H., et al., *Injectable multifunctional microgel encapsulating outgrowth endothelial cells and growth factors for enhanced neovascularization.* Journal of controlled release, 2014. **187**: p. 1-13.

220. Voudouris, P., et al., *Micromechanics of temperature sensitive microgels: dip in the Poisson ratio near the LCST.* Soft Matter, 2013. **9**(29): p. 7158-7166.

221. Muniz, E.C. and G. Geuskens, *Compressive elastic modulus of polyacrylamide hydrogels and semi-IPNs with poly (N-isopropylacrylamide).* Macromolecules, 2001. **34**(13): p. 4480-4484.

222. Veronese, F.M., *Peptide and protein PEGylation: a review of problems and solutions.* Biomaterials, 2001. **22**(5): p. 405-417.

223. Vojkovsky, T., B. Sullivan, and K.N. Sill, *Synthesis of heterobifunctional polyethylene glycols: Polymerization from functional initiators.* Polymer, 2016. **105**: p. 72-78.

224. Thelin, E.P., et al., *Serial sampling of serum protein biomarkers for monitoring human traumatic brain injury dynamics: a systematic review.* Frontiers in neurology, 2017. **8**: p. 300.

225. López-López, Á., et al., *A review of validated biomarkers obtained through metabolomics.* Expert review of molecular diagnostics, 2018. **18**(6): p. 557-575.

226. Cerqueira, M.R.F., et al., *Use of poly (methyl methacrylate)/polyethyleneimine flow microreactors for enzyme immobilization.* Microchemical Journal, 2015. **118**: p. 231-237.

227. Buddingh', B.C. and J.C. van Hest, *Artificial cells: synthetic compartments with life-like functionality and adaptivity.* Accounts of chemical research, 2017. **50**(4): p. 769-777.